

HU ISSN 1586–2070

JOURNAL OF COMPUTATIONAL AND APPLIED MECHANICS

An Open Access International Journal

Published by the University of Miskolc

VOLUME 9, NUMBER 2 (2014)



MISKOLC UNIVERSITY PRESS

EDITORS

László BARANYI, Institute of Energy Engineering and Chemical Machinery, University of Miskolc, H-3515 MISKOLC, Hungary, e-mail: arambl@uni-miskolc.hu

István PÁCZELT, Institute of Applied Mechanics, University of Miskolc, H-3515 MISKOLC, Hungary e-mail: mechpacz@uni-miskolc.hu

György SZEIDL, Institute of Applied Mechanics, University of Miskolc, H-3515 MISKOLC, Hungary e-mail: Gyorgy.SZEIDL@uni-miskolc.hu

EDITORIAL BOARD

Edgár BERTÓTI, Institute of Applied Mechanics, University of Miskolc, H-3515 MISKOLC, Hungary, e-mail: edgar.bertoti@uni-miskolc.hu

Atila BAKSA, Institute of Applied Mechanics, University of Miskolc, H-3515 MISKOLC, Hungary, attila.baksa@uni-miskolc.hu

István ECSEDI, Institute of Applied Mechanics, University of Miskolc, H-3515 MISKOLC, Hungary, mechecs@uni-miskolc.hu

Ulrich GABBERT, Institut für Mechanik, Otto-von-Guericke-Universität Magdeburg, Universitätsplatz 2, 39106 MAGDEBURG, Germany, ulrich.gabbert@mb.uni-magdeburg.de

Zsolt GÁSPÁR, Department of Structural Mechanics, Budapest University of Technology and Economics, Műegyetem rkp. 3, 1111 BUDAPEST, Hungary, gaspar@ep-mech.me.bme.hu

Robert HABER, Department of Theoretical and Applied Mechanics, University of Illinois at Urbana-Champaign, 216 Talbot Lab., 104 S. Wright Str., URBANA, IL 61801, USA, r-haber@uiuc.edu

Csaba HÓS, Department of Hydraulic Machines, Budapest University of Technology and Economics, Műegyetem rkp. 3, 1111 BUDAPEST, Hungary, HOSCSABA@vizgep.bme.hu

Károly JÁRMAI, Institute of Logistics, University of Miskolc, H-3515 MISKOLC, Hungary, altjar@uni-miskolc.hu

László KOLLÁR, Department of Strength of Materials and Structures, Budapest University of Technology and Economics, Műegyetem rkp. 3. K.II.42., 1521 BUDAPEST, Hungary, lkollar@eik.bme.hu

József KÖVECSES, Mechanical Engineering Department 817 Sherbrooke Street West, MD163 Montreal, Quebec H3A 2K6 jozsef.kovecses@mcgill.ca

Márta KURUTZ, Department of Structural Mechanics, Budapest University of Technology and Economics, Műegyetem rkp. 3, 1111 BUDAPEST, Hungary, kurutzm@eik.bme.hu

Herbert MANG, Institute for Strength of Materials, University of Technology, Karlsplatz 13, 1040 VIENNA, Austria, Herbert.Mang@tuwien.ac.at

Sanjay MITTAL, Department of Aerospace Engineering, Indian Institute of Technology Kanpur, UP 208 016, India, smittal@iitk.ac.in

Zenon MROZ, Polish Academy of Sciences, Institute of Fundamental Technological Research, Swietokrzyska 21, WARSAW, Poland zmroz@ippt.gov.pl

Gyula PATKÓ, Institute of Machine Tools and Mechatronics, University of Miskolc, H-3515 MISKOLC, Hungary, patko@uni-miskolc.hu

Jan SLADEK, Ústav stavbenictva a architektúry, Slovenskej akadémie vied, Dubróvska cesta 9, 842 20 BRATISLAVA, Slovakia, usarslad@savba.sk

Gábor STÉPÁN, Department of Applied Mechanics, Budapest University of Technology and Economics, Műegyetem rkp. 3, 1111 BUDAPEST, Hungary, stepan@mm.bme.hu

Barna SZABÓ, Center for Computational Mechanics, Washington University, Campus Box 1129, St. LOUIS, MO63130, USA, szabo@me.wustl.edu

Balázs TÓTH, Institute of Applied Mechanics, University of Miskolc, 3515 MISKOLC, Hungary, balazs.toth@uni-miskolc.hu

HONORARY EDITORIAL BOARD MEMBERS

Imre KOZÁK, Institute of Applied Mechanics, University of Miskolc, H-3515 Miskolc-Egyetemváros, Hungary

Tibor CZIBERE, Department of Fluid and Heat Engineering, University of Miskolc, H-3515 Miskolc-Egyetemváros, Hungary

R. Ivan LEWIS, Room 2-16 Bruce Building, Newcastle University, NEWCASTLE UPON TYNE, NE1 7RU, UK

Gábor HALÁSZ, Department of Hydraulic Machines, Budapest University of Technology and Economics, Műegyetem rkp. 3, 1111 BUDAPEST, Hungary,

SOLUTION OF 3D CONTACT PROBLEMS USING SPLINE INTERPOLATION

ATTILA BAKSA AND ISVÁN PÁCZELT

University of Miskolc

Department of Applied Mechanics, HUNGARY

mechab@uni-miskolc.hu, mechpacz@uni-miskolc.hu

TAMÁS SZABÓ

Széchenyi István University, Győr,

Department of Applied Mechanics, HUNGARY

tom.tolcsva@gmail.com

[Received: March 15, 2009]

Abstract. A three-dimensional elastic contact problem is examined. It is assumed that the displacements and deformations are small and the supposed zone of the contact domain must be single-connected, and surrounded by a smooth closed curve. The closed curve is interpolated by a single closed spline. For numerical tests three-dimensional p -extension finite elements are used. To take the conditions of contact and separation into account the penalty method is applied. Numerical examples presented here show the effect of positioning 3D p -version elements along the contact-separation and/or stick-and-slip borders and the influence of the friction coefficient, respectively.

Mathematical Subject Classification: 37J05, 76M10, 65D05, 65D10

Keywords: Contact problem, frictional contact, p -extension FEM, B-spline, interpolation with a closed spline, contact element positioning

1. INTRODUCTION

The modern history of contact mechanics might be said to have begun in 1882 with the publication by Hertz of his classic paper [1]. The classical Signorini problem [2] formulated in 1933 leading to the development of variational inequalities for the contact problem. These methods have been developed within several decades. After some analytical approaches published by Muskhelishvili [3] or Galin [4] there are numerous researchers who also worked on these fields e.g. Goldsmith [5], Fichera [6] or Kikuchi and Oden [7] and see some books for historical remarks in Johnson [8], in Kalker [9] or in Wriggers [10].

The finite element method (FEM) developed together with the growing power of modern computers. Turner and his colleagues in [11] have taken the first attempts to solve structural problems using finite elements in the late fifties. A further decade

must have gone by before the first papers, in which contact problems solved by FEM, appeared [12].

FEM can be classified into three main groups with respect to the type of refinement: h -, p -, and hp -extension. In the case of h -extension the size of the elements are decreased, while the p -extension increases only the polynomial degree of shape functions in order to give more accurate results. In recent years the interest in high order finite elements has been increased.

It was proved by Szabó and Babuška [13] that even in the case of singularities in the exact solution, the p -extension in combination with a proper mesh ensure an exponential rate of convergence in energy norm. If the mesh is aligned to points or lines of singularity, from practical point of view an adequate accuracy can be obtained. It was examined by Páczelt et al. in [14, 15] for two-dimensional examples of normal and frictional contact problems.

As the problem investigated in this paper is restricted to contact between convex bodies bounded by C^2 surfaces, and assuming small displacements and deformations, in this case of 3D contact problems the resulting contact domain is not a line, like in 2D, but a single-connected surface, which is bordered by a smooth closed curve. To ensure precise numerical results for 3D contact problems using p -extension elements, the determination of the contact zone or its three-dimensional contour is the key question of our investigation.

Article [16] examines the problems of elasto-plasticity with adaptive p -FEM. The present paper describes also an adaptive mesh modification technique which uses an interpolating spline curve. For an excellent and comprehensive treatment of B-splines from the numerical analyst's point of view, de Boor has served as the standard reference for close to 30 years [17]. A good introduction to Non-Uniform Rational B-splines, referred to as NURBS, can be found in [18]. A key advantage of using NURBS is the ability to represent conic sections and quadratic surfaces, such as ellipse, circle and cones [19]. Moreover, the free-form curves and surfaces are all a special case of the NURBS since the constant function 1 is a perfectly respectable spline, and can be used as the denominator in a rational representation.

During the last ten years, research activities have been focused on adaptive techniques that provide a discretization which is accurate and reliable. Adaptive techniques rely on indicators or estimators, which are able to predict the error of the approximated solution [13].

In the present article a solid and a linear elastic body's contact problem will be examined with adaptive p -extension FEM. Numerical examples show the convergence of the solution and the connection between the polynomial degree of shape functions and the relative error of the numerical results.

2. THE PROBLEM OF ELASTICITY

The considered mechanical system consists of two three-dimensional homogenous and isotropic elastic bodies. Only the mechanical interactions between them will be

examined. It is supposed that the displacements and deformations are small, and deformations evolving from external loads are only elastic, i.e. the task to be solved is in the frame of linear elasticity.

The examined contacting bodies (shown in Figure 1) have the volume V^α and outer boundary S^α , in which $\alpha = 1, 2$ marks the referred particle. The outer boundary is separated into three parts: on surface S_u^α the displacements \mathbf{u}_0^α are given; on surface S_p^α the surface traction $\tilde{\mathbf{p}}^\alpha$ is prescribed; while the surface S_c^α is the supposed zone of contact.

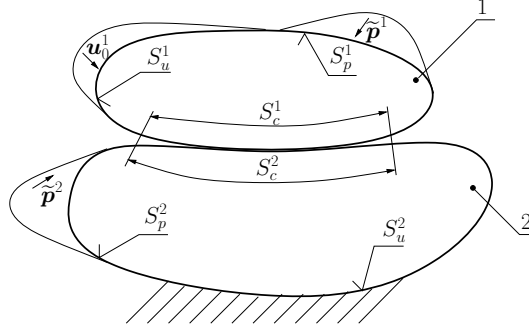


Figure 1. The examined contacting bodies

According to problem of elasticity the equilibrium equation is

$$\boldsymbol{\sigma}^\alpha \cdot \nabla + \mathbf{b}^\alpha = \mathbf{0} \quad \forall \mathbf{r}^\alpha \in V^\alpha \quad (2.1)$$

in which \mathbf{b}^α is the body force, $\boldsymbol{\sigma}^\alpha = \boldsymbol{\sigma}^\alpha(\mathbf{r}^\alpha)$ is the stress tensor, ∇ is the nabla operator. Strains are calculated as

$$\boldsymbol{\varepsilon}^\alpha = \frac{1}{2} (\mathbf{u}^\alpha \circ \nabla + \nabla \circ \mathbf{u}^\alpha) \quad \forall \mathbf{r}^\alpha \in V^\alpha, \quad (2.2)$$

where $\boldsymbol{\varepsilon}^\alpha = \boldsymbol{\varepsilon}^\alpha(\mathbf{r}^\alpha)$ is the strain tensor. The constitutive equation is

$$\boldsymbol{\sigma}^\alpha = \mathbf{D}^\alpha \cdot \cdot \boldsymbol{\varepsilon}^\alpha \quad \forall \mathbf{r}^\alpha \in V^\alpha, \quad (2.3)$$

in which \mathbf{D}^α is the fourth order elasticity tensor.

In equation (2.1) scalar product is denoted by a dot, double dots indicate the scalar product between two tensors in equation (2.3), and in equation (2.2) the circle denotes the dyadic (tensorial) product according to Lurje [20].

The natural and essential boundary conditions are defined as

$$\boldsymbol{\sigma}^\alpha \cdot \mathbf{n}^\alpha = \tilde{\mathbf{p}}^\alpha \quad \forall \mathbf{r}^\alpha \in S_p^\alpha, \quad \mathbf{u}^\alpha = \mathbf{u}_0^\alpha \quad \forall \mathbf{r}^\alpha \in S_u^\alpha. \quad (2.4)$$

The above equations (2.1)-(2.4) must be complemented with the conditions of contact-separation which are valid on S_c^α in order to fulfill all the requirements of the contact problem of linear elasticity.

2.1. Contact and separation. The outer normal of body α is denoted by \mathbf{n}^α . In the domain of the supposed zone of contact S_c^α the contact normal is defined as $\mathbf{n}_c = -\mathbf{n}^2 = \mathbf{n}^1$. Before loading, the distance h between the bodies is measured along the normal \mathbf{n}_c . h is decreased to the distance between the bodies after deformation is

$$d = d(\mathbf{u}) = u_n^2 - u_n^1 + h \quad \forall \mathbf{r}^\alpha \in S_c^\alpha, \quad (2.5)$$

which is shown in Figure 2. The normal components of the displacements are calculated as $u_n^\alpha = \mathbf{u}^\alpha \cdot \mathbf{n}_c$.

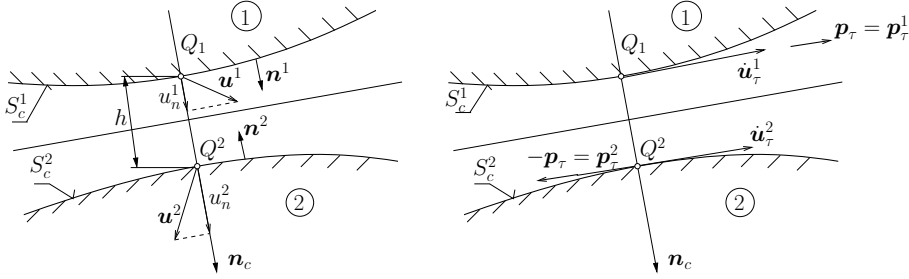


Figure 2. Contact and separation of two bodies

The normal components of the stresses on domain S_c^α can be determined as follows

$$\sigma_n^\alpha = \mathbf{n}^\alpha \cdot \boldsymbol{\sigma}^\alpha \cdot \mathbf{n}^\alpha \quad \forall \mathbf{r}^\alpha \in S_c^\alpha. \quad (2.6)$$

The contact pressure p_n is defined through the normal stress

$$p_n = -\sigma_n^1 = -\sigma_n^2 \quad \forall \mathbf{r}^\alpha \in S_c^\alpha, \quad (2.7)$$

and the tangential stress vectors

$$\mathbf{p}_\tau^\alpha = \boldsymbol{\sigma}^\alpha \cdot \mathbf{n}^\alpha - \sigma_n^\alpha \mathbf{n}^\alpha, \quad \mathbf{p}_\tau = \mathbf{p}_\tau^1 = -\mathbf{p}_\tau^2. \quad (2.8)$$

Summarising the statements written above the following conditions for contact and separation can be achieved.

(a) conditions of contact

$$d = 0, \quad p_n > 0 \quad \forall \mathbf{r} \in \Omega_p, \quad (2.9a)$$

(b) conditions of separation

$$d > 0, \quad p_n = 0 \quad \forall \mathbf{r} \in \Omega_0, \quad (2.9b)$$

(c) complementary conditions

$$d \geq 0, \quad p_n \geq 0, \quad p_n d = 0 \quad \forall \mathbf{r} \in S_c = \Omega_p \cup \Omega_0. \quad (2.9c)$$

The formulas (2.9a – 2.9c), called HERTZ-SIGNONIRINI-MOREAU conditions, give the basis of the solution of frictionless normal contact problems.

2.2. **Stick and slip.** Tangential stresses in the case of Coulomb-type friction are

$$\|\mathbf{p}_\tau^\alpha\| = \|\boldsymbol{\sigma}^\alpha \cdot \mathbf{n}^\alpha - \sigma_n^\alpha \mathbf{n}^\alpha\| \leq \mu p_n. \quad (2.10)$$

The tangential relative velocity is $\dot{\mathbf{u}}_\tau = \dot{\mathbf{u}}_\tau^2 - \dot{\mathbf{u}}_\tau^1$. The effects of friction are treated analogously to plasticity according to *Michalowski* and *Mróz* [21], i.e.

$$\dot{\mathbf{u}}_\tau = \dot{\mathbf{u}}_\tau^{(adh)} + \dot{\mathbf{u}}_\tau^{(slip)} \quad (2.11)$$

$$\dot{\mathbf{u}}_\tau^{(adh)} = \frac{\dot{\mathbf{p}}_\tau}{c_\tau}, \quad \dot{\mathbf{u}}_\tau^{(slip)} = \dot{\xi} \frac{\partial \phi}{\partial \mathbf{p}_\tau}, \quad \phi = \|\mathbf{p}_\tau\| - \mu p_n \leq 0, \quad (2.12)$$

where c_τ is the stiffness of connections at the interface and ϕ is the slip surface, $\dot{\xi} \geq 0$.

(a) With friction ($\Omega_p = \Omega_p^\alpha + \Omega_p^s$)

- on stick zone:

$$\dot{\mathbf{u}}_\tau(\mathbf{r}) = \dot{\mathbf{u}}_\tau^2(\mathbf{r}) - \dot{\mathbf{u}}_\tau^1(\mathbf{r}) = 0 \quad \text{and} \quad \|\mathbf{p}_\tau^\alpha\| \leq \mu p_n \quad \mathbf{r} \in \Omega_p^\alpha, \quad (2.13)$$

- on slip zone:

$$\dot{\mathbf{u}}_\tau(\mathbf{r}) \neq 0, \quad \text{and} \quad \mathbf{p}_\tau = \mu p_n \frac{\dot{\mathbf{u}}_\tau(\mathbf{r})}{\|\dot{\mathbf{u}}_\tau(\mathbf{r})\|} \quad \mathbf{r} \in \Omega_p^s. \quad (2.14)$$

(b) Without friction

$$\mathbf{p}_\tau^\alpha = \mathbf{0}. \quad (2.15)$$

Using the plasticity analogy the conditions for adhesion and slip are as follows

- in the adhesion (stick) zone

$$\phi < 0, \quad \dot{\xi} = 0 \quad (2.16)$$

- in the slip zone

$$\phi = 0, \quad \dot{\xi} > 0 \quad (2.17)$$

which ensures that $\phi \dot{\xi} = 0$.

Therefore the tangential stress can be expressed as

$$\dot{\mathbf{p}}_\tau = c_\tau \dot{\mathbf{u}}_\tau - c_\tau \dot{\mathbf{u}}_\tau^{(slip)} = c_\tau \dot{\mathbf{u}}_\tau - c_\tau \dot{\xi} \frac{\partial \phi}{\partial \mathbf{p}_\tau}. \quad (2.18)$$

The quasi-static problem is treated by the backward Euler time-discretization technique. So the time integration of (2.18) on the interval from t to $t + \Delta t$ gives

$${}^{t+\Delta t} \mathbf{p}_\tau = \mathbf{p}_\tau^* - c_\tau \Delta \xi \left[\frac{\partial \phi}{\partial \mathbf{p}_\tau} \right]^{t+\Delta t} = \mathbf{p}_\tau^* - c_\tau \Delta \xi \left[\frac{\partial \phi}{\partial \mathbf{p}_\tau} \right]^* = \mathbf{p}_\tau^* - \mathbf{p}_{\tau, m_0}^* \quad (2.19a)$$

where the predicted shear stress is

$$\mathbf{p}_\tau^* = {}^t \mathbf{p}_\tau + c_\tau ({}^{t+\Delta t} \mathbf{u}_\tau - {}^t \mathbf{u}_\tau), \quad (2.19b)$$

and

$$\phi^* = \|\mathbf{p}_\tau^*\| - \mu {}^{t+\Delta t} p, \quad \left[\frac{\partial \phi}{\partial \mathbf{p}_\tau} \right]^* = \frac{\mathbf{p}_\tau^*}{\|\mathbf{p}_\tau^*\|} \quad (2.19c)$$

and \mathbf{p}_{τ, m_0}^* is calculated by the well-known *return mapping algorithm* [10, 22].

2.3. The basis of the solution technique. The solution of the frictional contact problem is based on the principle of virtual power to ensure the normal contact condition with penalty term $p_n = -c_n d$

$$\sum_{\alpha} \left\{ \int_{V^{\alpha}} \delta \dot{\boldsymbol{\varepsilon}} \cdot {}^{t+\Delta t} \boldsymbol{\sigma} dV - \int_{V^{\alpha}} \delta \dot{\mathbf{u}} \cdot {}^{t+\Delta t} \mathbf{b} dV - \int_{S_p^{\alpha}} \delta \dot{\mathbf{u}} \cdot {}^{t+\Delta t} \tilde{\mathbf{p}} dS \right\} - \\ - \int_{{}^{t+\Delta t} S_c} \delta (\dot{u}_n^2 - \dot{u}_n^1) (-c_n d({}^{t+\Delta t} \mathbf{u})) dS - \int_{{}^{t+\Delta t} S_c} \delta (\dot{\mathbf{u}}_{\tau}^2 - \dot{\mathbf{u}}_{\tau}^1) \cdot {}^{t+\Delta t} \mathbf{p}_{\tau} dS = 0. \quad (2.20)$$

Using the $\int_t^{t+\Delta t} \dot{\mathbf{X}} d\tilde{t} = \Delta \mathbf{X}$ notation where t denotes the dimensionless loading parameter for integration of (2.20) gives the following variational equation

$$\sum_{\alpha} \left\{ \int_{V^{\alpha}} (\delta \Delta \boldsymbol{\varepsilon}) \cdot {}^{t+\Delta t} \boldsymbol{\sigma} dV - \int_{V^{\alpha}} (\delta \Delta \mathbf{u}) \cdot {}^{t+\Delta t} \mathbf{b} dV - \int_{S_p^{\alpha}} (\delta \Delta \mathbf{u}) \cdot {}^{t+\Delta t} \tilde{\mathbf{p}} dS \right\} - \\ - \int_{{}^{t+\Delta t} S_c} \delta (\Delta u_n^2 - \Delta u_n^1) (-c_n d({}^{t+\Delta t} \mathbf{u})) dS - \\ - \int_{{}^{t+\Delta t} S_c} \delta (\Delta \mathbf{u}_{\tau}^2 - \Delta \mathbf{u}_{\tau}^1) \cdot {}^{t+\Delta t} \mathbf{p}_{\tau} dS = 0. \quad (2.21)$$

Applying the partial derivation and integral theorem for the variation equation (2.21), the following formula is written for the normal stress in the contact zone S_c ,

$${}^{t+\Delta t} \sigma_n^1 = {}^{t+\Delta t} \sigma_n^2 = c_n d({}^{t+\Delta t} \mathbf{u}) \quad (2.22)$$

and for the tangential stress

$${}^{t+\Delta t} \mathbf{p}_{\tau} = {}^{t+\Delta t} p_{\tau} \mathbf{e}_{\tau}, \quad {}^{t+\Delta t} p_{\tau} = \mathbf{e}_{\tau} \cdot {}^{t+\Delta t} \boldsymbol{\sigma}^1 \cdot \mathbf{n}^1 = -\mathbf{e}_{\tau} \cdot {}^{t+\Delta t} \boldsymbol{\sigma}^2 \cdot \mathbf{n}^2. \quad (2.23)$$

Of course, the tangential stress ${}^{t+\Delta t} \mathbf{p}_{\tau}$ must satisfy the conditions (2.13) and (2.14), too.

2.4. Decomposition of mechanical quantities. Assuming small time steps, the mechanical quantities are decomposed into known values at time t and their increments

$$\begin{aligned} {}^{t+\Delta t} \boldsymbol{\sigma} &= {}^t \boldsymbol{\sigma} + \Delta \boldsymbol{\sigma}, & {}^{t+\Delta t} \mathbf{b} &= {}^t \mathbf{b} + \Delta \mathbf{b}, & {}^{t+\Delta t} p_n &= {}^t p_n + \Delta p_n, \\ {}^{t+\Delta t} \mathbf{u} &= {}^t \mathbf{u} + \Delta \mathbf{u}, & {}^{t+\Delta t} \tilde{\mathbf{p}} &= {}^t \tilde{\mathbf{p}} + \Delta \tilde{\mathbf{p}}, & {}^{t+\Delta t} \mathbf{p}_{\tau} &= {}^t \mathbf{p}_{\tau} + \Delta \mathbf{p}_{\tau} \end{aligned} \quad (2.24)$$

$$\begin{aligned} d({}^{t+\Delta t} \mathbf{u}) &= {}^{t+\Delta t} (u_n^2 - u_n^1 + h) = {}^t (u_n^2 - u_n^1 + h) + \Delta u_n^2 - \Delta u_n^1 + \Delta h \equiv \\ &\equiv {}^t d + \Delta d. \end{aligned}$$

Subtracting the virtual powers – written in t and $t + \Delta t$ time – from each other the basic functional for numerical calculations is

$$\sum_{\alpha} \left\{ \int_{V^{\alpha}} (\delta \Delta \boldsymbol{\varepsilon}) \cdot \Delta \boldsymbol{\sigma} \, dV - \int_{V^{\alpha}} (\delta \Delta \mathbf{u}) \cdot \Delta \mathbf{b} \, dV - \int_{S_p^{\alpha}} (\delta \Delta \mathbf{u}) \cdot \Delta \tilde{\mathbf{p}} \, dS \right\} -$$

$$+ \int_{t+\Delta t S_c} \delta (\Delta u_n^2 - \Delta u_n^1) (-c_n ({}^t d + \Delta u_n^2 - \Delta u_n^1 + \Delta h)) \, dS -$$

$$- \int_{t+\Delta t S_c} \delta (\Delta \mathbf{u}_{\tau}^2 - \Delta \mathbf{u}_{\tau}^1) \cdot \Delta \mathbf{p}_{\tau} \, dS = 0, \quad (2.25)$$

where $\Delta \mathbf{p}_{\tau}$ must be determined in different ways on adhesion and on slip subregions:

- in the adhesion subregion

$$\Delta \mathbf{p}_{\tau} = c_{\tau} (\Delta \mathbf{u}_{\tau}^2 - \Delta \mathbf{u}_{\tau}^1) = c_{\tau} \Delta \mathbf{u}_{\tau} \quad (2.26)$$

i.e., the bodies are connected by distributed elastic springs with coefficient c_{τ} .

- in the slip subregion

$$\Delta \mathbf{p}_{\tau} = \mu \frac{{}^{t+\Delta t} p_n}{\|\Delta \mathbf{u}_{\tau}\|} \Delta \mathbf{u}_{\tau} \quad {}^t \mathbf{p}_{\tau} = \mu \frac{{}^{t+\Delta t} p_n}{\|\mathbf{p}_{\tau}^*\|} \mathbf{p}_{\tau}^* \quad {}^t \mathbf{p}_{\tau} \quad (2.27)$$

i.e., the bodies are loaded by tangential traction which computed according to the Coulomb friction.

3. FE DISCRETIZATION WITH APPROXIMATED INCREMENTS

The increments in displacements are approximated in the usual form

$$\Delta \mathbf{u}^{\alpha} = \mathbf{N}^{\alpha} \Delta \mathbf{q}^{\alpha}, \quad \alpha = 1, 2 \quad (3.1)$$

where the shape functions in matrix \mathbf{N}^{α} consists of nodal modes, side modes and internal modes, $\Delta \mathbf{q}^{\alpha}$ is the vector of increments in displacement parameters [14]. Increments of strains

$$\Delta \boldsymbol{\varepsilon}^{\alpha} \rightarrow \Delta \underline{\boldsymbol{\varepsilon}}^{\alpha} = \mathbf{B}^{\alpha} \Delta \mathbf{q}^{\alpha} \quad (3.2)$$

and stresses

$$\Delta \boldsymbol{\sigma}^{\alpha} \rightarrow \Delta \underline{\boldsymbol{\sigma}}^{\alpha} = \mathbf{D}^{\alpha} \mathbf{B}^{\alpha} \Delta \mathbf{q}^{\alpha} \quad (3.3)$$

are calculated in the usual way. Here \mathbf{D}^{α} is the constitutive, and \mathbf{B}^{α} is the strain–displacement matrix. Normal and tangential displacements in the contact surface are approximated as follows

$$\Delta u_n^{\alpha} = \mathbf{L}^{\alpha} \Delta \mathbf{q}^{\alpha}, \quad \Delta \mathbf{u}_{\tau}^{\alpha} = \mathbf{L}_{\tau}^{\alpha} \Delta \mathbf{q}^{\alpha}. \quad (3.4)$$

where \mathbf{L}^{α} and $\mathbf{L}_{\tau}^{\alpha}$ are contains only the localized shape functions of matrix \mathbf{N}^{α} for the contact domain as follows

$$\mathbf{L}^{\alpha} = \mathbf{n}^{\alpha T} \mathbf{N}^{\alpha}(\xi, \eta, \zeta = 1), \quad \mathbf{L}_{\tau}^{\alpha} = \mathbf{P}^{\alpha} \mathbf{N}^{\alpha}(\xi, \eta, q, \zeta = 1), \quad (3.5)$$

using the normal \mathbf{n}^α and the tangential $\mathbf{t}_\xi^\alpha, \mathbf{t}_\eta^\alpha$ vectors of contact domain.

$$\mathbf{n}^\alpha \rightarrow \mathbf{n}^\alpha, \quad \mathbf{t}_\xi^\alpha = \frac{\partial \mathbf{r}^\alpha}{\partial \xi}, \mathbf{t}_\eta^\alpha = \frac{\partial \mathbf{r}^\alpha}{\partial \eta} \rightarrow \mathbf{P}^\alpha. \quad (3.6)$$

The vector of total displacement parameters is ${}^{t+\Delta t}\mathbf{q}^\alpha = {}^t\mathbf{q}^\alpha + \Delta\mathbf{q}^\alpha$.

Substituting these vectors into equation (2.25) the task is to solve the following system of equations

$$\sum_\alpha \left\{ \delta\Delta\mathbf{q}^{eT} \left[\underbrace{\int_{V^\alpha} \mathbf{B}^T \mathbf{D} \mathbf{B} dV}_{\mathbf{K}^\alpha} \Delta\mathbf{q}^\alpha - \underbrace{\int_{V^\alpha} \mathbf{N}^T \Delta\mathbf{b} dV - \int_{S_p^\alpha} \mathbf{N}^T \Delta\tilde{\mathbf{p}} dS}_{\Delta\mathbf{f}_E^\alpha} \right] + \delta\Delta\mathbf{q}^T [\mathbf{C}_n + \mathbf{C}_\tau] \Delta\mathbf{q} - \delta\Delta\mathbf{q}^T \mathbf{f}_c = 0, \quad (3.7)$$

in which the contact stiffness matrices are

$$\mathbf{C}_n = \int_{t+\Delta t S_c} \begin{bmatrix} -\mathbf{L}^{1T} \\ \mathbf{L}^{2T} \end{bmatrix} c_n \begin{bmatrix} -\mathbf{L}^1 & \mathbf{L}^2 \end{bmatrix} dS, \quad \mathbf{C}_\tau = \int_{t+\Delta t S_c^{(adh)}} \begin{bmatrix} -\mathbf{L}_\tau^{1T} \\ \mathbf{L}_\tau^{2T} \end{bmatrix} c_\tau \begin{bmatrix} -\mathbf{L}_\tau^1 & \mathbf{L}_\tau^2 \end{bmatrix} dS. \quad (3.8)$$

Introducing the notations for the quasi-triangular stiffness matrix \mathbf{K}

$$\mathbf{K} = \begin{bmatrix} \mathbf{K}^1 & \mathbf{1} \\ \mathbf{0} & \mathbf{K}^2 \end{bmatrix}, \quad (3.9)$$

and vector of load on the contact surface

$$\mathbf{f}_c^{(k-1)} = \int_{t+\Delta t S_c} \begin{bmatrix} -\mathbf{L}^{1T} \\ \mathbf{L}^{2T} \end{bmatrix} (-c_n \Delta h) dS - \int_{t+\Delta t S_c} \begin{bmatrix} -\mathbf{L}^{1T} \\ \mathbf{L}^{2T} \end{bmatrix} c_n {}^t d dS + \int_{t+\Delta t S_c^{(slip)}} \begin{bmatrix} -\mathbf{L}_\tau^{1T} \\ \mathbf{L}_\tau^{2T} \end{bmatrix} (\mu {}^{t+\Delta t} p_n^{(k-1)} \frac{\mathbf{p}_\tau^*}{|\mathbf{p}_\tau^*|} - {}^t \mathbf{p}_\tau) dS, \quad (3.10)$$

the final equation is written as

$$[\mathbf{K} + \mathbf{C}_n + \mathbf{C}_\tau]^{(k)} \Delta\mathbf{q}^{(k)} = \Delta\mathbf{f}_E + \mathbf{f}_c^{(k-1)} \quad (3.11)$$

which is solved by iterative technique. The solution process is controlled by the change in the adhesion/slip subdomains iteratively until the constraints in equations (2.10)-(2.17) are satisfied on the integration points of the contact domain. It means that on all contact elements the local condition of stick and slip is fulfilled.

4. INTERPOLATION WITH CLOSED SPLINE

In the present investigation it is supposed that the border curve of the resulting contact domain is a closed, smooth and continuous one. Thus it can be interpolated by a parametric spline curve. In geometric modeling and mechanical design parametric curves like B-spline curves and their rational generalization, i.e. Non-Uniform

Rational B-spline curves or shortly NURBS, are frequently used because of their capability for defining new object, or describing existing curves and borders. They also have a usefull property, that is the ease of changeability.

To define a NURBS a simple data structure must be given in advance, which consists of three parts: the *control points* \mathbf{v}_i , the vector of *knot values* \mathbf{u} and the *weight factors* w_i which are associated with the control points. When one deals with non-rational B-splines the last mentioned weights are missing. Hereby a NURBS can be modified through one of the three above mentioned structure elements.

In this section only a short summary is provided about the interpolation with closed NURBS, more details can be found in the book of Piegl and Tiller [18].

A NURBS curve is defined so that

$$\mathbf{c}_r(t) = \sum_{i=1}^n R_i^q(t) \mathbf{v}_i \tag{4.1}$$

in which

$$R_i^q(t) = \frac{N_i^q(t) w_i}{\sum_{j=1}^n N_j^q(t) w_j} \tag{4.2}$$

where n is the number of sample points, vector \mathbf{v}_i stores the coordinates of the control point, w_i denotes the weight factor of the i^{th} control point, N_i^q is the i^{th} normalized B-spline basis function of order q (degree $q - 1$), and $\mathbf{c}_r(t)$ gives the position of a point on the curve. The basis functions are obtained through a knot vector, which defines the functions' break positions.

Consider the problem of closed NURBS interpolation to a sequence of points \mathbf{d}_i ($i = 1, \dots, m$) of a closed polygon, where $(q - 1)$ constraints are additionally imposed to satisfy $C^{(q-2)}$ continuity at the endpoints of a resulting curve. It is an assumption that no two consecutive vertices on the polygon are the same.

When a cyclic knot vector [23] is applied, the required constraints are the following

$$\mathbf{v}_{\lceil i \rceil} = \begin{cases} \mathbf{v}_i & \text{if } 1 \leq i \leq m, \\ \mathbf{v}_{i \bmod (m+1)+1} & \text{if } m < i \leq m + q - 1, \end{cases} \tag{4.3}$$

in which the operation $(i \bmod j)$ gives the residuum of the quotient $\frac{i}{j}$. This results in overlapped control points, i.e. $\mathbf{v}_1 = \mathbf{v}_{m+1}, \dots, \mathbf{v}_{q-1} = \mathbf{v}_{m+q-1}$.

To determine the control points the following linear equation must be solved

$$\mathbf{d}_i = \mathbf{c}_r(t_i) = \sum_{k=1}^n R_k^q(t_i) \mathbf{v}_{\lceil k \rceil} \quad 1 \leq i \leq m. \tag{4.4}$$

Rewriting equation (4.4) in matrix form using equations (4.2) and (4.3) leads to

$$\mathbf{N}^q \mathbf{V} = \mathbf{D}, \tag{4.5}$$

in which

$$\mathbf{N}^q = \frac{1}{\sum_{j=1}^n N_j^q(t_i) w_j} \begin{bmatrix} w_1 N_1^q(t_1) + w_{m+1} N_{m+1}^q(t_1) & \cdots & w_m N_m^q(t_1) \\ w_1 N_1^q(t_2) + w_{m+1} N_{m+1}^q(t_2) & \cdots & w_m N_m^q(t_2) \\ \vdots & & \vdots \\ w_1 N_1^q(t_m) + w_{m+1} N_{m+1}^q(t_m) & \cdots & w_m N_m^q(t_m) \end{bmatrix} \quad (4.6)$$

where it is required to make summation in the first few $(q - 1)$ columns because of the overlapped control points and

$$\mathbf{V} = \begin{bmatrix} v_{1x} & v_{1y} & v_{1z} \\ v_{2x} & v_{2y} & v_{2z} \\ \vdots & \vdots & \vdots \\ v_{mx} & v_{my} & v_{mz} \end{bmatrix}, \quad \mathbf{D} = \begin{bmatrix} d_{1x} & d_{1y} & d_{1z} \\ d_{2x} & d_{2y} & d_{2z} \\ \vdots & \vdots & \vdots \\ d_{mx} & d_{my} & d_{mz} \end{bmatrix}. \quad (4.7)$$

Finally, a square coefficient matrix \mathbf{N}^q with size $m \times m$ is obtained. Thus the m interpolation points determine n control points since the $m+1^{\text{th}}$, $m+2^{\text{th}}$, \dots , control points are the same as the 1^{st} , 2^{nd} , \dots control points.

4.1. Choosing the parameters. The first step during interpolation is to assign parameters to different interpolation points, which are on the resulting parametric curve. It means that the parameters t_i ($i = 1, \dots, m$) are chosen in a way that the following equation holds true

$$\mathbf{d}_i = \mathbf{c}_r(t_i) \quad 1 \leq i \leq m. \quad (4.8)$$

In Figure 3 the curve must pass over five given interpolation points, i.e. five parameters t_1, \dots, t_5 are needed to be chosen in the first step.

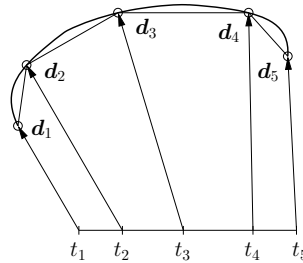


Figure 3. Relationship between the interpolation points and the parameters

Several techniques exist for making this assignment between the interpolation points and the parameters, see Refs.[18, 19, 23]. In this paper the parameters are chosen according to the chord length.

If the interpolating curve is closed, i.e. $\mathbf{d}_1 = \mathbf{d}_{m+1}$, the polygon – given by \mathbf{d}_i ($i = 1, \dots, m$) different interpolation points – is also closed. The parameters are

chosen by chord length with the following assumptions: Parameter $t_1 = 0$ is assigned to \mathbf{d}_1 , while parameter $t_{m+1} = 1$ is assigned to the imagined point \mathbf{d}_{m+1} .

Other parameters t_i ($i = 2, \dots, m$) can be computed with the help of chord lengths

$$\begin{aligned}
 t_1 &= 0, & t_{m+1} &= 1, \\
 t_i &= \frac{1}{L_c} \sum_{j=2}^i |\mathbf{d}_j - \mathbf{d}_{j-1}| & 1 < i < m + 1,
 \end{aligned}
 \tag{4.9}$$

where L_c is the length of the closed polygon

$$L_c = \sum_{i=2}^{m+1} |\mathbf{d}_i - \mathbf{d}_{i-1}|.
 \tag{4.10}$$

4.2. Generating the knot vector. After choosing the parameters, the next important step for creating an interpolation curve is to generate the knot vector $\mathbf{u} = [u_1, \dots, u_l]$ which is needed to obtain the normalized B-spline basis functions.

Since the knot vector is searched for a closed interpolating curve the parameters t_1, t_2, \dots, t_m are known. The number of control points which can be calculated from equation (4.5) is $n = m + q - 1$, therefore the number of knot values, which are written in the knot vector \mathbf{u} , is $l = m + 2q - 1$, see. [23].

In this way there exist no such a knot value which has $k > 1$ multiplicity. For generating the knot values the following term is applied, which is partially based on Ref. [23]

$$\begin{aligned}
 u_{-k} &= u_{1-k} + u_{n-q-k+2} - u_{n-q-k+3} & k &= 1, \dots, q - 1, \\
 u_1 &= 0, & u_{n-q+2} &= 1 \\
 u_i &= \frac{1}{2z + 1} \sum_{j=i-z}^{i+z} s_j & i &= 2, \dots, n - q + 1, \\
 u_{n-q+2+k} &= u_{n-q+1+k} + u_{k+1} - u_k & k &= 1, \dots, q - 1
 \end{aligned}
 \tag{4.11}$$

in which $z = \lfloor \frac{q-1}{2} \rfloor$, $\lfloor x \rfloor$ means the greatest integer which is not greater than x . For calculating s_j ($j = -(z + 2), \dots, m + z$) refer to the following rules

$$s_j = \begin{cases} u_1 + t_{m+1+j} - t_{m+1} & \text{if } -(z - 1) \leq j \leq -1, \\ t_j & \text{if } 1 \leq j \leq (m + 1), \\ u_{n-q+2} + t_{j-m-1} & \text{if } (m + 2) \leq j \leq (m + z) \end{cases}
 \tag{4.12}$$

where $u_{n-q+2} = t_{m+1} = 1$.

For better understanding of the above formulation let us see a numerical example to generate the knots for a fourth order ($q = 4$) interpolation spline. There are $m = 8$ interpolation points given, and the aim is to create a closed spline which crosses all the interpolation points $\mathbf{d}_1, \dots, \mathbf{d}_8$. The parameters t_1, \dots, t_8 are also calculated, according to the chord length, and listed in Table 1.

Table 1. Parameters for ($m = 8$) interpolation points

t_1	t_2	t_3	t_4	t_5	t_6	t_7	t_8	t_9
0	$\frac{1}{8}$	$\frac{2}{8}$	$\frac{3}{8}$	$\frac{4}{8}$	$\frac{5}{8}$	$\frac{6}{8}$	$\frac{7}{8}$	1

The task is to generate the cyclic knot vector \mathbf{u} . The number of control points is $n = m + q - 1 = 11$, therefore the number of knot values is $l = n + q = 15$. The parameters for the cyclic knot vector \mathbf{u} are $u_1 = 0$ and $u_{n-q+2} = u_9 = 1$ while the rest can be obtained by means of equations (4.11) and (4.12). The results are summarised in Table 2.

Table 2. Cyclic knot vector ($q = 4, m = 8$)

(1)	(2)	(3)	(4)	(5)	(6)	(7)	(8)	(9)	(10)	(11)	(12)	(13)	(14)	(15)
u_{-3}	u_{-2}	u_{-1}	u_1	u_2	u_3	u_4	u_5	u_6	u_7	u_8	u_9	u_{10}	u_{11}	u_{12}
$-\frac{3}{8}$	$-\frac{2}{8}$	$-\frac{1}{8}$	0	$\frac{1}{8}$	$\frac{2}{8}$	$\frac{3}{8}$	$\frac{4}{8}$	$\frac{5}{8}$	$\frac{6}{8}$	$\frac{7}{8}$	1	$\frac{9}{8}$	$\frac{10}{8}$	$\frac{11}{8}$

4.3. Numerical example. A simple Fortran code is developed to interpolate a set of points which are chosen by the contact search algorithm, i.e. the points are all along the contact-separation border. Now let us consider a 2D interpolation across ($m = 8$) points $\mathbf{d}_i, (i = 1, \dots, 8)$ which are in the same plane (see Figure 4.).

Table 3. Coordinates of interpolation points

\mathbf{d}_i	x	y	z	\mathbf{d}_i	x	y	z
\mathbf{d}_1	$-\sqrt{2}$	$-\sqrt{2}$	5.0	\mathbf{d}_5	$\sqrt{2} + 0.2$	$\sqrt{2} + 0.2$	5.0
\mathbf{d}_2	-2.0	0.0	5.0	\mathbf{d}_6	2.0	0.0	5.0
\mathbf{d}_3	$-\sqrt{2} - 0.2$	$\sqrt{2} + 0.2$	5.0	\mathbf{d}_7	$\sqrt{2}$	$-\sqrt{2}$	5.0
\mathbf{d}_4	0.0	3.0	5.0	\mathbf{d}_8	0.0	-2.0	5.0

It is obvious, that the number of control points belonging to the closed interpolation spline curve is ($n = 11$). Since the order of the B-spline basis function is chosen for $q = 4$, the first and last three control points are overlapped. The calculated

Table 4. Coordinates of control points

\mathbf{v}_i	x	y	z	\mathbf{v}_i	x	y	z
\mathbf{v}_8	0.0	-2.21321	5.0	\mathbf{v}_4	0.0	3.69991	5.0
$\mathbf{v}_1 = \mathbf{v}_9$	-1.58342	-1.57357	5.0	\mathbf{v}_5	1.72789	1.75406	5.0
$\mathbf{v}_2 = \mathbf{v}_{10}$	-2.16753	0.06703	5.0	\mathbf{v}_6	2.16753	0.06703	5.0
$\mathbf{v}_3 = \mathbf{v}_{11}$	-1.72789	1.75406	5.0	\mathbf{v}_7	1.58342	-1.57357	5.0

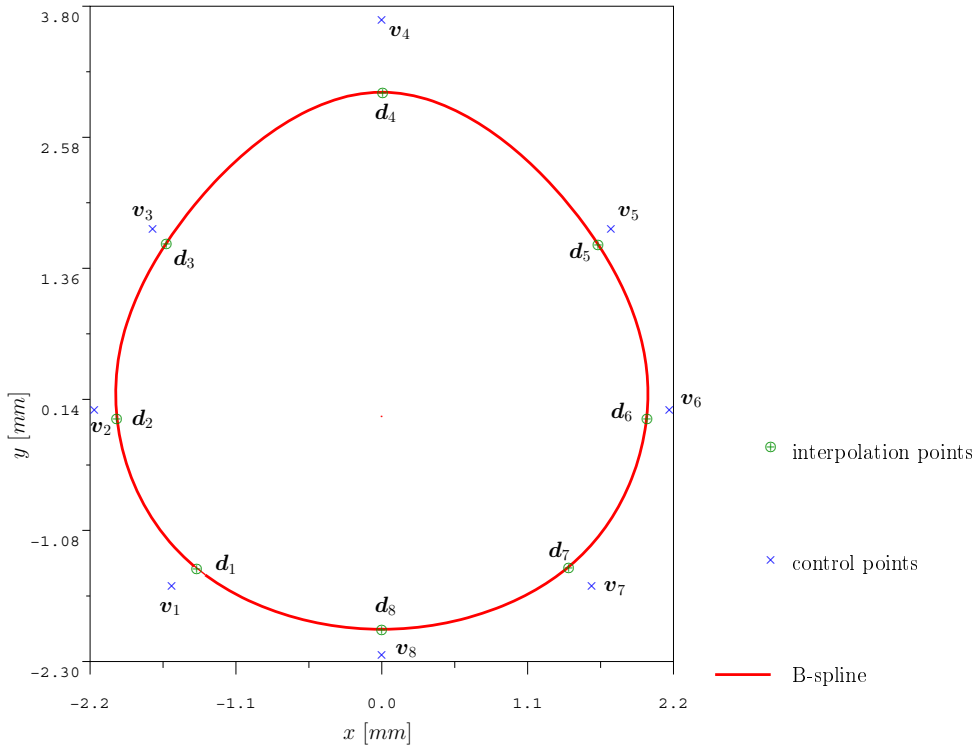


Figure 4. Interpolation with a spline curve generated numerically.

coordinates of the control points \mathbf{v}_i , ($i = 1, \dots, 11$) are illustrated in Figure 4. For the sake of simplicity, here the weights w_i are prescribed to 1. The parameters for the interpolation points are generated according to chord lengths.

The resulting two-dimensional NURBS curve is drawn in Figure 4 which is generated by the calculated control points. For drawing the spline, 303 points are determined along the curve and between the points a line segments are used.

5. EXAMPLE FOR 3D CONTACT

Here the contact of two bodies is considered (shown in Figure 5). The upper body is a rigid sphere and the lower one is an elastic block with the geometrical data $R = 800$ mm, $a = 5$ mm, $b = c = 10$ mm. The material parameters are the modulus of elasticity $E_1 = \infty$, $E_2 = 2.1 \cdot 10^5$ MPa and the Poisson-ratio $\nu_2 = 0.3$. The contact

problem is investigated in frictional case as well. Here three different coefficients of friction are applied for three different computations, $\mu_1 = 0.08$, $\mu_2 = 0.1$, $\mu_3 = 0.12$. The upper body is loaded on its top by a prescribed displacement $w_0 = 5.0 \cdot 10^{-3}$ mm.

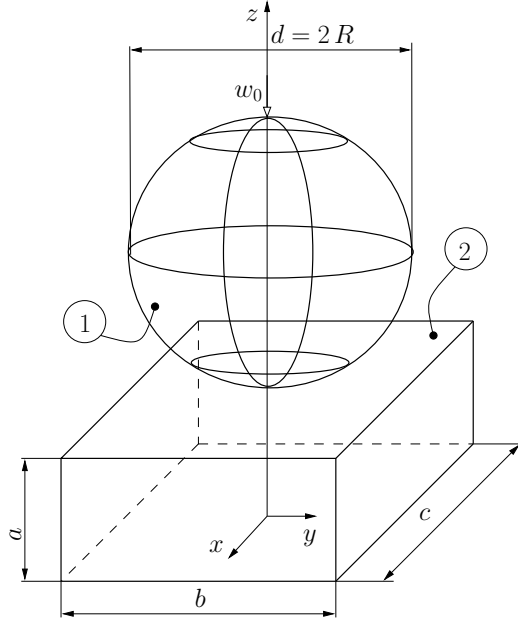


Figure 5. Geometry of the contacting bodies.

Two types of contact problems are investigated. Firstly, a normal contact problem is analysed in order to make a comparison between the solution achieved by the Hertz-theory and the finite element computation. Secondly, frictional contact is examined to get to know more about the stick and slip zones with the use of different friction coefficients.

Approximating the analytical solution according to the HERTZ-theory [1] the following formulae are used

$$a_0 = \sqrt[3]{\frac{3}{4} F k \frac{R_1 R_2}{R_1 + R_2}}, \quad p_0 = \frac{\sqrt[3]{6}}{\pi} \sqrt[3]{\frac{F}{k^2} \left(\frac{R_1 + R_2}{R_1 R_2} \right)^2} \quad (5.1)$$

in which F is the applied compression force, a_0 is the size of the contact domain, p_0 is the maximal contact pressure, R_1 and R_2 are the radii of the upper and the lower body, respectively. Here the lower contacting body is a brick therefore $R_2 = \infty$ i.e.

$$\frac{R_1 + R_2}{R_1 R_2} = \frac{1}{R_1} \quad \text{and} \quad \frac{R_1 R_2}{R_1 + R_2} = R_1, \quad (5.2)$$

and since the upper body is rigid

$$k = \frac{1 - \nu_2^2}{E_2}.$$

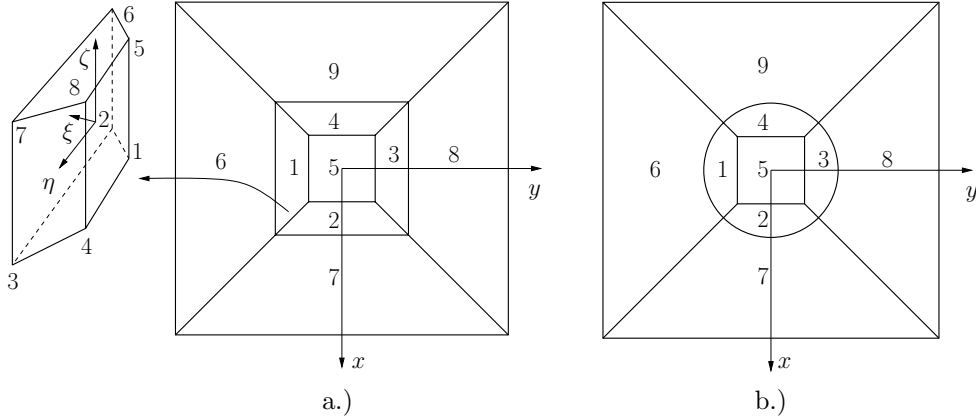


Figure 6. Applied FE meshes without friction.

In all our numerical investigations p -extension finite elements are used. The applied FE meshes are shown in Figure 6 and Figure 7. In case of the normal contact problem the aim is to identify the border of contact zone. Therefore only 9 elements are applied. Figure 6a illustrates the mesh which was used only for test reasons and as an initial point for computations. Naturally, it cannot be expected accurate results using such a coarse mesh for a problem in which a rigid spherical intender is used. Therefore the mesh was modified according to Figure 6b where the borders of elements 1, 2, 3, 4 are interpolated by properly chosen splines.

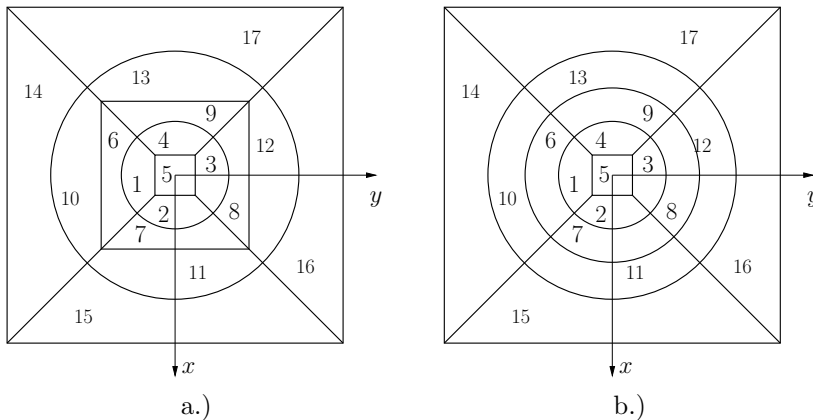


Figure 7. Applied FE meshes with friction.

In frictional case not only the contact border but also the stick and slip zones are investigated. It means that two subdomains exist in the real contact surface and between them the algorithm must identify also a smooth well-defined border. Here more elements are used to distinguish the sticking and slipping elements and to ensure smooth stress distributions on these zones.

5.1. The search of border points. Determining the points on contact-separation or stick-slip borders is a key task before making the interpolation. Figure 8 shows the points which must be identified. The code developed uses eight different directions along which the search is performed. These directions chosen follow the edges of elements and the integration points in the middle of each contact elements.

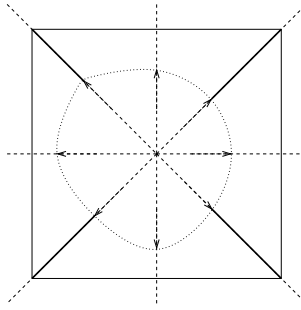


Figure 8. Directions on which the points are to be identified.

The search of border points are based on the computed results determined in previous step. In the integration points of each directions the contact pressure is produced and before the supposed border point all the pressure values have the same sign. See the illustration in Figure 9.

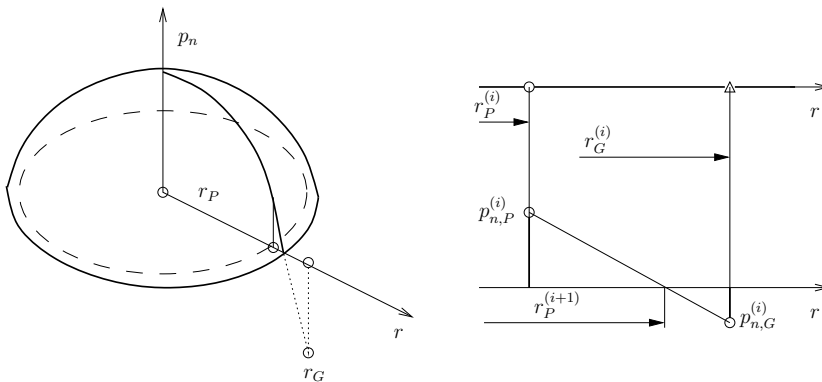


Figure 9. Linear approximation of a border point.

The border point can be identified after some finite steps, using the following linear iteration schema

$$r_P^{(i+1)} = r_P^{(i)} + \frac{p_{n,P}^{(i)}}{p_{n,P}^{(i)} - p_{n,G}^{(i)}} \left(r_G^{(i)} - r_P^{(i)} \right). \quad (5.3)$$

According to equation (5.3) the eight points of the border are determined which are interpolated with a single closed B-spline. The advantage of this procedure can be easily noticeable for non-symmetrical indentation problems where the resulting contact zone is *a priory* not known .

5.2. Results for normal contact. Two types of meshes are applied. In the first case straight bordered elements are used. The results for these computations are illustrated in Figures 10 and 11.

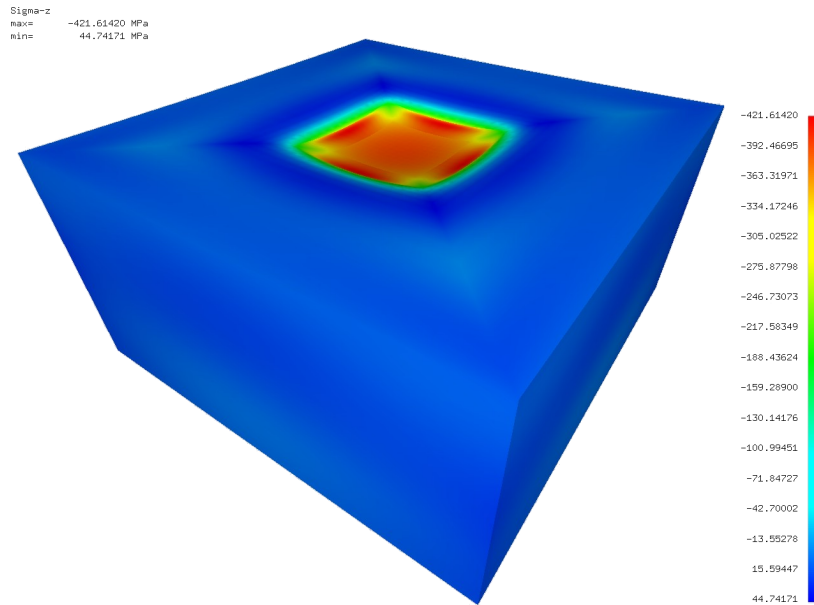


Figure 10. Oscillation in $(-\sigma_z)$ normal stress distribution.

On Figure 11 the normal pressure is drawn as a function of x coordinates. The polynomial degree is increased from 4 to 8. The normal pressure can be computed from the penalty term $(-c_N \cdot d^-)$ and the derivatives of displacements $(-\sigma_z)$, respectively. Results shown in Figure 11 are not acceptable because it cannot describe the smooth pressure distribution along the axis x . Hence the application of straight bordered elements are not adequate.

In the second case spline bordered elements are applied. Computations show smoother pressure distribution, as can be seen in Figures 12 and 13. This shows

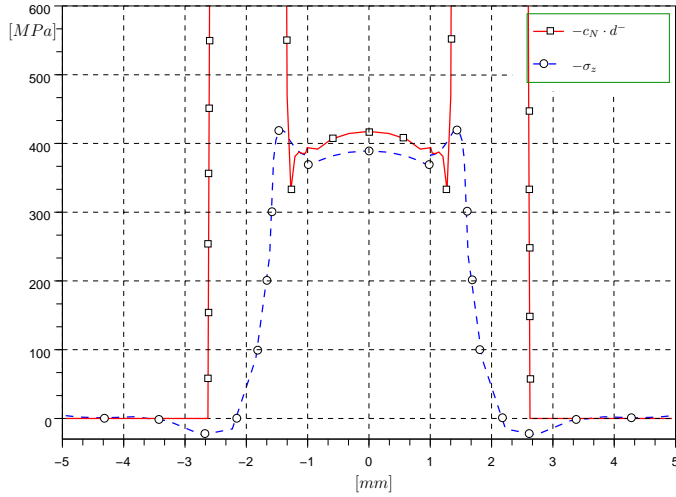


Figure 11. Contact pressure calculated by straight element borders.

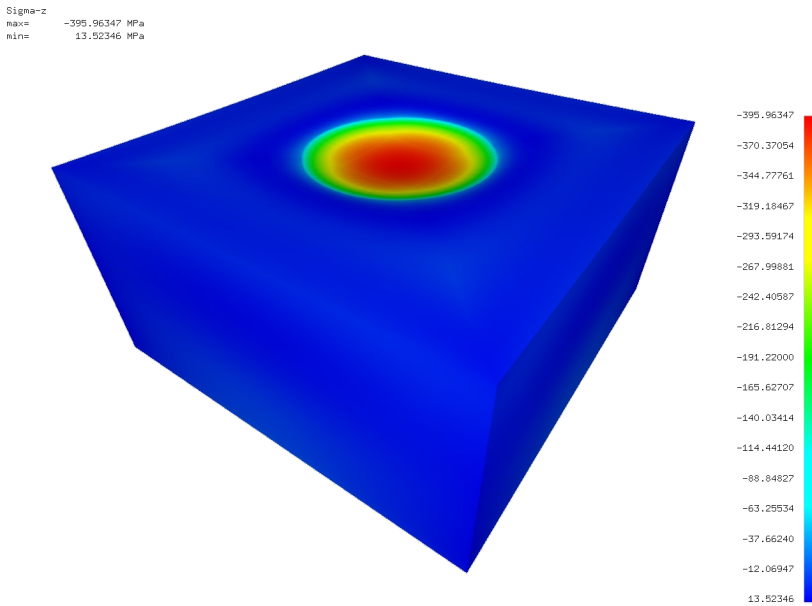


Figure 12. Oscillation free results in case of $(-\sigma_z)$.

the analytical results coming from equations (5.1) and the numerical results, respectively. In numerical cases the applied polynomial degree is also varied from 4 to 8.

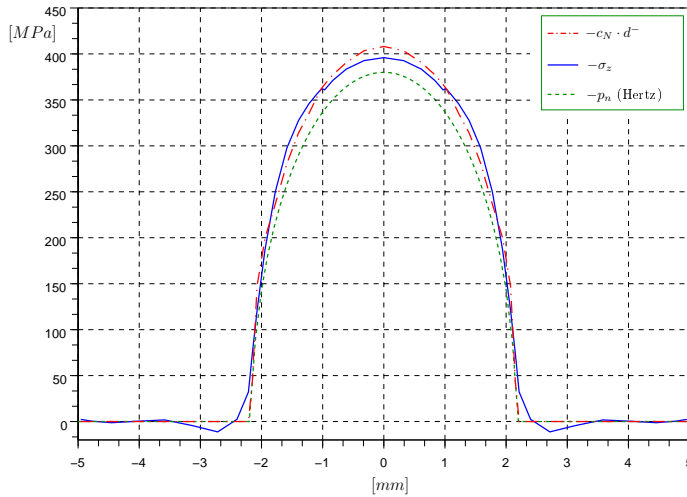


Figure 13. Contact pressure compared with the Hertzian result.

Table 5. Results of normal contact with spline border elements $w = -0.005$ mm

	p	a_0 [mm]	p_n [MPa]
HERTZ		2.000	367.28
FEM	4	2.100	491.76
	5	2.111	462.24
	6	2.139	423.66
	7	2.157	401.34
	8	2.161	395.96

The discrepancy between the analytical and the numerical results – see Tab. 5 – can be explained by the different assumptions used for the boundary value problem in the theoretical and numerical approaches, i.e. the lower body has finite dimensions in all directions.

If one makes a comparison between these numerical results, it will be obviously seen that the application of positioning elements [14] with spline borders is suitable. Figure 14 draws the relative error in energy norm in three different computation series: straight bordered elements with and without remeshing, and elements bounded by a positioning spline curve.

5.3. Results for frictional contact. Here, friction is taken into account. After the solution of the normal contact problem the effects of friction are also applied. Therefore it is computed with an iterational procedure.

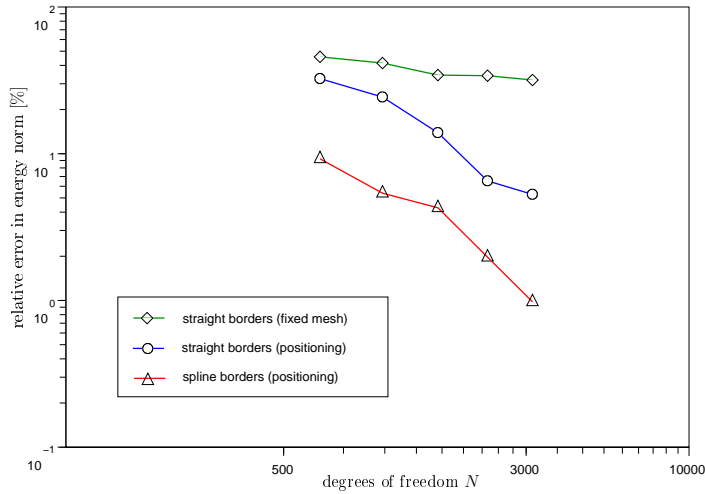
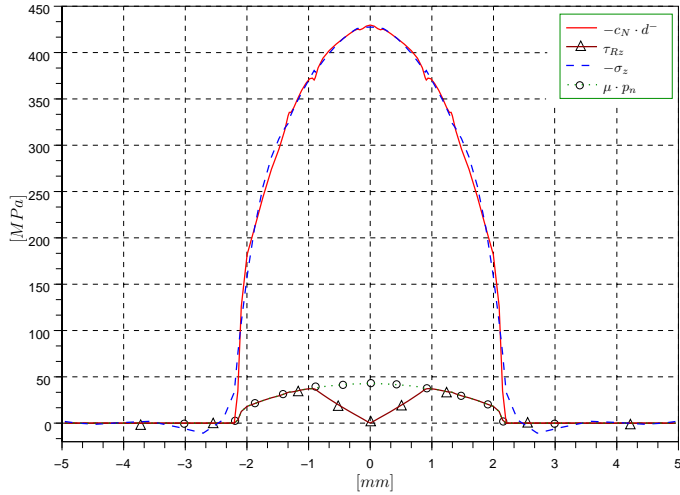


Figure 14. Relative errors without friction.

Figure 15. Contact pressure and shear stress with $\mu = 0.10$.

As is known, in the case of frictional contact there are two additional domains inside the contact zone. These are the stick and slip domains which are distinguished according to the relation between shear and the normal stresses. The size of the adhesion zone is $r_{adh} = 0.96$ mm, while the slip zone is $0.96 \text{ mm} \leq r_{slip} \leq 2.16$ mm which can be identified from Figure 15.

Results computed with $\mu = 0.10$ are illustrated in Figure 15 where τ_{Rz} means the shear stress.

Figure 16 shows the effects of the friction coefficient on relative energy norm. The polynomial order of shape functions is increased from 4 to 8 in order to see the convergence in the solution.

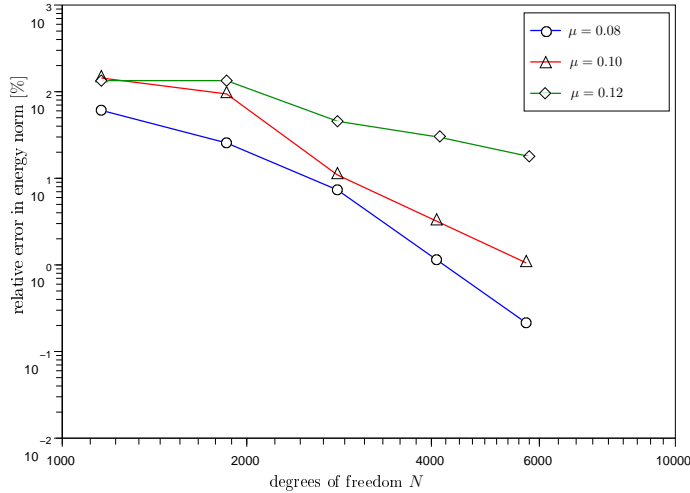


Figure 16. Relative errors with different friction coefficients.

Using the spline border positioning process the error in energy norm is smaller comparing to meshes without spline interpolation.

6. CONCLUSIONS

Unilateral contact problems have been solved by p -extension of the finite element method with the following assumptions:

- the contact region is single connected,
- the border of the contact region is a smooth curve, and the border curve of the stick and slip zones is also smooth.

In order to achieve high accuracy, the treatment of weak singularities along the border of the contact region and along the border curve of the stick and slip zones are needed. The positioning of the spline to the contact border and to the stick-and-slip zone proved to be an efficient method.

The border curves related to the contact zones are interpolated by B-splines using only a couple of design parameters. The localization of the border curve of the stick

and slip zones requires more iteration steps than to find the border of the contact region.

Acknowledgements. This research was (partially) carried out in the framework of the Center of Excellence of Innovative Engineering Design and Technologies at the University of Miskolc.

REFERENCES

1. HERTZ, H.: Über die Berührung fester elastischer Körper. *Journal für die Reine und Angewandte Mathematik*, **29**, (1882), 156–171.
2. SIGNORINI, A.: *Sopra alcune questioni di elastostatica*. Ph.D. thesis, Atti della Società Italiana per il Progresso delle Scienze, 1933.
3. MUSKHELISHVILI, N. I.: *Some Basic Problems of the Mathematical Theory of Elasticity*. Moscow, 3rd edn., 1949. In Russian (English translation by J.R.M. Radok, Noordhoff, 1953.).
4. GALLIN, L. A.: *Contact Problems in the Theory of Elasticity*. Moscow, 1953. In Russian (English translation by H. Moss, North Carolina State College, Dep. Math., 1961.).
5. GOLDSMITH, W.: *Impact: The theory and physical behavior of colliding solids*. London: Edward Arnold, 1960.
6. FICHERA, G.: Problemi elastostatici con cingoli unilaterale: il problema di signorini con ambigue condizioni al contorno. Series 8, 7, 91.
7. KIKUTCHI, N. and ODEN, J. T.: *A study of variational inequalities and finite element methods*. Contact problems in elasticity, Philadelphia: SIAM, 1988.
8. JOHNSON, K. L.: *Contact Mechanics*. Cambridge University Press, 1985.
9. KALKER, J. J.: *A course of contact mechanics*. TU Delft, Neatherland, 1985.
10. WRIGGERS, P.: *Computational Contact Mechanics*. John Wiley & Sons, Ltd., 2002.
11. TURNER, M. J., CLOUGH, R. W., MARTIN, H. C., and TOPP, L. J.: Stiffness and deflection analysis of complex structures. *Journal of the Aeronautical Sciences*, **23**, (1956), 805–823.
12. WILSON, E. A. and PARSONS, B.: Finite element analysis of elastic contact problems using differential displacements. *International Journal for Numerical Methods in Engineering*, **2**, (1970), 387–395.
13. SZABÓ, B. A. and BABUŠKA, I.: *Finite Element Analysis*. John Wiley & Sons, 1991.
14. PÁCZELT, I., SZABÓ, B., and SZABÓ, T.: Solution of contact problem using the hp -version of the finite element method. *Computers and Mathematics with Applications*, **38**, (1999), 49–69.
15. PÁCZELT, I. and SZABÓ, T. .: Solution of contact optimization problems of cylindrical bodies using hp -fem. *International Journal for Numerical Methods in Engineering*, **53**, (2002), 123–146.
16. DÜSTER, A., NIGGL, A., NÜBEL, V., and RANK, E.: A numerical investigation of high-order finite elements for problems of elasto-plasticity. **17**, (2002), 429–437.
17. DE BOOR, C.: *A Practical Guide to Splines*. Applied Mathematical Sciences, Springer-Verlag, New York, 1978.

-
18. PIEGL, L. and TILLER, W.: *The NURBS book*. Berlin: Springer, 1995.
 19. BEATTY, R. H. B. J. C. and BARSKY, B. A.: *An Introduction to Splines for use in Computer Graphics & Geometric Modeling*. 1987.
 20. LURJE, A. I.: *Theory of Elasticity*. Nauka, Moscow, 1970. In Russian.
 21. MICHALOWSKI, R. and MRÓZ, Z.: Associated and non-associated sliding rules in contact friction problems. *Archives of Mechanics*, **30**, (1978), 259–276.
 22. SIMO, J. C. and HUGHES, T. J. R.: *Computational Inelasticity*. Springer, New York, Berlin, 1998.
 23. PARK, H. and KIM, K.: Smooth surface approximation to serial cross-sections. *Computer-Aided Design*, **28**, (1999), 995–1005.

VECTOR FORMULAE FOR NON-HOMOGENEOUS PRISMATIC BARS

ISTVÁN ECSEDI

Department of Mechanics, University of Miskolc
H-3515 Miskolc–Egyetemváros, Hungary
mechecs@uni-miskolc.hu

KORNÉL DLUHI

Hewlett-Packard Hungary Ltd.
H-1117, Budapest, Alíz u. 1., Hungary
kornel.dluhi@hp.com

[Received: October 15, 2006]

Abstract. By using the Timoshenko type beam theory a simple solution is obtained for the bending–tension–shearing problem of non-homogeneous prismatic bars. Within this framework the elastic moduli can vary arbitrarily over the bar’s cross section. Vector formulas for normal stress, shear flow and strain variables such as longitudinal strain and curvature for arbitrary cross section are derived. A vector–tensor formulation of the first-order shear deformation theory for thin-walled beams is presented. Applications of formulas obtained are illustrated in the case of thin-walled open and closed cross section deriving the formulas of shear centre and shear rigidity tensor.

Mathematical Subject Classification: 05C38, 15A15

Keywords: Bending, Non-homogeneous, Shear centre, Shear rigidity, Thin-walled, Timoshenko type beam

1. INTRODUCTION

This report is concerned with the tension (compression), bending and shearing of non-homogeneous prismatic bars. The analysis of the present report is based on the Timoshenko type beam theory in which the strain field is equivalent to assuming that plane transverse sections of prismatic bars remain plane after bending, shearing and tension (compression). The material of the bar is linearly elastic, non-homogeneous and isotropic. The material and geometrical properties do not depend on the axial coordinate z . The bar has non-homogeneity only in its cross section. It means that the Young’s modulus E and shear modulus G may depend on the cross-sectional coordinates x and y . This type of non-homogeneity is called cross-sectional non-homogeneity. The definition of the cross-sectional non-homogeneity includes cases when the bar is a composite of different homogeneous materials, so that E and G are piecewise constants on the cross section. Types of these bars are the compound

and reinforced bars. Their discontinuities in material properties should not affect the presented analysis.

A paper by Wang [1] presents the vectorial formulation of bending and shearing of homogeneous prismatic beams with arbitrary cross section. Wang [1] gives a new form of some known relationships changing the component (scalar) formulas by more compact vector formulas. For homogeneous and non-homogeneous beams the governing equations of pure bending are written in coordinate-free invariant forms by Stokes [2, 3]. In the paper by Stokes [4] a matrix formulation is developed to analyse the thermoelastic effect in pure bending of non-homogeneous prismatic bars. The formulation of Wang [1] and Stokes [2, 3] is based on the Bernoulli–Euler type beam theory, where the effect of the shear force to the deformations is neglected, it is assumed that the shear strains vanish.

The analysis of shear deformability of thin-walled beam is a coordinate free version, based on the shear factor tensor, is developed by Romano et al. [5]. Formulae of the position of shear centre derived in the present paper are different from them obtained by Romano et al. [5]. Our formulae are explicit expressions for the centre of shear, while paper by Romano et al. [5] gives implicit formulae for location of centre of shear in general case. Romano et al. [5] did not deal with the determination of the deflection curve of shear deformable thin-walled beams.

2. FORMULATION OF TENSION (COMPRESSION) AND BENDING

Consider a prismatic bar of arbitrary cross section. The longitudinal direction of the bar is denoted by the unit vector \mathbf{e}_z . The cross section of the bar is a connected planar domain A orthogonal to vector \mathbf{e}_z . Under the action of axial force N and the bending moment which is represented by vector \mathbf{M} in the cross section the axial deformation of the bar according to the Timoshenko type beam theory can be written as

$$\varepsilon_z = \varepsilon_0 + \kappa\eta. \quad (2.1)$$

In equation (2.1), ε_z is the normal strain in direction z at point $P(x, y)$ and ε_0 is the value of ε_z at the origin O and κ is the “rate of rotation with respect to z ” of the cross section about axis ξ . In the case of the Bernoulli–Euler type beam theory κ is the curvature of the deformed longitudinal fibre for which $x = y = 0$. The positions of axes ξ and η are unknown (Figure 1), they depend on the loading parameters which are the axial force and the bending moment vector.

Application of Hooke’s law gives the formula of normal stress:

$$\sigma_z = E(x, y) \varepsilon_z = E(x, y) [\varepsilon_0 + \kappa \eta(x, y)]. \quad (2.2)$$

Here, the function $E = E(x, y)$ may be continuous or discontinuous.

The relationship between the coordinates x, y and ξ, η is (Figure 1)

$$\overrightarrow{OP} = \mathbf{R} = x \mathbf{e}_x + y \mathbf{e}_y = \xi \mathbf{n} + \eta \mathbf{m}, \quad (2.3)$$

where $\mathbf{n}, \mathbf{m} = \mathbf{e}_z \times \mathbf{n}$ are unit vectors, in which cross denotes the vectorial product according to Lurje [6] and Malvern [7].

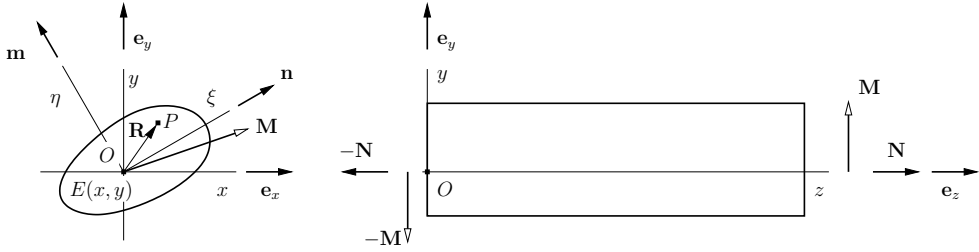


Figure 1. Non-homogeneous bar subjected to axial force and bending moment

The definition of the normal stress vector is as follows

$$\mathbf{t}_z = \sigma_z \mathbf{e}_z = E\varepsilon_0 \mathbf{e}_z + E\kappa \mathbf{n} \times \mathbf{R}, \quad (2.4)$$

since $\mathbf{n} \times \mathbf{R} = \eta \mathbf{e}_z$.

The axial force vector can be computed as

$$\mathbf{N} = N \mathbf{e}_z = \int_A \mathbf{t}_z \, dA = \mathbf{e}_z \varepsilon_0 \int_A E \, dA + \kappa \mathbf{n} \times \int_A E \mathbf{R} \, dA. \quad (2.5)$$

The following designations will be used

$$S = \int_A E(x, y) \, dA, \quad \mathbf{Q} = \int_A E(x, y) \mathbf{R} \, dA. \quad (2.6)$$

It is evident that

$$N = \varepsilon_0 S + \kappa \mathbf{n} \cdot (\mathbf{Q} \times \mathbf{e}_z), \quad (2.7)$$

where the dot denotes the scalar product of two vectors [6, 7, 8].

The expression of the bending moment vector can be derived from the equation

$$\mathbf{M} = \int_A \mathbf{R} \times \mathbf{t}_z \, dA. \quad (2.8)$$

A simple calculation gives

$$\mathbf{M} = \varepsilon_0 \mathbf{Q} \times \mathbf{e}_z + \mathbf{J} \cdot \kappa \mathbf{n}. \quad (2.9)$$

In equation (2.9) the E -weighted moment of inertia tensor of the cross section A about point O is introduced by the following definition

$$\mathbf{J} = \int_A E(x, y) [\mathbf{1}R^2 - \mathbf{R} \circ \mathbf{R}] \, dA. \quad (2.10)$$

In equation (2.10), the dyadic (tensorial) product of two vectors is denoted by a circle and $\mathbf{1}$ is the second order two-dimensional unit tensor [6, 7, 8]. It is clear, that \mathbf{J} is a positive definite symmetrical second order two-dimensional tensor. The validity of this statement follows from equation (2.10).

The principal values of \mathbf{J} are $J_1 \geq J_2 > 0$ and the corresponding principal directions of \mathbf{J} are given by unit vectors \mathbf{e}_1 and \mathbf{e}_2 . We have

$$\mathbf{e}_1 \cdot \mathbf{e}_2 = 0 \quad \text{and} \quad \det \mathbf{J} = J_1 J_2. \quad (2.11)$$

The spectral decomposition of \mathbf{J} and its inverse \mathbf{J}^{-1} can be written as

$$\mathbf{J} = J_1 \mathbf{e}_1 \circ \mathbf{e}_1 + J_2 \mathbf{e}_2 \circ \mathbf{e}_2, \quad \mathbf{J}^{-1} = \frac{1}{J_1} \mathbf{e}_1 \circ \mathbf{e}_1 + \frac{1}{J_2} \mathbf{e}_2 \circ \mathbf{e}_2. \quad (2.12)$$

By the use of the equation written above an identity for \mathbf{J} is derived which will be used later on. A simple computation gives

$$\mathbf{e}_z \times \mathbf{J}^{-1} \times \mathbf{e}_z = - \left[\frac{1}{J_1} \mathbf{e}_2 \circ \mathbf{e}_2 + \frac{1}{J_2} \mathbf{e}_1 \circ \mathbf{e}_1 \right] \quad (2.13)$$

where the following identities have been used for any dyad $\mathbf{a} \circ \mathbf{b}$ with arbitrary \mathbf{c} and \mathbf{d} vectors [6, 7, 8]

$$\mathbf{c} \times (\mathbf{a} \circ \mathbf{b}) \times \mathbf{d} = (\mathbf{c} \times \mathbf{a}) \circ (\mathbf{b} \times \mathbf{d}).$$

The combination of equation (2.11) with equation (2.13) yields

$$\mathbf{e}_z \times \mathbf{J}^{-1} \times \mathbf{e}_z = - \frac{\mathbf{J}}{\det \mathbf{J}}. \quad (2.14)$$

The aim is to get the relationship between the loading parameters N , \mathbf{M} and strain variables ε_0 , $\kappa \mathbf{n}$. Let the origin O be the E -weighted centre C of the cross section which is defined as (Figure 1)

$$\int_A E(x, y) \mathbf{R} \, dA = \mathbf{0}, \quad \mathbf{R} = \overrightarrow{CP}. \quad (2.15)$$

In this case from equations (2.5) and (2.9) it follows that

$$\varepsilon_0 = \frac{N}{S}, \quad \kappa \mathbf{n} = \mathbf{J}^{-1} \cdot \mathbf{M}. \quad (2.16)$$

Combination of equation (2.2) with equation (2.16) yields the formula of normal stress

$$\sigma_z = E(x, y) \left[\frac{N}{S} + \mathbf{M} \cdot \mathbf{J}^{-1} \cdot (\mathbf{R} \times \mathbf{e}_z) \right]. \quad (2.17)$$

Formula (2.17) in the case when $N = 0$ can be considered as a generalisation of the classical bending (flexure) formula [9].

3. SHEAR LOADING OF NON-HOMOGENEOUS BARS

Figure 2 shows a bar segment which is loaded at its end cross sections so that $N = 0$ ($0 \leq z \leq L$). The cylindrical surface of the non-homogeneous bar is traction-free and there are no body forces. Equations of equilibrium of this bar element are as follows (Figure 2)

$$\frac{d\mathbf{F}}{dz} = \mathbf{0}, \quad \frac{d\mathbf{M}}{dz} + \mathbf{e}_z \times \mathbf{F} = \mathbf{0}. \quad (3.1)$$

Here, \mathbf{F} is the internal force and \mathbf{M} is the couple

$$\mathbf{F} = \int_A \boldsymbol{\tau}_z \, dA, \quad \mathbf{M} = \left(\int_A \sigma \mathbf{R} \, dA \right) \times \mathbf{e}_z. \quad (3.2)$$

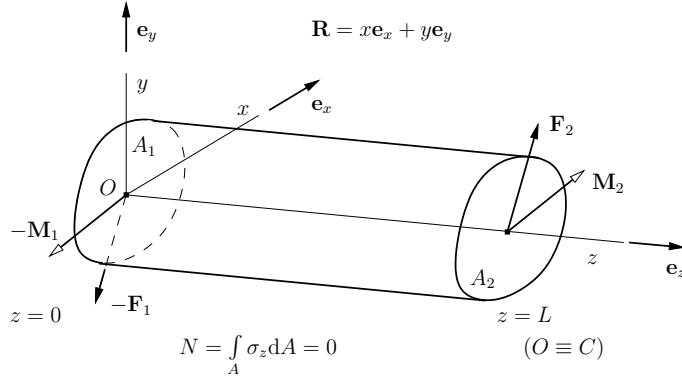


Figure 2. Bending and shear of a non-homogeneous bar

$\boldsymbol{\tau}_z = \tau_{xz}\mathbf{e}_x + \tau_{yz}\mathbf{e}_y$ is the shear stress vector, \mathbf{e}_x and \mathbf{e}_y are unit vectors in the direction of axes x and y , respectively. It should be noticed that the applied loads at the end cross sections A_1 and A_2 satisfy the global conditions of equilibrium (Figure 2)

$$\mathbf{F}_2 - \mathbf{F}_1 = \mathbf{0}, \quad \mathbf{M}_2 - \mathbf{M}_1 + L\mathbf{e}_z \times \mathbf{F}_2 = \mathbf{0}, \quad (3.3)$$

$$\int_{A_2} \mathbf{R} \times \boldsymbol{\tau}_z(x, y, L) \, dA - \int_{A_1} \mathbf{R} \times \boldsymbol{\tau}_z(x, y, 0) \, dA = \mathbf{0}. \quad (3.4)$$

According to the equation of equilibrium the following can be written [6, 7]

$$\frac{\partial \tau_{xz}}{\partial x} + \frac{\partial \tau_{yz}}{\partial y} + \frac{\partial \sigma_z}{\partial z} = 0 \quad (x, y) \in A \quad 0 < z < L, \quad (3.5)$$

$$\tau_{xz}n_x + \tau_{yz}n_y = 0 \quad (x, y) \in \partial A \quad 0 < z < L. \quad (3.6)$$

Here, ∂A is the boundary curve of A and $\mathbf{n} = n_x\mathbf{e}_x + n_y\mathbf{e}_y$ is the unit normal vector of boundary curve ∂A .

Consider the part A^* of the cross section A which is bounded by the line segment \overline{HK} and the boundary segment ∂A^* (Figure 3). From equation (3.5) it follows that

$$\int_{A^*} \left(\frac{\partial \tau_{xz}}{\partial x} + \frac{\partial \tau_{yz}}{\partial y} \right) \, dA = - \int_{A^*} \frac{\partial \sigma_z}{\partial z} \, dA. \quad (3.7)$$

By using Stokes's theorem and the stress boundary condition it can be proved

$$\begin{aligned} \int_{A^*} \left(\frac{\partial \tau_{xz}}{\partial x} + \frac{\partial \tau_{yz}}{\partial y} \right) \, dA &= \int_{\partial A^*} (\tau_{xz}n_x + \tau_{yz}n_y) \, ds + \int_{\overline{HK}} (\tau_{xz}n_x + \tau_{yz}n_y) \, ds \\ &= \int_{\overline{HK}} \boldsymbol{\tau}_z \cdot \mathbf{m} \, ds. \end{aligned} \quad (3.8)$$

In equation (3.8) s is an arc-length defined on $\partial A^* \cup \overline{HK}$ and \mathbf{m} is the unit normal vector to line segment \overline{HK} (Figure 3). The shear flow acting on the line segment \overline{HK}

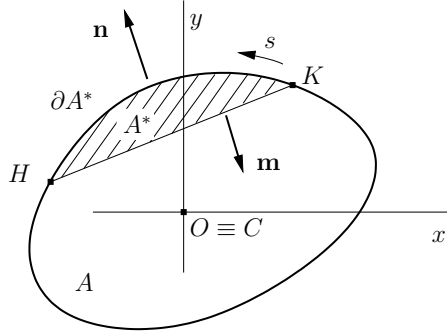


Figure 3. A sketch to the computation of shear flow

is denoted by V_{HK} and it can be computed as

$$V_{HK} = \int_{HK} \boldsymbol{\tau}_z \cdot \mathbf{m} \, ds = - \int_{A^*} \frac{\partial \sigma_z}{\partial z} \, dA. \quad (3.9)$$

Note, that the unit of V_{HK} is force/length. Assuming that $O \equiv C$ and the flexure formula is valid, from equation (2.17) with $N = 0$ follows

$$\frac{\partial \sigma_z}{\partial z} = E \frac{d\mathbf{M}}{dz} \cdot \mathbf{J}^{-1} \cdot (\mathbf{R} \times \mathbf{e}_z). \quad (3.10)$$

Substitution of equation (3.10) into equation (3.9) gives

$$V_{HK} = -(\mathbf{F} \times \mathbf{e}_z) \cdot \mathbf{J}^{-1} \cdot (\mathbf{Q}_{HK} \times \mathbf{e}_z), \quad (3.11)$$

where

$$\mathbf{Q}_{HK} = \int_{A^*} E(x, y) \mathbf{R} \, dA. \quad (3.12)$$

Here, equation (3.1) has been used. The combination of equation (2.14) with equation (3.11) gives the final form of shear flow as

$$V_{HK} = \mathbf{F} \cdot (\mathbf{e}_z \times \mathbf{J}^{-1} \times \mathbf{e}_z) \cdot \mathbf{Q}_{HK} = - \frac{\mathbf{F} \cdot \mathbf{J} \cdot \mathbf{Q}_{HK}}{\det \mathbf{J}}. \quad (3.13)$$

4. SHEAR CENTRE AND SHEAR RIGIDITY OF A THIN-WALLED BEAM WITH OPEN CROSS SECTION

The thin-walled beam of open cross section is loaded by a single force $\mathbf{F} = F_x \mathbf{e}_x + F_y \mathbf{e}_y$ at the end cross section A_2 , while the end cross section A_1 at $z = 0$ is fixed (Figure 4). The centre line of the profile is denoted by c and the thickness of the profile is indicated by $t = t(s)$, where s is an arc-length coordinate defined on c . The origin of the cross-sectional coordinate system Oxy is the E -weighted centre of

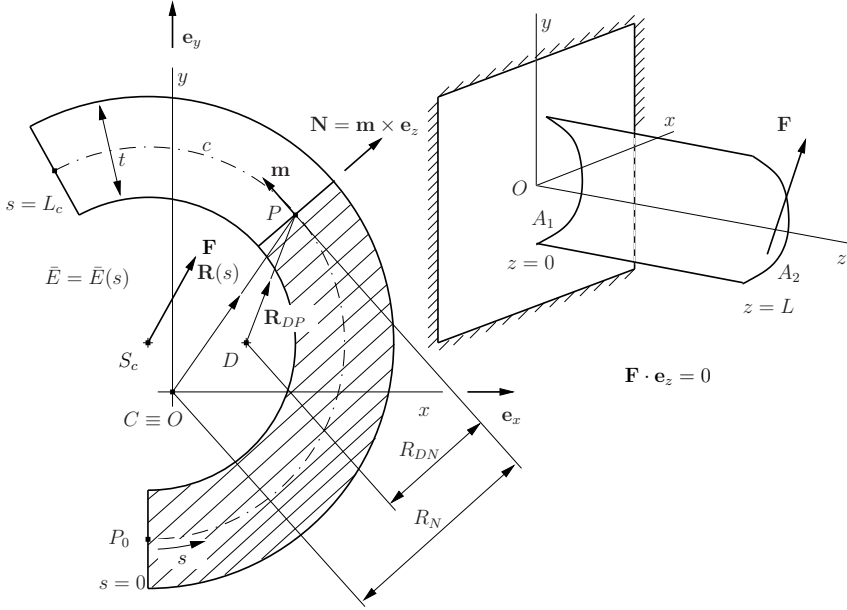


Figure 4. Thin-walled beam with open cross section

the cross section, that is $O \equiv C$. Let ξ denote the thickness coordinate, and \bar{E} is introduced by the definition

$$\bar{E}(s) = \frac{1}{t(s)} \int_{-t/2}^{t/2} E \, d\xi. \quad (4.1)$$

The equation of the centre line of the open profile is

$$\overrightarrow{OP} = \mathbf{R}(s) = X(s) \mathbf{e}_x + Y(s) \mathbf{e}_y. \quad (4.2)$$

It is clear, that the E -weighted second moment of inertia tensor has the form

$$\mathbf{J} = J_x \mathbf{e}_x \circ \mathbf{e}_x - J_{xy} (\mathbf{e}_x \circ \mathbf{e}_y + \mathbf{e}_y \circ \mathbf{e}_x) + J_y \mathbf{e}_y \circ \mathbf{e}_y, \quad (4.3)$$

where

$$J_x = \int_c \bar{E} Y^2 t \, ds, \quad J_y = \int_c \bar{E} X^2 t \, ds, \quad J_{xy} = J_{yx} = \int_c \bar{E} X Y t \, ds. \quad (4.4)$$

The E -weighted first moment of the shaded area about point O is as follows (Figure 4)

$$\mathbf{Q}(s) = \int_{\widehat{P_0P}} \bar{E} \mathbf{R} t \, ds, \quad 0 \leq s \leq L_c. \quad (4.5)$$

It follows that $\mathbf{Q}(0) = \mathbf{Q}(L_c) = \mathbf{0}$ since $O \equiv C$.

In equations (4.5) L_c is the length of the middle curve c .

An equivalent force–couple system at point O to the shear flow

$$V(s) = -\frac{\mathbf{F} \cdot \mathbf{J} \cdot \mathbf{Q}(s)}{\det \mathbf{J}} \quad (4.6)$$

is

$$\mathbf{F} = \int_c V(s) \mathbf{m}(s) \, ds, \quad (4.7)$$

$$\mathbf{T} = \int_c \mathbf{R}(s) \times \mathbf{m}(s) V(s) \, ds = \int_c V(s) \mathbf{R}(s) \times d\mathbf{R}, \quad (4.8)$$

since

$$\mathbf{m}(s) = \frac{d\mathbf{R}}{ds}. \quad (4.9)$$

According to Figure 4

$$\begin{aligned} \mathbf{R} \times d\mathbf{R} &= \mathbf{R} \times \mathbf{m} \, ds = \mathbf{R} \times (\mathbf{e}_z \times \mathbf{N}) \, ds = \\ &= \mathbf{e}_z (\mathbf{R} \cdot \mathbf{N}) \, ds - \mathbf{N} (\mathbf{R} \cdot \mathbf{e}_z) \, ds = R_N \mathbf{e}_z \, ds, \end{aligned} \quad (4.10)$$

where

$$R_N = \mathbf{R} \cdot \mathbf{N}. \quad (4.11)$$

Introducing equation (4.6) into equation (4.8) yields

$$\mathbf{T} = \mathbf{e}_z \int_c V(s) R_N \, ds = -\frac{\mathbf{F} \cdot \mathbf{J} \cdot \int_c \mathbf{Q}(s) R_N \, ds}{\det \mathbf{J}} \mathbf{e}_z. \quad (4.12)$$

Integration by parts gives the result

$$\int_c \mathbf{Q}(s) R_N(s) \, ds = [\mathbf{Q}(s) \omega(s)]_0^{L_c} - \int_c \frac{d\mathbf{Q}}{ds} \omega(s) \, ds = - \int_c \bar{E} \mathbf{R} \omega \, ds \quad (4.13)$$

since

$$\omega(s) = \int_{\widehat{P_0P}} R_N \, ds, \quad \frac{d\mathbf{Q}}{ds} = \bar{E}(s) \mathbf{R} t \quad (4.14)$$

and $\mathbf{Q}(0) = \mathbf{Q}(L_c) = \mathbf{0}$. A new cross-sectional property \mathbf{Q}_ω is introduced as

$$\mathbf{Q}_\omega = \int_c \bar{E}(s) \mathbf{R}(s) \omega(s) t(s) \, ds. \quad (4.15)$$

From equation (4.10) and (4.14) follows that

$$\mathbf{T} = \frac{\mathbf{F} \cdot \mathbf{J} \cdot \mathbf{Q}_\omega}{\det \mathbf{J}} \mathbf{e}_z. \quad (4.16)$$

It is very easy to show that

$$\mathbf{F} \times (\mathbf{e}_z \times (\mathbf{J} \cdot \mathbf{Q}_\omega)) = \mathbf{e}_z (\mathbf{F} \cdot \mathbf{J} \cdot \mathbf{Q}_\omega), \quad (4.17)$$

since $\mathbf{F} \cdot \mathbf{e}_z = 0$.

By the application of equation (4.17) a new form of the couple (torque) vector \mathbf{T} can be derived

$$\mathbf{T} = \mathbf{F} \times \left[\frac{\mathbf{e}_z \times \mathbf{J} \cdot \mathbf{Q}_\omega}{\det \mathbf{J}} \right]. \quad (4.18)$$

The shear flow is caused by the shear force \mathbf{F} whose point of application is the shear centre S_c . It is clear, that \mathbf{T} can be computed as

$$\mathbf{T} = \overrightarrow{OS_c} \times \mathbf{F}. \quad (4.19)$$

Comparing two expressions of \mathbf{T} which are given by equations (4.18) and (4.19) a vector formula can be obtained to determine the position of the shear centre

$$\overrightarrow{OS_c} = -\frac{\mathbf{e}_z \times \mathbf{J} \cdot \mathbf{Q}_\omega}{\det \mathbf{J}}, \quad (O \equiv C). \quad (4.20)$$

For homogeneous beams, the scalar version of formula (4.20) is identical to which can be found in Vlasov's book [10].

The derivation of the shear stiffness of the open profile is based on the expression of shear strain energy. The shear strain energy per unit length of the non-homogeneous beam is [10, 11]

$$U_s = \frac{1}{2} \int_c \int_{-t/2}^{t/2} \frac{\tau_z^2}{G} d\xi ds = \frac{1}{2} \int_c \frac{\tau^2}{\bar{G}} t ds = \frac{1}{2} \int_c \frac{[V(s)]^2}{\bar{G}t} ds. \quad (4.21)$$

Here, $\bar{G}(s)$ is introduced by the next definition

$$\frac{t(s)}{\bar{G}(s)} = \int_{-t/2}^{t/2} \frac{d\xi}{G}. \quad (4.22)$$

A simple computation shows that

$$V^2 = \left[\frac{\mathbf{F} \cdot \mathbf{J} \cdot \mathbf{Q}(s)}{\det \mathbf{J}} \right]^2 = \frac{\mathbf{F} \cdot \mathbf{J} \cdot (\mathbf{Q} \circ \mathbf{Q}) \cdot \mathbf{J} \cdot \mathbf{F}}{(\det \mathbf{J})^2}. \quad (4.23)$$

Defining the tensor \mathbf{W} as

$$\mathbf{W} = \int_c \frac{\mathbf{Q}(s) \circ \mathbf{Q}(s)}{\bar{G}(s)t(s)} ds \quad (4.24)$$

and using equation (4.23) it follows that

$$U_s = \frac{1}{2} \mathbf{F} \cdot \mathbf{H}_s \cdot \mathbf{F}, \quad (4.25)$$

where \mathbf{H}_s is the shear flexibility tensor

$$\mathbf{H}_s = \frac{\mathbf{J} \cdot \mathbf{W} \cdot \mathbf{J}}{(\det \mathbf{J})^2}. \quad (4.26)$$

The shear rigidity tensor \mathbf{C}_s is the inverse of \mathbf{H}_s , that is

$$\mathbf{C}_s = \mathbf{H}_s^{-1}. \quad (4.27)$$

The principal directions of bending are the principal axes of E -weighted second moment of inertia tensor computed to point C . The principal directions of shear deformation are the principal axes of the shear rigidity (flexibility) tensor. From equation (4.26) it follows that in general, the principal directions of bending deformation and the principal directions of shear deformation have different orientations. The principal directions of bending and shear deformations coincide only if \mathbf{J} and \mathbf{W} have the same eigenvectors. In the case of symmetric cross sections this latter

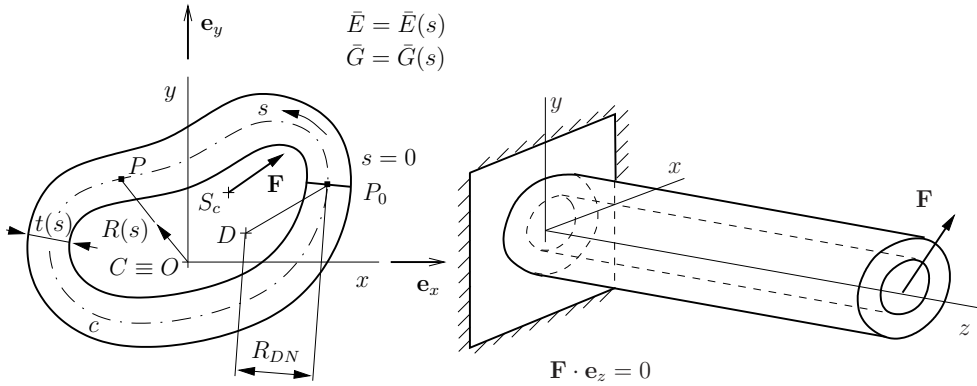


Figure 5. Thin-walled beam with closed cross section

statement is valid, that is the principal directions of bending and shear deformations coincide.

5. SHEAR CENTRE AND SHEAR RIGIDITY OF A THIN-WALLED BEAM WITH CLOSED CROSS SECTION

For a single cell closed thin-walled tube shown in Figure 5 the shear flow $V = V(s)$ at any point s is

$$V(s) = V_0 - \frac{\mathbf{F} \cdot \mathbf{J} \cdot \mathbf{Q}(s)}{\det \mathbf{J}}, \tag{5.1}$$

where V_0 is the value of V at $s = 0$ and s is an arc-length coordinate measured along the centre line c . In order to find the shear flow caused by the shear force \mathbf{F} , it is necessary to determine V_0 . In the literature of thin-walled beams it is customary to define the torsion-free bending of the tube as one in which the value of V_0 is chosen so, that the strain energy stored in the tube is minimal [11]. This condition leads to the equation

$$\int_c \frac{V(s)}{Gt} ds = 0. \tag{5.2}$$

From equations (5.1) and (5.2) the following can be derived

$$V_0 = \frac{\mathbf{F} \cdot \mathbf{J} \cdot \int_c \frac{\mathbf{Q}(s)}{Gt} ds}{\det \mathbf{J} \int_c \frac{ds}{Gt}}. \tag{5.3}$$

Note, that the thin-walled tube is axially homogeneous, i.e. all material and geometrical properties do not change in the direction of axis z .

The derivation of the next identity is based on integration by parts

$$\int_c \frac{\mathbf{Q}(s)}{Gt} ds = - \int_c \left(\int_0^s \frac{d\lambda}{Gt} \right) \bar{\mathbf{E}} \mathbf{R} t ds. \tag{5.4}$$

The point of application of the end load \mathbf{F} , at which the twist is not developed, is denoted by S_c . Point S_c is the shear centre of thin-walled beams with closed profile. The torque about point $O \equiv C$ obtained from \mathbf{F} is

$$\mathbf{T} = \overrightarrow{OS_c} \times \mathbf{F}. \quad (5.5)$$

The expression of the same torque in terms of shear flow in the case of torsion-free bending is as follows

$$\mathbf{T} = \mathbf{e}_z \int_c R_N(s) V(s) ds. \quad (5.6)$$

From equations (5.1), (5.3), (5.4) and from the comparison of the results formulated in equations (5.5) and (5.6) follows

$$\overrightarrow{OS_c} = -\frac{\mathbf{e}_z \times \mathbf{J} \cdot \mathbf{Q}_\Omega}{\det \mathbf{J}} \quad (O \equiv C), \quad (5.7)$$

where

$$\Omega(s) = \omega(s) - \frac{2A_c}{\int_c \frac{ds}{\tilde{G}t}} \int_0^s \frac{d\lambda}{\tilde{G}t}, \quad (5.8)$$

A_c is the area enclosed by the middle curve c ,

$$\mathbf{Q}_\Omega = \int_c \bar{E}R\Omega t ds. \quad (5.9)$$

In order to get the expression of shear stiffness \mathbf{c}_s the expression of shear strain energy per unit length of the non-homogeneous thin-walled tube is introduced, which is [10, 11]

$$U_s = \frac{1}{2} \int_c \frac{[V(s)]^2}{\tilde{G}t} ds. \quad (5.10)$$

Here,

$$[V(s)]^2 = \left[\frac{\mathbf{F} \cdot \mathbf{J} \cdot \mathbf{q}(s)}{\det \mathbf{J}} \right]^2 = \frac{\mathbf{F} \cdot \mathbf{J} \cdot (\mathbf{q}(s) \circ \mathbf{q}(s)) \cdot \mathbf{J} \cdot \mathbf{F}}{(\det \mathbf{J})^2}, \quad (5.11)$$

$$\mathbf{q}(s) = \frac{\int_c \frac{\mathbf{Q}}{\tilde{G}t} ds}{\int_c \frac{ds}{\tilde{G}t}} - \mathbf{Q}(s). \quad (5.12)$$

We introduce the tensor \mathbf{w} as

$$\mathbf{w} = \int_c \frac{\mathbf{q}(s) \circ \mathbf{q}(s)}{\tilde{G}(s)t(s)} ds. \quad (5.13)$$

Inserting equations (5.11) and (5.13) into the formula of U_s results in

$$U_s = \frac{1}{2} \mathbf{F} \cdot \mathbf{h}_s \cdot \mathbf{F}, \quad (5.14)$$

where \mathbf{h}_s is the shear flexibility tensor of the non-homogeneous thin-walled tube. Expression of \mathbf{h}_s is

$$\mathbf{h}_s = \frac{\mathbf{J} \cdot \mathbf{w} \cdot \mathbf{J}}{(\det \mathbf{J})^2}. \quad (5.15)$$

The shear rigidity tensor \mathbf{c}_s is the inverse of \mathbf{h}_s , that is

$$\mathbf{c}_s = \mathbf{h}_s^{-1}. \quad (5.16)$$

Following the discussion on the coincidence of principal directions of bending and shear deformations given at the end of Section 4 the next statement can be formulated. The principal directions of bending and shear deformations for the non-homogeneous thin-walled tube will be the same only if \mathbf{J} and \mathbf{w} have the same eigenvectors.

6. REMARK TO THE COMPUTATION OF THE CENTRE OF SHEAR

6.1. Open cross section. Here, a new formula is derived to obtain the position of the centre of shear S_c relative to an arbitrary point D . According to Figure 4 and formula (4.12)

$$\overrightarrow{DS_c} \times \mathbf{F} = -\frac{\mathbf{F} \cdot \mathbf{J} \cdot \int_c \mathbf{Q}(s) R_{DN}(s) ds}{\det \mathbf{J}} \mathbf{e}_z, \quad (6.1)$$

where $R_{DN} = \overrightarrow{DS_c} \cdot \mathbf{N}$. From equation (6.1) it follows that

$$\mathbf{F} \cdot \left\{ \mathbf{e}_z \times \overrightarrow{DS_c} + \frac{\mathbf{J} \cdot \int_c \mathbf{Q}(s) R_{DN}(s) ds}{\det \mathbf{J}} \right\} = 0. \quad (6.2)$$

Combination of equation (6.2) with the next identity

$$(\mathbf{e}_z \times \overrightarrow{DS_c}) \times \mathbf{e}_z = \overrightarrow{DS_c} \quad (6.3)$$

gives

$$\overrightarrow{DS_c} = \frac{\mathbf{e}_z \times \mathbf{J} \cdot \int_c \mathbf{Q}(s) R_{DN}(s) ds}{\det \mathbf{J}}. \quad (6.4)$$

6.2. Closed cross section. In the case of closed profile a new formula can be derived by the same method to determine the position of the centre of shear S_c relative to an arbitrary point D . Here, equations (5.1) and (5.3) are used. A detailed computation yields the next result (Figure 5)

$$\overrightarrow{DS_c} = \frac{\mathbf{e}_z \times \mathbf{J} \cdot \int_c \mathbf{Q}(s) R_{DN}(s) ds}{\det \mathbf{J}} - \frac{\mathbf{e}_z \times \mathbf{J} \cdot \int_c \frac{\mathbf{Q}(s)}{Gt} ds}{\det \mathbf{J}} \frac{2A_c}{\int_c \frac{ds}{Gt}}. \quad (6.5)$$

Note, that in equations (6.4) and (6.5) \mathbf{J} and $\mathbf{Q} = \mathbf{Q}(s)$ refer to the E -weighted centre of the cross section.

7. DEFLECTION CURVE OF SHEAR DEFORMABLE THIN-WALLED NON-HOMOGENEOUS BEAMS

It is assumed that the displacements and strains are small and the form of the displacement field is

$$\mathbf{u}(x, y, z) = \mathbf{U}(z) + [w_0(z) + (\mathbf{e}_z \times \boldsymbol{\psi}(z)) \cdot \mathbf{R}] \mathbf{e}_z, \quad (7.1)$$

where $\mathbf{U}(z) = U(z) \mathbf{e}_x + V(z) \mathbf{e}_y$ is the transverse displacement vector of the E -weighted centre of the cross section and $w_0 = w_0(z)$ is the axial displacement of the E -weighted centre of the cross section while $\boldsymbol{\psi} = \psi_x(z) \mathbf{e}_x + \psi_y(z) \mathbf{e}_y$ describes the

“rigid” rotation of cross sections according to Timoshenko’s beam theory. From the strain–displacement relationships of the linearized theory of elasticity [6, 7, 8] follows

$$\varepsilon_x = \varepsilon_y = \gamma_{xy} = 0, \quad \varepsilon_z = \frac{\partial w_0}{\partial z} + \left(\mathbf{e}_z \times \frac{d\boldsymbol{\psi}}{dz} \right) \cdot \mathbf{R}, \quad (7.2)$$

$$\gamma_{xz} = \frac{dU}{dz} + (\mathbf{e}_z \times \boldsymbol{\psi}) \cdot \mathbf{e}_x, \quad \gamma_{yz} = \frac{dV}{dz} + (\mathbf{e}_z \times \boldsymbol{\psi}) \cdot \mathbf{e}_y. \quad (7.3)$$

The shear strain vector $\boldsymbol{\gamma}_z$ is introduced as

$$\boldsymbol{\gamma}_z = \gamma_{xz} \mathbf{e}_x + \gamma_{yz} \mathbf{e}_y = \frac{d\mathbf{U}}{dz} + \mathbf{e}_z \times \boldsymbol{\psi}. \quad (7.4)$$

It follows from the obtained strain components that the displacement field formulated in equation (7.1) satisfies the requirements of Timoshenko’s beam theory, i.e. the cross sections remain planes and the shear strains do not vanish. The shear strain vector on a cross section is constant, since it depends only on axial coordinate z . According to this statement the beam theory based on the displacement field (7.1) is a first-order shear deformation beam theory [12]. It should be emphasised that axis z is the centre line of the non-homogeneous beam, that is it connects the E -weighted centre of the cross sections. Internal forces in a cross section can be decomposed into two parts as

$$\mathbf{F} = \mathbf{S} + \mathbf{e}_z N, \quad \mathbf{S} \cdot \mathbf{e}_z = 0, \quad (7.5)$$

where N is the axial force and \mathbf{S} is the shear force vector. According to equation (7.5) the applied distributed load is resolved as

$$\mathbf{f} = \mathbf{s} + \mathbf{e}_z n, \quad \mathbf{s} \cdot \mathbf{e}_z = 0. \quad (7.6)$$

Force equilibrium equations can be written in the form

$$\frac{dN}{dz} + n = 0, \quad \frac{d\mathbf{S}}{dz} + \mathbf{s} = \mathbf{0} \quad 0 < z < L. \quad (7.7)$$

Next, it is assumed that $n(z) = 0$ ($0 < z < L$) and $N(0) = 0$, that is $N(z) = 0$ ($0 \leq z \leq L$).

The moment of internal forces about point S_c is $\mathbf{M} = \mathbf{M}(z)$. It is assumed that there is no torsional load present, that is

$$\mathbf{M} \cdot \mathbf{e}_z = 0 \quad \text{and} \quad \mathbf{m} \cdot \mathbf{e}_z = 0. \quad (7.8)$$

In equation (7.8) $\mathbf{m} = \mathbf{m}(z)$ is the moment of the applied distributed transverse load about point S_c . The moment equilibrium equation has the form

$$\frac{d\mathbf{M}}{dz} + \mathbf{e}_z \times \mathbf{S} + \mathbf{m} = \mathbf{0}. \quad (7.9)$$

From equations (2.1) and (7.2) it follows that

$$\varepsilon_z = \varepsilon_0 + \kappa\eta = \varepsilon_0 + (\mathbf{e}_z \times \kappa\mathbf{n}) \cdot \mathbf{R} = \frac{dw_0}{dz} + \left(\mathbf{e}_z \times \frac{d\boldsymbol{\psi}}{dz} \right) \cdot \mathbf{R}, \quad (7.10)$$

that is

$$\varepsilon_0 = \frac{dw_0}{dz}, \quad \kappa\mathbf{n} = \frac{d\boldsymbol{\psi}}{dz}. \quad (7.11)$$

On the other hand, the following holds

$$\varepsilon_0 = \frac{N}{S} = 0 \quad 0 \leq z \leq L \quad (7.12)$$

in the present case. According to equations (7.11) and (7.12), without the loss of generality it can be assumed that

$$w_0(z) = 0 \quad 0 \leq z \leq L. \quad (7.13)$$

Expression of \mathbf{M} in terms of $\boldsymbol{\psi}$ is as follows

$$\mathbf{M} = \mathbf{J} \cdot \frac{d\boldsymbol{\psi}}{dz}. \quad (7.14)$$

In order to get the relationship between shear force \mathbf{S} and shear strain $\boldsymbol{\gamma}_z$ the expression of shear strain energy per unit length of non-homogeneous beams is considered

$$U_s = \frac{1}{2} \int_A \boldsymbol{\tau}_z \cdot \boldsymbol{\gamma}_z \, dA = \frac{1}{2} \mathbf{S} \cdot \boldsymbol{\gamma}_z = \frac{1}{2} \mathbf{S} \cdot \mathbf{H} \cdot \mathbf{S}. \quad (7.15)$$

For open cross section $\mathbf{H} = \mathbf{H}_s$, and for closed cross section (tube) $\mathbf{H} = \mathbf{h}_s$. equation (7.15) yields

$$\boldsymbol{\gamma}_z = \mathbf{H} \cdot \mathbf{S} \quad \text{or} \quad \mathbf{S} = \mathbf{C} \cdot \boldsymbol{\gamma}_z, \quad (7.16)$$

where $\mathbf{C} = \mathbf{H}^{-1}$ is the shear rigidity tensor.

Here, we note, that the shear strain vector $\boldsymbol{\gamma}_z$ represented by equation (7.4) is constant on the cross section, from this it follows that the shear stress vector $\boldsymbol{\tau}_z$ will also be constant. The discrepancy between the stress state compatible with the equilibrium equations (formula (3.13)) and the constant stress state of the first order shear deformation theory can be overcome approximately by introducing the shear rigidity tensor to obtain the shear strain vector $\boldsymbol{\gamma}_z$ according to equation (7.16).

From equation (7.9) it follows that

$$\frac{d}{dz}(\mathbf{e}_z \times \mathbf{M}) - \mathbf{S} + \mathbf{e}_z \times \mathbf{m} = \mathbf{0}. \quad (7.17)$$

Integration of equations (7.7) and (7.17) gives

$$\mathbf{S} = - \int_0^z \mathbf{s}(\xi_1) \, d\xi_1 + \mathbf{c}_1, \quad (7.18)$$

$$\mathbf{e}_z \times \mathbf{M} = - \int_0^z \int_0^{\xi_2} \mathbf{s}(\xi_1) \, d\xi_1 \, d\xi_2 - \int_0^z \mathbf{e}_z \times \mathbf{m}(\xi_1) \, d\xi_1 + \mathbf{c}_1 z + \mathbf{c}_2. \quad (7.19)$$

Here, \mathbf{c}_1 and \mathbf{c}_2 are the constants of integration ($\mathbf{c}_1 \cdot \mathbf{e}_z = \mathbf{c}_2 \cdot \mathbf{e}_z = 0$). A new kinematical quantity $\boldsymbol{\phi} = \boldsymbol{\phi}(z)$ is introduced as

$$\boldsymbol{\phi}(z) = \mathbf{e}_z \times \boldsymbol{\psi}(z). \quad (7.20)$$

It is evident, that

$$\boldsymbol{\psi}(z) = -\mathbf{e}_z \times \boldsymbol{\phi}(z). \quad (7.21)$$

A simple calculation shows that

$$\mathbf{e}_z \times \mathbf{M}(z) = \mathbf{e}_z \times \mathbf{J} \cdot \frac{d\boldsymbol{\psi}}{dz} = -(\mathbf{e}_z \times \mathbf{J} \times \mathbf{e}_z) \cdot \frac{d\boldsymbol{\phi}}{dz} = (\det \mathbf{J}) \mathbf{J}^{-1} \cdot \frac{d\boldsymbol{\phi}}{dz}. \quad (7.22)$$

Here, equation (2.14) has been used for “ \mathbf{J}^{-1} ”. Inserting equation (7.22) into equation (7.19) yields

$$\frac{d\phi}{dz} = \frac{\mathbf{J}}{\det \mathbf{J}} \cdot \left\{ - \int_0^z \int_0^{\xi_2} \mathbf{s}(\xi_1) d\xi_1 d\xi_2 - \int_0^z \mathbf{e}_z \times \mathbf{m}(\xi_1) d\xi_1 + \mathbf{c}_1 z + \mathbf{c}_2 \right\}. \quad (7.23)$$

Integrating equation (7.23) with respect to z results in

$$\begin{aligned} \phi(z) = \frac{\mathbf{J}}{\det \mathbf{J}} \cdot \left\{ - \int_0^z \int_0^{\xi_3} \int_0^{\xi_2} \mathbf{s}(\xi_1) d\xi_1 d\xi_2 d\xi_3 - \int_0^z \int_0^{\xi_3} \mathbf{e}_z \times \mathbf{m}(\xi_1) d\xi_1 d\xi_2 \right. \\ \left. + \frac{\mathbf{c}_1}{2} z^2 + \mathbf{c}_2 z \right\} + \mathbf{c}_3. \end{aligned} \quad (7.24)$$

From equations (7.4), (7.16) and (7.18) the next equation can be derived

$$\mathbf{H} \cdot \mathbf{S} = \mathbf{H} \cdot \left(- \int_0^z \mathbf{s}(\xi_1) d\xi_1 + \mathbf{c}_1 \right) = \frac{d\mathbf{U}}{dz} + \phi. \quad (7.25)$$

Substituting $\phi = \phi(z)$ in equation (7.25) and integrating it once more with respect to z results in

$$\begin{aligned} \mathbf{U}(z) = - \frac{\mathbf{J}}{\det \mathbf{J}} \cdot \left\{ - \int_0^z \int_0^{\xi_4} \int_0^{\xi_3} \int_0^{\xi_2} \mathbf{s}(\xi_1) d\xi_1 d\xi_2 d\xi_3 d\xi_4 \right. \\ \left. - \int_0^z \int_0^{\xi_3} \int_0^{\xi_2} \mathbf{e}_z \times \mathbf{m}(\xi_1) d\xi_1 d\xi_2 d\xi_3 + \frac{1}{6} \mathbf{c}_1 z^3 + \frac{1}{2} \mathbf{c}_2 z^2 \right\} - \mathbf{c}_3 z + \mathbf{c}_4 \\ + \mathbf{H} \cdot \left(- \int_0^z \int_0^{\xi_2} \mathbf{s}(\xi_1) d\xi_1 d\xi_2 + \mathbf{c}_1 z \right). \end{aligned} \quad (7.26)$$

The transverse deflection vector $\mathbf{U} = \mathbf{U}(z)$ consists of two parts, $\mathbf{U} = \mathbf{U}_B + \mathbf{U}_S$, where the bending part \mathbf{U}_B is

$$\begin{aligned} \mathbf{U}_B = \frac{\mathbf{J}}{\det \mathbf{J}} \cdot \left\{ \int_0^z \int_0^{\xi_4} \int_0^{\xi_3} \int_0^{\xi_2} \mathbf{s}_0(\xi_1) d\xi_1 d\xi_2 d\xi_3 d\xi_4 \right. \\ \left. + \int_0^z \int_0^{\xi_3} \int_0^{\xi_2} \mathbf{e}_z \times \mathbf{m}(\xi_1) d\xi_1 d\xi_2 d\xi_3 - \frac{1}{6} \mathbf{c}_1 z^3 - \frac{1}{2} \mathbf{c}_2 z^2 \right\} - \mathbf{c}_3 z + \mathbf{c}_4 \end{aligned} \quad (7.27)$$

and the shear part of \mathbf{U} is \mathbf{U}_S

$$\mathbf{U}_S = \mathbf{H} \cdot \left(- \int_0^z \int_0^{\xi_2} \mathbf{s}(\xi_1) d\xi_1 d\xi_2 + \mathbf{c}_1 z \right). \quad (7.28)$$

The bending part $\mathbf{U}_B = \mathbf{U}_B(z)$ is the same that can be derived from the classical Euler–Bernoulli’s beam theory. When the shear stiffness tends to infinity, the shear strain vector γ_z goes to zero vector, that is

$$\mathbf{e}_z \times \boldsymbol{\psi} = \phi = - \frac{d\mathbf{U}}{dz}. \quad (7.29)$$

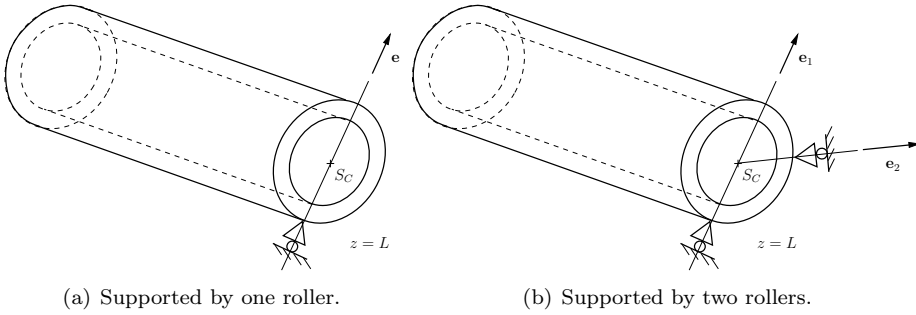


Figure 6. Simply supported end cross sections ($a = L$)

If equation (7.29) is valid, the Timoshenko's beam theory reduces to the classical Euler–Bernoulli's beam theory [12].

Associated boundary conditions to equations (7.18), (7.19), (7.24) and (7.26) are as follows

- for fixed support: $\mathbf{U}(a) = \mathbf{0}$, $\phi(a) = \mathbf{0}$ ($a = 0$ or $a = L$);
- for loaded end cross section: $\mathbf{M}(a) = \tilde{\mathbf{M}}$, $\mathbf{S}(a) = \tilde{\mathbf{S}}$ ($a = 0$ or $a = L$), here $\tilde{\mathbf{M}}$ and $\tilde{\mathbf{S}}$ are prescribed;
- for free end cross section: $\mathbf{M}(a) = \mathbf{0}$, $\mathbf{S}(a) = \mathbf{0}$ ($a = 0$ or $a = L$);
- for simply supported end cross section by one roller as shown in Figure 6(a): $\mathbf{U}(a) \cdot \mathbf{e} = 0$, $\mathbf{M}(a) = \mathbf{0}$, $(\mathbf{e}_z \times \mathbf{S}(a)) \cdot \mathbf{e} = 0$ ($a = 0$ or $a = L$);
- for end cross section supported by two rollers as shown in Figure 6(b): $\mathbf{U}(a) = \mathbf{0}$, $\mathbf{M}(a) = \mathbf{0}$. The common point of lines of action of rollers is the centre of shear of considered end cross section.

8. NUMERICAL EXAMPLES

8.1. Shear centre and shear rigidity of a slitted rectangular tube. The thickness of cross section shown in Figure 7 is uniform but the walls are made of different materials. Using data given in Figure 7 results in

$$\overrightarrow{DC} = \begin{pmatrix} 0.065 \\ 0.098 \end{pmatrix} \text{ m}, \quad \mathbf{J} = \begin{pmatrix} 721046 & -50597.6 \\ -50597.6 & 798352 \end{pmatrix} \text{ Nm}^2, \quad \overrightarrow{DS_C} = \begin{pmatrix} 0.219 \\ -0.053 \end{pmatrix} \text{ m}.$$

A simple computation gives

$$\mathbf{H}_s = \begin{pmatrix} 1.216\text{E-}07 & 7.633\text{E-}08 \\ 7.633\text{E-}08 & 1.066\text{E-}07 \end{pmatrix} \frac{1}{\text{N}}, \quad \mathbf{C}_s = \begin{pmatrix} 1.491\text{E+}07 & -1.067\text{E+}07 \\ -1.067\text{E+}07 & 1.702\text{E+}07 \end{pmatrix} \text{ N}.$$

The principal directions of bending deformation (eigenvectors of \mathbf{J}) are

$$\mathbf{b}_1 = \begin{pmatrix} -0.896398 \\ -0.44325 \end{pmatrix}, \quad \mathbf{b}_2 = \begin{pmatrix} -0.44325 \\ 0.896398 \end{pmatrix}.$$

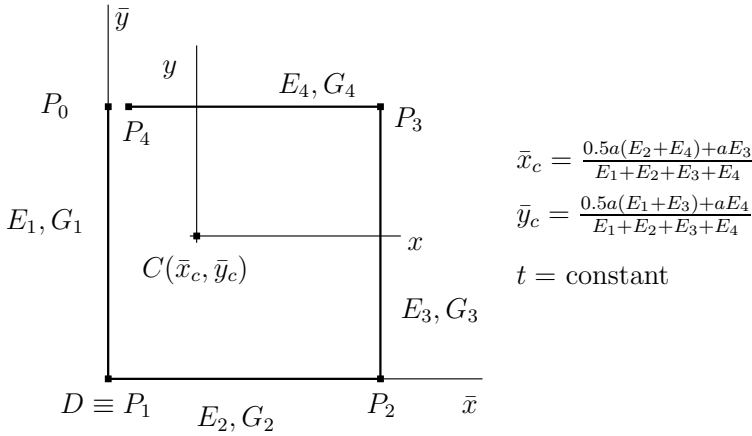


Figure 7. Slitted rectangular thin-walled tube. Data: $a = 160$ mm, $t = 2$ mm, $E_1 = E_4 = 2.1 \times 10^5$ MPa, $E_2 = 0.7 \times 10^5$ MPa, $E_3 = 1.05 \times 10^5$ MPa, $G_1 = G_4 = 0.8 \times 10^5$ MPa, $G_2 = 0.27 \times 10^5$ MPa, $G_3 = 0.39 \times 10^5$ MPa, $\overline{P_0P_1} = \overline{P_1P_2} = a$

The principal directions of shear deformation (eigenvectors of \mathbf{C}_s) are

$$\mathbf{S}_1 = \begin{pmatrix} -0.741031 \\ -0.67147 \end{pmatrix}, \quad \mathbf{S}_2 = \begin{pmatrix} 0.67147 \\ -0.741031 \end{pmatrix}.$$

In this example the principal directions of bending and shear deformations are significantly different.

8.2. Shear centre and shear rigidity of a closed rectangular tube. The middle curve of the closed tube is the same as above (Figure 7), but $P_0 \equiv P_4$, i.e. there is no cut at point P_0 . By the use of data given in Figure 7 the next results are obtained

$$\overrightarrow{DS_c} = \begin{pmatrix} 0.054 \\ 0.123 \end{pmatrix} \text{ m}, \quad \mathbf{h}_s = \begin{pmatrix} 3.775\text{E-}08 & -1.841\text{E-}09 \\ -1.841\text{E-}09 & 3.381\text{E-}08 \end{pmatrix} \frac{1}{\text{N}},$$

$$\mathbf{c}_s = \begin{pmatrix} 2.655\text{E+}07 & 1.446\text{E+}06 \\ 1.446\text{E+}06 & 2.965\text{E+}07 \end{pmatrix} \text{ N}.$$

The principal directions of bending deformation for open and closed cross sections are the same. The principal directions of shear deformation (eigenvectors of \mathbf{c}_s) are

$$\mathbf{s}_1 = \begin{pmatrix} -0.930169 \\ 0.367131 \end{pmatrix}, \quad \mathbf{s}_2 = \begin{pmatrix} -0.367131 \\ -0.930169 \end{pmatrix}.$$

8.3. Deflection curve of a cantilever thin-walled beam with open cross section. Consider a cantilever beam of length L fixed at $z = 0$ (Figure 8). The data of the “L” shape cross section is obtained from the data of the cross section shown in Figure 7. Here, $a = 160$ mm, $t = 2$ mm, $E_1 = 2.1 \times 10^5$ MPa, $E_2 = 0.7 \times 10^5$ MPa,

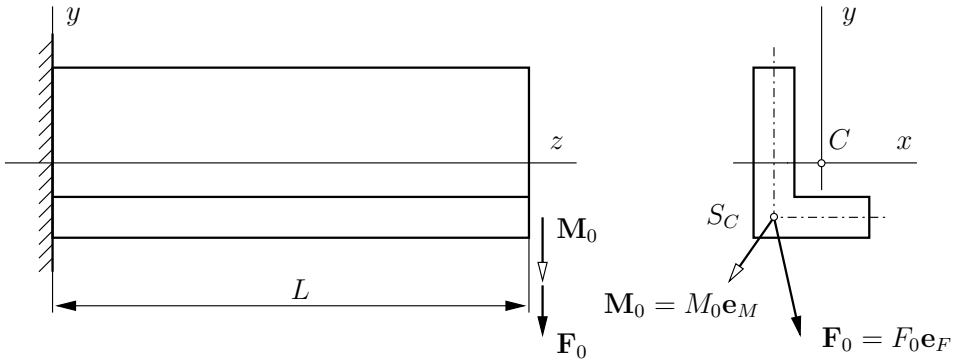


Figure 8. Cantilever thin-walled beam with open profile

$E_3 = E_4 = 0$, $G_1 = 0.8 \times 10^5$ MPa, $G_2 = 0.27 \times 10^5$ MPa, $G_3 = G_4 = 0$. The determination of the deflection vector $\mathbf{U} = \mathbf{U}(z)$ and the vector $\boldsymbol{\phi} = \boldsymbol{\phi}(z)$ is based on equations (7.18), (7.19), (7.24), (7.27) and the associated boundary conditions

$$\mathbf{U}(0) = \mathbf{0}, \quad \boldsymbol{\phi}(0) = \mathbf{0}, \quad \mathbf{S}(L) = \mathbf{F}_0, \quad \mathbf{M}(L) = \mathbf{M}_0. \quad (8.1)$$

It is clear, that in the present problem $\mathbf{s} = \mathbf{0}$ and $\mathbf{m} = \mathbf{0}$. A detailed computation gives the next results:

$$\mathbf{c}_1 = F_0 \mathbf{e}_F, \quad \mathbf{c}_2 = \mathbf{e}_z \times \mathbf{e}_M M_0 - L F_0 \mathbf{e}_F, \quad \mathbf{c}_3 = \mathbf{0}, \quad \mathbf{c}_4 = \mathbf{0}; \quad (8.2)$$

$$\boldsymbol{\phi}(z) = \frac{\mathbf{J}}{\det \mathbf{J}} \cdot \left\{ F_0 \left(\frac{z^2}{2} - Lz \right) \mathbf{e}_F + M_0 z \mathbf{e}_z \times \mathbf{e}_M \right\}, \quad (8.3)$$

$$\mathbf{U}(z) = -\frac{\mathbf{J}}{\det \mathbf{J}} \cdot \left\{ F_0 \left(\frac{z^3}{6} - \frac{Lz^2}{2} \right) \mathbf{e}_F + \frac{M_0 z^2}{2} \mathbf{e}_z \times \mathbf{e}_M \right\} + z F_0 \mathbf{H} \cdot \mathbf{e}_F. \quad (8.4)$$

Table 1 illustrates the effect of shear to the end displacement of the cantilever thin-walled non-homogeneous beam with open profile.

8.4. Deflection curve of a fixed-fixed thin-walled beam with open cross section. Figure 9 shows the fixed-fixed supported thin-walled beam and its load. The applied load is acting on the whole length of the thin-walled beam. The intensity of the applied load is

$$\mathbf{s}(z) = \mathbf{f}_0 = f_0 \mathbf{e}_f, \quad (f_0, \mathbf{e}_f \text{ are constants}). \quad (8.5)$$

For a fixed-fixed end beam the boundary conditions are as follows

$$\mathbf{U}(0) = \mathbf{0}, \quad \boldsymbol{\phi}(0) = \mathbf{0}, \quad \mathbf{U}(L) = \mathbf{0}, \quad \boldsymbol{\phi}(L) = \mathbf{0}. \quad (8.6)$$

Application of equations (7.24), (7.27) and the first two of the boundary conditions mentioned above gives

$$\boldsymbol{\phi}(z) = \frac{\mathbf{J}}{\det \mathbf{J}} \cdot \left\{ -\frac{f_0 z^3}{6} \mathbf{e}_f + \frac{\mathbf{c}_1}{2} z^2 + \mathbf{c}_2 z \right\}, \quad (8.7)$$

Table 1. End deflection of the cantilever beam caused by a single force ($M_0 = 0$, $\mathbf{e}_F = \cos \alpha \mathbf{e}_x + \sin \alpha \mathbf{e}_y$, $L = 2$ m)

α	$\mathbf{U}(L)/F_0$ [$\frac{\text{m}}{\text{N}}$]	$\mathbf{U}_B(L)/F_0$ [$\frac{\text{m}}{\text{N}}$]	$\mathbf{U}_S(L)/F_0$ [$\frac{\text{m}}{\text{N}}$]
0	$\begin{pmatrix} 2.47073\text{E-}05 \\ 1.0477\text{E-}05 \end{pmatrix}$	$\begin{pmatrix} 2.44088\text{E-}05 \\ 1.04606\text{E-}05 \end{pmatrix}$	$\begin{pmatrix} 2.98525\text{E-}07 \\ 1.6429\text{E-}08 \end{pmatrix}$
$\frac{\pi}{6}$	$\begin{pmatrix} 2.66356\text{E-}05 \\ 1.66851\text{E-}05 \end{pmatrix}$	$\begin{pmatrix} 2.63689\text{E-}05 \\ 1.66151\text{E-}05 \end{pmatrix}$	$\begin{pmatrix} 2.66745\text{E-}07 \\ 7.00265\text{E-}08 \end{pmatrix}$
$\frac{\pi}{3}$	$\begin{pmatrix} 2.1427\text{E-}05 \\ 1.84224\text{E-}05 \end{pmatrix}$	$\begin{pmatrix} 2.12635\text{E-}05 \\ 1.83176\text{E-}05 \end{pmatrix}$	$\begin{pmatrix} 1.6349\text{E-}07 \\ 1.04861\text{E-}07 \end{pmatrix}$
$\frac{\pi}{2}$	$\begin{pmatrix} 1.0477\text{E-}05 \\ 1.52235\text{E-}05 \end{pmatrix}$	$\begin{pmatrix} 1.04606\text{E-}05 \\ 1.51119\text{E-}05 \end{pmatrix}$	$\begin{pmatrix} 1.6429\text{E-}08 \\ 1.11597\text{E-}07 \end{pmatrix}$
$\frac{5\pi}{6}$	$\begin{pmatrix} -1.61586\text{E-}05 \\ -1.4616\text{E-}06 \end{pmatrix}$	$\begin{pmatrix} -1.59083\text{E-}05 \\ -1.50318\text{E-}06 \end{pmatrix}$	$\begin{pmatrix} -2.50316\text{E-}07 \\ 4.15707\text{E-}08 \end{pmatrix}$
$\frac{2\pi}{3}$	$\begin{pmatrix} -3.28028\text{E-}06 \\ 7.94544\text{E-}06 \end{pmatrix}$	$\begin{pmatrix} -3.14525\text{E-}06 \\ 7.85701\text{E-}06 \end{pmatrix}$	$\begin{pmatrix} -1.35035\text{E-}07 \\ 8.84316\text{E-}08 \end{pmatrix}$

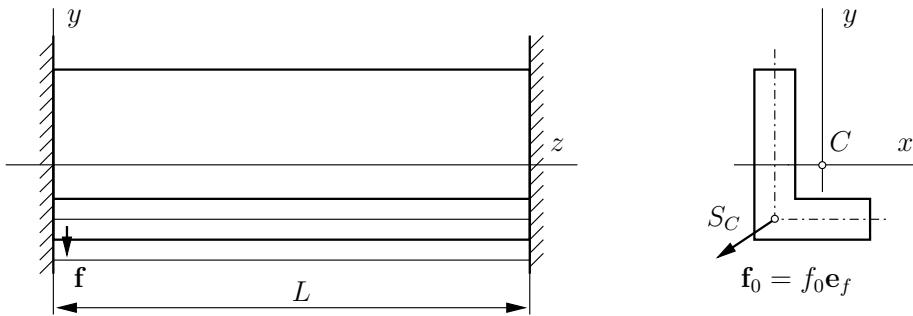


Figure 9. Uniform load on a fixed-fixed supported thin-walled beam with open profile

$$\mathbf{U}(z) = \frac{\mathbf{J}}{\det \mathbf{J}} \cdot \left\{ \frac{f_0 z^4}{24} \mathbf{e}_f - \frac{\mathbf{c}_1}{6} z^3 - \frac{\mathbf{c}_2}{2} z^2 \right\} + \mathbf{H} \cdot \left\{ -\frac{f_0 z^2}{2} \mathbf{e}_f + \mathbf{c}_1 z \right\}. \quad (8.8)$$

In the present problem $\mathbf{c}_3 = \mathbf{c}_4 = \mathbf{0}$. From the boundary conditions $\mathbf{U}(L) = \phi(L) = \mathbf{0}$ it can be deduced

$$\mathbf{c}_1 = \frac{f_0 L}{2} \mathbf{e}_f, \quad \mathbf{c}_2 = -\frac{f_0 L^2}{12} \mathbf{e}_f. \quad (8.9)$$

In Table 2 the deflection vector $\mathbf{U}(L/2)$ is listed for different values of α ($\mathbf{e}_f = \cos \alpha \mathbf{e}_x + \sin \alpha \mathbf{e}_y$).

Table 2. Deflection vector of the midpoint of a fixed-fixed thin-walled non-homogeneous beam with open profile

α	$\mathbf{U}(L/2)/f_0 \left[\frac{\text{m}^2}{\text{N}} \right]$	$\mathbf{U}_B(L/2)/f_0 \left[\frac{\text{m}^2}{\text{N}} \right]$	$\mathbf{U}_S(L/2)/f_0 \left[\frac{\text{m}^2}{\text{N}} \right]$
0	$\begin{pmatrix} -5.64617\text{E-}06 \\ -2.44759\text{E-}06 \end{pmatrix}$	$\begin{pmatrix} -5.7208\text{E-}06 \\ -2.4517\text{E-}06 \end{pmatrix}$	$\begin{pmatrix} 7.46312\text{E-}08 \\ 4.10724\text{E-}09 \end{pmatrix}$
$\frac{\pi}{6}$	$\begin{pmatrix} -6.11352\text{E-}06 \\ -3.87665\text{E-}06 \end{pmatrix}$	$\begin{pmatrix} -6.18021\text{E-}06 \\ -3.89416\text{E-}06 \end{pmatrix}$	$\begin{pmatrix} 6.66862\text{E-}08 \\ 1.75066\text{E-}08 \end{pmatrix}$
$\frac{\pi}{3}$	$\begin{pmatrix} -4.94276\text{E-}06 \\ -4.26697\text{E-}06 \end{pmatrix}$	$\begin{pmatrix} -4.98363\text{E-}06 \\ -4.29318\text{E-}06 \end{pmatrix}$	$\begin{pmatrix} 4.08726\text{E-}08 \\ 2.62151\text{E-}08 \end{pmatrix}$
$\frac{\pi}{2}$	$\begin{pmatrix} -2.44759\text{E-}06 \\ -3.51395\text{E-}06 \end{pmatrix}$	$\begin{pmatrix} -2.4517\text{E-}06 \\ -3.54185\text{E-}06 \end{pmatrix}$	$\begin{pmatrix} 4.10724\text{E-}09 \\ 2.78993\text{E-}08 \end{pmatrix}$
$\frac{5\pi}{6}$	$\begin{pmatrix} 3.66593\text{E-}06 \\ 3.62699\text{E-}07 \end{pmatrix}$	$\begin{pmatrix} 3.72851\text{E-}06 \\ 3.52307\text{E-}07 \end{pmatrix}$	$\begin{pmatrix} -6.25789\text{E-}08 \\ 1.03927\text{E-}08 \end{pmatrix}$
$\frac{2\pi}{3}$	$\begin{pmatrix} 7.03408\text{E-}07 \\ -1.81938\text{E-}06 \end{pmatrix}$	$\begin{pmatrix} 7.37167\text{E-}07 \\ -1.84149\text{E-}06 \end{pmatrix}$	$\begin{pmatrix} -3.37586\text{E-}08 \\ 2.21079\text{E-}08 \end{pmatrix}$

9. CONCLUSIONS

It has been shown that the governing formulas of bending and shear can be written in a coordinate-free invariant form for arbitrary non-homogeneous cross sections. New coordinate-free expressions are derived for the location of the centre of shear of thin-walled beams with open and closed profiles. Explicit coordinate-free formulas of shear rigidity tensors have been presented for thin-walled cross sections with open and closed profiles. Numerical examples illustrate that the principal directions of bending and shear deformations may not be the same. A vector–tensor formulation of the first-order shear deformation theory for non-homogeneous thin-walled beams is also presented.

Acknowledgements. This research was (partially) carried out in the framework of the Center of Excellence of Innovative Engineering Design and Technologies at the University of Miskolc.

REFERENCES

1. WANG, C.-C.: Some vector formulas for the bending and shearing of prismatic beams with arbitrary cross section. *Thin-Walled Structures*, **21**, (1995), 175–190.
2. STOKES, V. K.: A note on the pure bending of unsymmetrical prismatic beams. *ASME Journ. of Appl. Mech.*, **44**, (1977), 344–345.
3. STOKES, V. K.: Design with non-homogeneous materials – part i: Pure bending of prismatic bars. *Trans. ASME Journ. of Vibration, Stress & Reliability in Design*, **44**, (1987), 82–86.
4. STOKES, V. K.: Thermoelastic pure bending of non-homogeneous prismatic bars. *Journal of Thermal Stresses*, **14**, (1991), 499–518.

-
5. ROMANO, G., ROSATI, L., and FERRO, G.: Shear deformability of thin-walled beams of arbitrary cross sections. *International Journal for Numerical Methods in Engineering*, **35**, (1992), 283–306.
 6. LURJE, I.: *Theory of Elasticity*. Fiz-Mat. Lit, Moscow, 1970. In Russian.
 7. MALVERN, L. E.: *Introduction to the Mechanics of a Continuous Medium*. Prentice Hall, New York, 1969.
 8. MASE, G. T. and MASE, G. E.: *Continuum Mechanics*. CRC Press, London, 1999.
 9. BEER, F. P. and JOHNSTON, E. R.: *Mechanics of Materials*. McGraw-Hill, New York, 1987.
 10. VLASOV, V. Z.: *Thin-Walled Elastic Beams*. Israel Program for Scientific Translations. Jerusalem, Israel, 2nd edn., 1961.
 11. FUNG, Y. C.: *Introduction to the Theory of Aeroelasticity*. John Wiley, New York, 1955.
 12. WANG, C. M., REDDY, J. N., and LEE, K. H.: *Shear Deformable Beams and Plates. Relationships with Classical Solutions*. Elsevier, New York, 2000.

IN-PLANE BUCKLING OF ROTATIONALLY RESTRAINED HETEROGENEOUS SHALLOW ARCHES SUBJECTED TO A CONCENTRATED FORCE AT THE CROWN POINT

LÁSZLÓ KISS

Institute of Applied Mechanics, University of Miskolc
H-3515 Miskolc-Egyetemváros
mechkiss@uni-miskolc.hu

[Received: March 26, 2014]

Abstract. The nonlinear in-plane stability of shallow arches with cross-sectional inhomogeneity is investigated. It is assumed that a central concentrated load is exerted at the crown of the arch and the supports are uniform rotationally restrained pins at the endpoints with constant stiffness. The effects of the springs on the stability is investigated. It is found that such arches may buckle in an antisymmetric bifurcation mode with no strain increment at the moment of the stability loss, and in a symmetric snap-through mode with an increased strain. The effects of the springs are notable on the buckling ranges and also on the critical (buckling) loads. If the spring stiffness is zero we get back the results valid for pinned-pinned arches and as the stiffness of the rotational restraints tends to infinity the results become consistent with those for fixed-fixed arches. The results computed are compared with finite element calculations.

Mathematical Subject Classification: 74G60, 74B15

Keywords: Heterogeneous arch, stability, snap-through, bifurcation, rotational restraint

1. INTRODUCTION

Arches are widely used in many engineering applications. Let us mention, for instance, their role in arch bridges and roof structures. It is naturally important to be aware of the behavior of such structural members. An early scientific work on the mechanical behavior of such arches was published in the 19th century by Bresse [1], who derived the connection between the displacements and the inner forces. Regarding the stability, Hurlbrink [2] was the first to work out a model for the determination of the buckling load assuming the inextensibility of the centerline. The model of Chwalla and Kollbrunner [3] accounts for the extensibility of the centerline. Results by Timoshenko and Gere [4] are also of importance. Since the 1960s, work on stability issues became more intensive. Schreyer and Masur provided an analytical solution to arches with rectangular cross-section in [5]. DaDeppo [6] showed first in 1969 that quadratic terms in the stability analysis should be taken into account. Dym in [7] and [8] derives results for shallow arches under dead pressure. The thesis by Szeidl [9] determines the Green's function matrices of the extensible pinned-pinned and fixed-fixed circular

beams and determines not only the natural frequencies but also the critical loads given that the beam is subjected to a radial dead load. Finite element solutions are provided by e.g., Noor [10], Calboun [11], Elias [12] and Wen [13] with the assumption that the membrane strain is a quadratic function of the rotation field. A more accurate model is established by Pi [14]. Analytical solutions for pinned-pinned and fixed-fixed shallow circular arches under a central load are provided by Bradford et al. in [15], [16].

In the open literature there can hardly be found account for elastic supports when investigating the buckling behavior of arches. However, as structural members are often connected to each other, they can provide elastic rotational restraints. This can, in one way, be modeled by applying pinned supports with torsional springs, which impede the end rotations of the arch. Such a hypothesis is used by Bradford et al. in [17] for symmetric supports and a central load and in [18], where the spring stiffnesses are different at the ends. The authors have come to the conclusion that the springs have a significant effect on the in-plane elastic buckling behavior of shallow arches. Stiffening elastic supports for sinusoidal shallow arches are modeled in [19] by Plaut.

Within the frames of the present article a new geometrically nonlinear model is introduced for the in-plane elastic buckling of shallow circular arches with cross-sectional inhomogeneity. Nonlinearities are taken into account through the rotation field. The loading is a concentrated force, normal in direction and exerted at the crown point. The principle of virtual work is used to get the equilibrium equations. Uniform, rotationally restrained pinned supports are considered at the ends by using torsional springs with constant stiffness. The effects of the elastic restraints on the buckling types and buckling loads are studied. Special cases when the spring stiffness is zero and when it tends to infinity coincide with the earlier results in [20], [21] valid for pinned-pinned and for fixed-fixed supports. The solution algorithm is based on the one presented in [17]. However, the current model uses less neglects and is also valid for nonhomogeneous materials. In addition, more accurate predictions for not strictly shallow arches are also a benefit.

The paper is organized in seven Sections. Section 2 presents the fundamental hypotheses and relations for the pre- and post-buckling states. The differential equations, which govern the problem are derived in Section 3. Solutions to these are provided in Sections 4 and 5. Numerical evaluation of the results is presented in Section 6. The article concludes with a short summary, which is followed by the Appendix and the list of references.

2. FUNDAMENTAL RELATIONS

2.1. Pre-buckling state. Figure 1 shows the rotationally restrained arch and the applied curvilinear coordinate system, which is attached to the E -weighted centerline (or centerline for short). The former has a constant initial radius ρ_o . The right-handed local base is formed by the unit vectors \mathbf{e}_ξ (tangent to the centerline), \mathbf{e}_η

(perpendicular to the plane of the centerline) and \mathbf{e}_ζ (normal to the centerline) – $\mathbf{e}_\eta = \mathbf{e}_\zeta \times \mathbf{e}_\xi$.

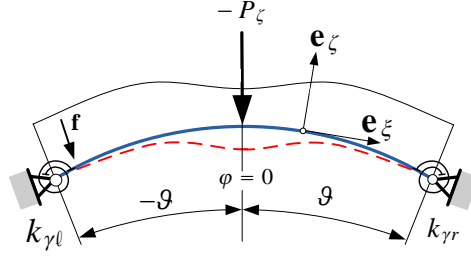


Figure 1. Rotationally restrained arch.

Under cross-sectional heterogeneity is meant that the material parameters – the Young's modulus E and the Poisson's number ν – are functions of the cross-sectional coordinates η and ζ (that is, these are independent of ξ): $E(\eta, \zeta) = E(-\eta, \zeta)$, $\nu(\eta, \zeta) = \nu(-\eta, \zeta)$. Otherwise, the material of the arch is isotropic. The cross-section is uniform and symmetric with respect to the coordinate plane (ξ, ζ) . The E -weighted centerline, along which the coordinates $\xi = s$ are measured, is assumed to remain in the coordinate plane (ξ, ζ) . The position of the point at which the E -weighted centerline intersects the cross-section is obtained from the condition

$$Q_{e\eta} = \int_A E(\eta, \zeta) \zeta \, dA = 0, \quad (1)$$

in which the integral is the E -weighted first moment with respect to the axis η – this quantity is denoted by $Q_{e\eta}$. We assume that the displacement vector at an arbitrary point of the cross-section prior to buckling has the form

$$\mathbf{u} = \mathbf{u}_o + \psi_{o\eta} \zeta \mathbf{e}_\xi = w_o \mathbf{e}_\zeta + (u_o + \psi_{o\eta} \zeta) \mathbf{e}_\xi, \quad (2)$$

where \mathbf{u}_o is the displacement vector of the centerline and $\psi_{o\eta}$ is the rigid body rotation there – Euler-Bernoulli beam theory is considered. The rotation can be determined in terms of the displacements as

$$\psi_{o\eta} = -\frac{1}{2} (\mathbf{u} \times \nabla)|_{\zeta=0} \cdot \mathbf{e}_\eta = \frac{u_o}{\rho_o} - \frac{dw_o}{ds}, \quad \nabla = \frac{\rho_o}{\rho_o + \zeta} \frac{\partial}{\partial s} \mathbf{e}_\xi + \frac{\partial}{\partial \eta} \mathbf{e}_\eta + \frac{\partial}{\partial \zeta} \mathbf{e}_\zeta. \quad (3)$$

Nonlinearities are taken into account by keeping some nonlinear terms in the Green-Lagrange strain tensor, that is

$$\mathbf{E} = \mathbf{E}^L + \mathbf{E}^N, \quad \mathbf{E}^L = \frac{1}{2} (\mathbf{u} \circ \nabla + \nabla \circ \mathbf{u}), \quad \mathbf{E}^N = \frac{1}{2} (\nabla \circ \mathbf{u}) \cdot (\mathbf{u} \circ \nabla) \simeq \frac{1}{2} \boldsymbol{\Psi} \cdot \boldsymbol{\Psi}^T. \quad (4)$$

Here $\boldsymbol{\Psi}$ is the tensor of small rotations and, for shallow arches, it is dominant compared to the other quadratic components [15]. Consequently

$$\varepsilon_\xi = \mathbf{e}_\xi \cdot \frac{1}{2} (\mathbf{u} \circ \nabla + \nabla \circ \mathbf{u}) \cdot \mathbf{e}_\xi + \mathbf{e}_\xi \cdot \frac{1}{2} (\boldsymbol{\Psi}^T \cdot \boldsymbol{\Psi}) \cdot \mathbf{e}_\xi = \frac{\rho_o}{\rho_o + \zeta} (\varepsilon_{o\xi} + \zeta \kappa_o) + \frac{1}{2} \psi_{o\eta}^2 \quad (5)$$

is the axial strain at an arbitrary point, where

$$\varepsilon_{o\xi} = \frac{du_o}{ds} + \frac{w_o}{\rho_o}, \quad \kappa_o = \frac{d\psi_{o\eta}}{ds} = \frac{1}{\rho_o} \frac{du_o}{ds} - \frac{d^2w_o}{ds^2} \quad \text{and} \quad \varepsilon_m = \varepsilon_{o\xi} + \frac{1}{2}\psi_{o\eta}^2. \quad (6)$$

Here $\varepsilon_{o\xi}$ and ε_m are the linear and the nonlinear axial strain on the centerline, further κ_o is the curvature there.

It is assumed that σ_ξ is much greater than any other element of the second Piola-Kirchhoff stress tensor. Under this condition $\sigma_\xi = E\varepsilon_\xi$ is the constitutive equation. The E -weighted reduced area A_{eR} , the E -weighted reduced moment of inertia I_{eR} and the E -weighted reduced first moment Q_{eR} are defined as

$$A_{eR} = \int_A \frac{\rho_o}{\rho_o + \zeta} E(\eta, \zeta) dA \simeq \int_A E(\eta, \zeta) dA = A_e, \quad (7a)$$

$$I_{eR} = \int_A \frac{\rho_o}{\rho_o + \zeta} E(\eta, \zeta) \zeta^2 dA \simeq \int_A \zeta^2 E(\eta, \zeta) dA = I_{e\eta}, \quad (7b)$$

$$Q_{eR} = \int_A \frac{\rho_o}{\rho_o + \zeta} E(\eta, \zeta) \zeta dA \simeq \frac{1}{\rho_o} \int_A \zeta^2 E(\eta, \zeta) dA = -\frac{I_{e\eta}}{\rho_o}. \quad (7c)$$

With the aid of these quantities and by recalling the kinematic relations (5)-(6), we get the axial force and the bending moment:

$$N = \int_A E\varepsilon_\xi dA = A_{eR}\varepsilon_{o\xi} + Q_{eR}\kappa_o + A_e \frac{1}{2}\psi_{o\eta}^2 \approx A_e\varepsilon_m - \frac{I_{e\eta}}{\rho_o}\kappa_o, \quad (8)$$

$$\begin{aligned} M &= \int_A E\varepsilon_\xi \zeta dA = \underbrace{\int_A E \frac{\zeta}{1 + \frac{\zeta}{\rho_o}} dA \varepsilon_{o\xi}}_{Q_{eR} \simeq -\frac{I_{e\eta}}{\rho_o}} + \underbrace{\int_A E \frac{\zeta^2}{1 + \frac{\zeta}{\rho_o}} dA \kappa_o}_{I_{eR} \simeq I_{e\eta}} + \underbrace{\int_A E \zeta dA}_{Q_{e\eta}=0} \frac{1}{2}\psi_{o\eta}^2 = \\ &= -I_{e\eta} \left(\frac{d^2w_o}{ds^2} + \frac{w_o}{\rho_o^2} \right). \quad (9) \end{aligned}$$

With the knowledge of the bending moment we can check – by utilizing (8) and (6)_{2,3} – that

$$N = \frac{I_{e\eta}}{\rho_o^2} \left(\frac{A_e \rho_o^2}{I_{e\eta}} - 1 \right) \varepsilon_m - \frac{M}{\rho_o} \approx A_e \varepsilon_m - \frac{M}{\rho_o}. \quad (10)$$

2.2. Post-buckling state. Quantities denoted by an asterisk belong to the post-buckling equilibrium state, while the change (increment) between the pre- and post-buckling equilibrium is denoted by a subscript b . (The change from the initial configuration to the pre-buckling state is not denoted specifically.) Making use of this convention, similarly as before, we can derive the rotation field and the change of curvature as

$$\psi_{o\eta}^* = \psi_{o\eta} + \psi_{o\eta b}, \quad \psi_{o\eta b} = \frac{u_{ob}}{\rho_o} - \frac{dw_{ob}}{ds}, \quad \kappa_o^* = \kappa_o + \kappa_{ob}, \quad \kappa_{ob} = \frac{1}{\rho_o} \frac{du_{ob}}{ds} - \frac{d^2w_{ob}}{ds^2}. \quad (11)$$

As regards the strain increment (assuming $\left| \frac{1}{2} \psi_{o\eta}^2 \right| \ll |\psi_{o\eta} \psi_{ob}|$, which is generally accepted in the literature) we have

$$\varepsilon_{\xi}^* = \frac{\rho_o}{\rho_o + \zeta} (\varepsilon_{o\xi}^* + \zeta \kappa_o^*) + \frac{1}{2} (\psi_{o\eta}^*)^2 = \varepsilon_{\xi} + \varepsilon_{\xi b}, \quad \varepsilon_{\xi b} \simeq \frac{\rho_o}{\rho_o + \zeta} (\varepsilon_{o\xi b} + \zeta \kappa_{ob}) + \psi_{o\eta b} \psi_{o\eta}; \quad (12a)$$

$$\varepsilon_{o\xi b} = \frac{du_{ob}}{ds} + \frac{w_{ob}}{\rho_o}, \quad \varepsilon_{mb} \simeq \varepsilon_{o\xi b} + \psi_{o\eta b} \psi_{o\eta}. \quad (12b)$$

Recalling (7), (8), (10) and (12) we can write

$$N^* = \int_A E \varepsilon_{\xi}^* dA = N + N_b, \quad N_b = A_e \varepsilon_{mb} - \frac{I_{e\eta}}{\rho_o} \kappa_{ob}. \quad (13)$$

In the same way we obtain the increment in the bending moment as

$$M^* = \int_A E \varepsilon_{\xi}^* \zeta dA = M + M_b, \quad M_b = -I_{e\eta} \left(\frac{d^2 w_{ob}}{ds^2} + \frac{w_{ob}}{\rho_o^2} \right). \quad (14)$$

Let us assume that

$$A_e \rho_o^2 / I_{e\eta} - 1 \approx A_e \rho_o^2 / I_{e\eta} = (\rho_o / i_e)^2 = m, \quad i_e = \sqrt{I_{e\eta} / A_e}. \quad (15)$$

Here i_e is the E -weighted radius of gyration and m is the slenderness ratio of the arch. The latter (heterogeneity) parameter is of particular importance as the computational results will significantly depend on it.

With the knowledge of the increment in the bending moment we can check, in the same way as we did for equation (10), that

$$N_b = \frac{I_{e\eta}}{\rho_o^2} \left(\frac{A_e \rho_o^2}{I_{e\eta}} - 1 \right) \varepsilon_{mb} - \frac{M_b}{\rho_o} \approx A_e \varepsilon_{mb} - \frac{M_b}{\rho_o}. \quad (16)$$

It should be pointed out that Bradford et al. have assumed $\rho_o / (\rho_o + \zeta) = 1$ when expressing the axial strain and the strain increment at an arbitrary point. They have also neglected the terms M / ρ_o and M_b / ρ_o in their corresponding article when expressing the axial force and its increment – compare (10) and (16) with (15) and (47) in [17]

We shall change derivatives with respect to s to derivatives with respect to φ by using the following equation:

$$\frac{d^n(\dots)}{ds^n} = \frac{1}{\rho_o^n} \frac{d^n(\dots)}{d\varphi^n} = (\dots)^{(n)}, \quad n \in \mathbb{Z}. \quad (17)$$

This transformation is carried out, where necessary without a remark.

3. GOVERNING EQUATIONS

3.1. Equations of the pre-buckling equilibrium. Assuming symmetric loading and support conditions Figure 1 shows the centerline in the initial configuration (continuous line) and in the pre-buckling equilibrium (dashed line). We shall assume in a more general approach that the arch with a central angle of 2ϑ is subjected to the concentrated force P_{ζ} at the crown as well as to the arbitrary distributed line load

$\mathbf{f} = f_t \mathbf{e}_\xi + f_n \mathbf{e}_\zeta$. Moreover, the [left] (right) end of the arch is rotationally restrained by torsional springs with spring stiffness $[k_{\gamma\ell}]$ ($k_{\gamma r}$). The principle of virtual work is given by

$$\int_V \sigma_\xi \delta \varepsilon_\xi dV = -P_\zeta \delta w_o|_{s=0} - k_{\gamma\ell} \psi_{o\eta} \delta \psi_{o\eta}|_{s(-\vartheta)} - k_{\gamma r} \psi_{o\eta} \delta \psi_{o\eta}|_{s(\vartheta)} + \int_{\mathcal{L}} (f_n \delta w_o + f_t \delta u_o) ds, \quad (18)$$

where the virtual quantities are preceded by the symbol δ . After substituting the kinematic equations (5) and (6) in terms of the virtual quantities and applying then formulae (8) and (9) established for the inner forces, the integration by parts theorem leads to a form of the principle of virtual work from which, with regard to the arbitrariness of the virtual quantities, we get the equilibrium equations

$$\begin{aligned} \frac{dN}{ds} + \frac{1}{\rho_o} \left[\frac{dM}{ds} - \left(N + \frac{M}{\rho_o} \right) \psi_{o\eta} \right] + f_t &= 0, \\ \frac{d}{ds} \left[\frac{dM}{ds} - \left(N + \frac{M}{\rho_o} \right) \psi_{o\eta} \right] - \frac{N}{\rho_o} + f_n &= 0. \end{aligned} \quad (19)$$

It also follows from the principle of virtual work that boundary conditions can be imposed on

$$N|_{s(\pm\vartheta)} \quad \text{or} \quad u_o|_{s(\pm\vartheta)}, \quad (20a)$$

$$\left[\frac{dM}{ds} - \left(N + \frac{M}{\rho_o} \right) \psi_{o\eta} \right] \Big|_{s(\pm\vartheta)} \quad \text{or} \quad w_o|_{s(\pm\vartheta)}, \quad (20b)$$

$$(M \pm k_\gamma \psi_{o\eta})|_{s(\pm\vartheta)} \quad \text{or} \quad \psi_{o\eta}|_{s(\pm\vartheta)}, \quad (20c)$$

where it is assumed that $k_{\gamma\ell} = k_{\gamma r} = k_\gamma$. In addition, the discontinuity condition

$$\left[\frac{dM}{ds} - \left(N + \frac{M}{\rho_o} \right) \psi_{o\eta} \right] \Big|_{s=+0} - \left[\frac{dM}{ds} - \left(N + \frac{M}{\rho_o} \right) \psi_{o\eta} \right] \Big|_{s=-0} - P_\zeta = 0 \quad (21)$$

for the shear force at the crown point should also be fulfilled.

In the sequel we assume $f_t = f_n = 0$. Upon substitution of equation (6) into equation (19)₁ we get

$$\frac{d}{ds} (A_e \varepsilon_m) - \frac{1}{\rho_o} (A_e \varepsilon_m \psi_{o\eta}) = 0. \quad (22)$$

Let us now neglect the quadratic term $\varepsilon_m \psi_{o\eta}$. Consequently, we arrive at

$$\frac{d\varepsilon_m}{ds} \simeq \frac{d\varepsilon_{o\xi}}{ds} = 0 \quad \rightarrow \quad \varepsilon_m \simeq \varepsilon_{o\xi} = \text{constant}, \quad (23)$$

which shows, depending on which theory is applied, that the nonlinear/linear strain on the centerline is constant.

If we introduce (3) and (6)_{1,3} into the expression $\rho_o \varepsilon_m \left(1 + \psi_{o\eta}^{(1)} \right)$ we arrive at the following result (the quadratic term is neglected when that is compared to the others):

$$\begin{aligned} \rho_o \varepsilon_m \left(1 + \psi_{o\eta}^{(1)} \right) &= \rho_o \varepsilon_m \left[1 + \frac{1}{\rho_o} \left(u_o^{(1)} - w_o^{(2)} \right) \right] = \\ &= \rho_o \varepsilon_m \left[1 + \frac{1}{\rho_o} \left(\rho_o \varepsilon_m - w_o - \frac{1}{2} \psi_{o\eta}^2 \rho_o - w_o^{(2)} \right) \right] \approx \\ &\approx \rho_o \varepsilon_m \underbrace{\left(1 + \varepsilon_m \right)}_{\approx 1} - \varepsilon_m \left(w_o + w_o^{(2)} \right) \approx \rho_o \varepsilon_m - \varepsilon_m \left(w_o^{(2)} + w_o \right) . \end{aligned} \quad (24)$$

Substitute now formulae (9) and (10) into (19)₂ and take equations (23) and (24) into account. After some manipulations we have

$$W_o^{(4)} + (\chi^2 + 1) W_o^{(2)} + \chi^2 W_o = \chi^2 - 1, \quad \chi^2 = 1 - m \varepsilon_m . \quad (25)$$

Here and in the sequel $W_o = w_o/\rho_o$ and $U_o = u_o/\rho_o$ are dimensionless displacements. Equation (25) can be compared with the equation Bradford et al. have used in their series of articles published recently on stability problems of shallow arches. This equation is of the form

$$W_o^{(4)} + (\chi^2 - 1) W_o^{(2)} = \chi^2 - 1. \quad (26)$$

Equation (25) includes less neglects than that derived by Bradford et al. – see, e.g., [15], [17].

3.2. Equations of the post-buckling equilibrium. The principle of virtual work for the buckled equilibrium configuration assumes the form

$$\begin{aligned} \int_V \sigma_\xi^* \delta \varepsilon_\xi^* dV &= -P_\zeta^* \delta w_o^*|_{s=0} - k_{\gamma\ell} \psi_{o\eta}^* \delta \psi_{o\eta}^*|_{s(-\vartheta)} - k_{\gamma r} \psi_{o\eta}^* \delta \psi_{o\eta}^*|_{s(\vartheta)} + \\ &+ \int_{\mathcal{L}} (f_n^* \delta w_o^* + f_t^* \delta u_o^*) ds . \end{aligned} \quad (27)$$

By repeating the line of thought leading to (19),(20) and taking into account that (a) the principle of virtual work should be fulfilled in the pre-buckling state; (b) $P_{\zeta b} = 0$ and $k_{\gamma\ell} = k_{\gamma r} = k_\gamma$ the principle of virtual work yields

$$\frac{dN_b}{ds} + \frac{1}{\rho_o} \frac{dM_b}{ds} - \frac{1}{\rho_o} \left(N + \frac{M}{\rho_o} \right) \psi_{o\eta b} - \frac{1}{\rho_o} \left(N_b + \frac{M_b}{\rho_o} \right) \psi_{o\eta b} + f_{tb} = 0 , \quad (28a)$$

$$\frac{d^2 M_b}{ds^2} - \frac{N_b}{\rho_o} - \frac{d}{ds} \left[\left(N + N_b + \frac{M + M_b}{\rho_o} \right) \psi_{o\eta b} + \left(N_b + \frac{M_b}{\rho_o} \right) \psi_{o\eta} \right] + f_{nb} = 0, \quad (28b)$$

which govern the post-buckling equilibrium. For the buckled configuration, boundary conditions can be prescribed on the following quantities:

$$N_b|_{s(\pm\vartheta)} \quad \text{or} \quad u_{ob}|_{s(\pm\vartheta)} , \quad (29a)$$

$$\left[\frac{dM_b}{ds} - \left(N + N_b + \frac{M + M_b}{\rho_o} \right) \psi_{o\eta b} - \left(N_b + \frac{M_b}{\rho_o} \right) \psi_{o\eta} \right]_{s(\pm\vartheta)} \quad \text{or} \quad w_{ob}|_{s(\pm\vartheta)} , \quad (29b)$$

$$(M_b \pm k_\gamma \psi_{o\eta})|_{s(\pm\vartheta)} \quad \text{or} \quad \psi_{o\eta} b|_{s(\pm\vartheta)} . \tag{29c}$$

In the forthcoming it is assumed that $f_{tb} = f_{nb} = 0$. Observe that, apart from the last but one term, (28a) formally coincides with (19)₁. However, since the term mentioned is quadratic in the increment, it can be neglected with a good accuracy. Therefore repeating now a similar line of thought leading to (23), we obtain that the strain increment is constant:

$$\frac{d}{ds} (A_e \varepsilon_{mb}) - \underbrace{\frac{1}{\rho_o} (A_e \varepsilon_m \psi_{o\eta b})}_{\text{it can also be neglected}} = 0 \quad \Rightarrow \quad \varepsilon_{mb} \simeq \varepsilon_{o\zeta b} = \text{constant} . \tag{30}$$

If we (a) take into account that $\varepsilon_m^{(1)} = \varepsilon_{mb}^{(1)} = 0$; (b) substitute M_b from (14) and (c) utilize that

$$m\rho_o \varepsilon_{mb} \left(1 + \psi_{o\eta}^{(1)} \right) \simeq m\rho_o \varepsilon_{mb} \left[1 - \frac{1}{\rho_o} \left(w_o^{(2)} + w_o \right) \right] = m\rho_o \varepsilon_{mb} - m\varepsilon_{mb} \left(w_o^{(2)} + w_o \right)$$

(this relation can be set up in the same way as (24)) then, after some manipulations, (28b) results in

$$W_{ob}^{(4)} + (\chi^2 + 1)W_{ob}^{(2)} + \chi^2 W_{ob} = m\varepsilon_{mb} \left[1 - \left(W_o^{(2)} + W_o \right) \right] . \tag{31}$$

This equation is again comparable with the outcome derived by Bradford et al. – e.g., [15], [17] – that is

$$W_{ob}^{(4)} + (\chi^2 - 1)W_{ob}^{(2)} = m\varepsilon_{mb} \left[1 - W_o^{(2)} \right] . \tag{32}$$

4. SOLUTION FOR THE PRE-BUCKLING STATE

The general solution satisfying (25) for the dimensionless normal displacement is of the form

$$W_o(\varphi) = \frac{\chi^2 - 1}{\chi^2} + A_1 \cos \varphi + A_2 \sin \varphi - \frac{A_3}{\chi^2} \cos \chi\varphi - \frac{A_4}{\chi^2} \sin \chi\varphi, \tag{33}$$

in which A_i ($i = 1, \dots, 4$) are integration constants. Since all the geometry, the loa-

Table 1. Boundary conditions for the rotationally restrained arch.

Boundary conditions	
Crown point	Right end
$\psi_{o\eta} _{\varphi=+0} = 0 \rightarrow W_o^{(1)} _{\varphi=+0} = 0$	$W_o _{\varphi=\vartheta} = 0$
$\left[-\frac{dM}{ds} + \frac{P_\zeta}{2} \right]_{\varphi=+0} = 0 \rightarrow W_o^{(3)} _{\varphi=+0} = \frac{\mathcal{P}}{\vartheta}$	$[M + k_\gamma \psi_{o\eta}] _{\varphi=\vartheta} = 0 \rightarrow [W_o^{(2)} + \mathcal{S}W_o^{(1)}] _{\varphi=\vartheta} = 0$

ding and the supports are symmetric, it is sufficient to consider a half of the arch as the pre-buckling shape is also symmetric. To determine the integration constants, we shall use the boundary conditions (BCs) presented in Table 1 – $\mathcal{P} = -P_\zeta \rho_o^2 \vartheta / 2I_{e\eta}$ is the dimensionless load and $\mathcal{S} = \rho_o k_\gamma / I_{e\eta}$ is the dimensionless stiffness of the restraints.

For the sake of brevity let us introduce the constant

$$a = (\chi^2 - 1) \cos \vartheta \cos \chi \vartheta - \mathcal{S} (\sin \vartheta \cos \chi \vartheta - \chi \cos \vartheta \sin \chi \vartheta). \quad (34)$$

Solution (33) satisfies the boundary conditions if

$$A_1 = A_{11} + \frac{\mathcal{P}}{\vartheta} A_{12} = \frac{(1 - \chi^2) (\chi \cos \chi \vartheta + \mathcal{S} \sin \chi \vartheta)}{\chi a} + \frac{(1 - \chi^2) \sin \vartheta \cos \chi \vartheta - \mathcal{S} (\cos \vartheta \cos \chi \vartheta + \chi \sin \vartheta \sin \chi \vartheta - 1) \mathcal{P}}{(\chi^2 - 1) a \vartheta}, \quad (35a)$$

$$A_2 = \frac{1}{(\chi^2 - 1)} \frac{\mathcal{P}}{\vartheta} = A_{22} \frac{\mathcal{P}}{\vartheta}; \quad (35b)$$

$$A_3 = A_{31} + \frac{\mathcal{P}}{\vartheta} A_{32} = \frac{\cos \vartheta + \mathcal{S} \sin \vartheta}{-a} + \frac{\chi [(\chi^2 - 1) \cos \vartheta \sin \chi \vartheta - \mathcal{S} (\sin \vartheta \sin \chi \vartheta + \chi \cos \vartheta \cos \chi \vartheta - \chi)] \mathcal{P}}{-(\chi^2 - 1) a \vartheta}, \quad (35c)$$

$$A_4 = \frac{\chi}{(\chi^2 - 1)} \frac{\mathcal{P}}{\vartheta} = A_{42} \frac{\mathcal{P}}{\vartheta}. \quad (35d)$$

If $[\mathcal{S} = 0]$ ($\mathcal{S} \rightarrow \infty$) we get back the results valid for [pinned-pinned] (fixed-fixed) arches – see [20], [21]. The radial displacement for the whole arch is given by

$$W_o = \frac{\chi^2 - 1}{\chi^2} + A_{11} \cos \varphi - \frac{A_{31}}{\chi^2} \cos \chi \varphi + \left(A_{12} \cos \varphi + A_{22} H \sin \varphi - \frac{A_{32}}{\chi^2} \cos \chi \varphi - \frac{A_{42}}{\chi^2} H \sin \chi \varphi \right) \frac{\mathcal{P}}{\vartheta}; \quad (36)$$

in which $H = H(\varphi) = 1$ if $\varphi > 0$ and $H = H(\varphi) = -1$ if $\varphi < 0$. The rotation field (by neglecting the effects of the tangential displacement due to the shallowness) is

$$\psi_{o\eta} \simeq -W_o^{(1)} = B_{11} \sin \varphi + B_{31} \sin \chi \varphi + (B_{12} \sin \varphi + B_{22} H \cos \varphi + B_{32} \sin \chi \varphi + B_{42} H \cos \chi \varphi) \frac{\mathcal{P}}{\vartheta}; \quad (37)$$

where the new constants are

$$B_{11} = A_{11}, \quad B_{12} = A_{12}, \quad B_{22} = -A_{22}, \quad B_{31} = -\frac{A_{31}}{\chi}, \quad B_{32} = -\frac{A_{32}}{\chi}, \quad B_{42} = \frac{A_{42}}{\chi}.$$

Because the strain on the centerline is constant, based on (23), the mathematical average of the strain, i.e., the strain itself, is given by

$$\varepsilon_m = \frac{1}{\vartheta} \int_0^\vartheta \varepsilon_m d\varphi = \frac{1}{\vartheta} \int_0^\vartheta \left(\varepsilon_o \xi + \frac{1}{2} \psi_{o\eta}^2 \right) d\varphi = \frac{1}{\vartheta} \int_0^\vartheta \left(U_o^{(1)} + W_o + \frac{1}{2} \psi_{o\eta}^2 \right) d\varphi; \quad (38)$$

where

$$\frac{1}{\vartheta} \int_0^\vartheta U_o^{(1)} d\varphi = U_o|_0^\vartheta = 0. \quad (39)$$

Equation (38) results in the

$$I_2 \mathcal{P}^2 + I_1 \mathcal{P} + I_0 - \varepsilon_m = 0, \quad I_j(m, \vartheta, \chi, \mathcal{S}) \in \mathbb{R}, \quad j = 0, 1, 2 \quad (40)$$

quadratic formula for the dimensionless force, in which the coefficients I_j can be obtained in a closed form – see Appendix A.1 for details.

5. SOLUTIONS FOR THE POST-BUCKLING STATE

5.1. Differential equations, which govern the problem. Substitution of the solution (36) into the post-buckling equilibrium equation (31) yields

$$W_{ob}^{(4)} + (1 + \chi^2)W_{ob}^{(2)} + \chi^2 W_{ob} = -m\varepsilon_{mb} \frac{1 - \chi^2}{\chi^2} \left(\frac{1}{1 - \chi^2} + A_3 \cos \chi\varphi + A_4 \sin \chi\varphi \right). \quad (41)$$

In general, there are two possibilities regarding the buckled equilibrium of the arch [15]. When the strain increment ε_{mb} is constant but not equal to zero, the problem is governed by the above relation and the buckled shape is symmetric. However, it is also possible that the arch buckles antisymmetrically with no strain increment ($\varepsilon_{mb} = 0$). Then the phenomenon is described by the

$$W_{ob}^{(4)} + (1 + \chi^2)W_{ob}^{(2)} + \chi^2 W_{ob} = 0 \quad (42)$$

homogeneous differential equation. The mathematical average of the strain increment, that is, the strain increment itself can be determined by using the kinematical equations (3), (10) and (12b) under the assumption that the effect of the normal displacement is again negligible when calculating the rotation increment:

$$\begin{aligned} \varepsilon_{mb} &\simeq \frac{1}{2\vartheta} \int_{-\vartheta}^{\vartheta} (\varepsilon_{o\zeta b} + \psi_{o\eta b} \psi_{o\eta}) d\varphi = \frac{1}{2\vartheta} \int_{-\vartheta}^{\vartheta} [U_{ob}^{(1)} + W_{ob} + (U_{ob} - W_{ob}^{(1)}) (U_o - W_o^{(1)})] d\varphi \approx \\ &\approx \frac{1}{2\vartheta} \int_{-\vartheta}^{\vartheta} (W_{ob} + W_{ob}^{(1)} W_o^{(1)}) d\varphi. \end{aligned} \quad (43)$$

It will later be shown that antisymmetric shape belongs to bifurcation buckling, while in the case of a snap-through (or limit point) buckling the shape of the arch is always symmetric.

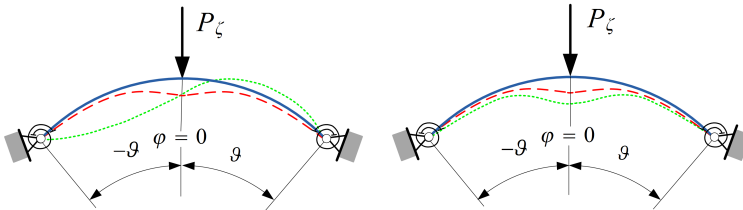


Figure 2. Antisymmetric and symmetric buckling shapes.

In Figure 2 the continuous lines show the centerline in the initial configuration, the dashed lines represent the pre-buckling equilibrium state and the dotted lines illustrate the buckled arch shapes for antisymmetric and symmetric buckling.

5.2. Antisymmetric buckling. The solution to the homogeneous equilibrium equation (42) is sought for the whole arch as

$$W_{ob}(\varphi) = C_1 \cos \varphi + C_2 \sin \varphi + C_3 \sin \chi \varphi + C_4 \cos \chi \varphi, \quad (44)$$

where C_i ($i = 1, \dots, 4$) are integration constants. It is paired with the homogeneous BCs gathered in Table 2.

Table 2. Boundary conditions in terms of W_{ob} .

Boundary conditions	
Left end	Right end
$W_{ob} _{\varphi=-\vartheta} = 0$	$W_{ob} _{\varphi=\vartheta} = 0$
$\left(-W_{ob}^{(2)} + \mathcal{S}W_{ob}^{(1)}\right) _{\varphi=-\vartheta} = 0$	$\left(W_{ob}^{(2)} + \mathcal{S}W_{ob}^{(1)}\right) _{\varphi=\vartheta} = 0$

Upon substitution of solution (44) into the boundary conditions, we arrive at a homogeneous equation system for which solution different from the trivial one exists if the determinant of the coefficient matrix vanishes:

$$\begin{aligned} \mathcal{D} = & [(\chi^2 - 1) \sin \vartheta \sin \chi \vartheta + \mathcal{S} (\cos \vartheta \sin \chi \vartheta - \chi \sin \vartheta \cos \chi \vartheta)] \times \\ & \times [(\chi^2 - 1) \cos \vartheta \cos \chi \vartheta + \mathcal{S} (\chi \cos \vartheta \sin \chi \vartheta - \sin \vartheta \cos \chi \vartheta)] = 0. \end{aligned} \quad (45)$$

Vanishing of the first factor in (45) results in the transcendental equation

$$\frac{\mathcal{S} \chi \tan \vartheta}{\mathcal{S} + (\chi^2 - 1) \tan \vartheta} = \tan \chi \vartheta. \quad (46)$$

Some numerical solutions for $\mathfrak{F} = \chi \vartheta$ in terms of the ϑ are plotted in Figure 3. When $[\mathcal{S} = 0](\mathcal{S} \rightarrow \infty)$ this characteristic equation coincides with that valid for [pinned-pinned](fixed-fixed) arches – see [20], [21].

Recalling (25)₂, we get the critical strain for antisymmetric buckling:

$$\varepsilon_{mcr\ anti} = \frac{1 - \chi^2}{m} = \frac{1}{m} \left[1 - \left(\frac{\mathfrak{F}(\vartheta, \mathcal{S})}{\vartheta} \right)^2 \right]. \quad (47)$$

If we now substitute the solution (46) back to the boundary conditions, it follows that $C_1 = C_4 = 0$ and $C_2 = -C_3 \sin \chi \vartheta / \sin \vartheta$. Consequently, recalling the general solution (44), we get that the shape of the arch is antisymmetric:

$$W_{ob}(\varphi) = C_3 \left(\sin \chi \varphi - \frac{\sin \chi \vartheta}{\sin \vartheta} \sin \varphi \right) = C_3 \left(\sin \frac{\mathfrak{F}}{\vartheta} \varphi - \frac{\sin \mathfrak{F}}{\sin \vartheta} \sin \varphi \right). \quad (48)$$

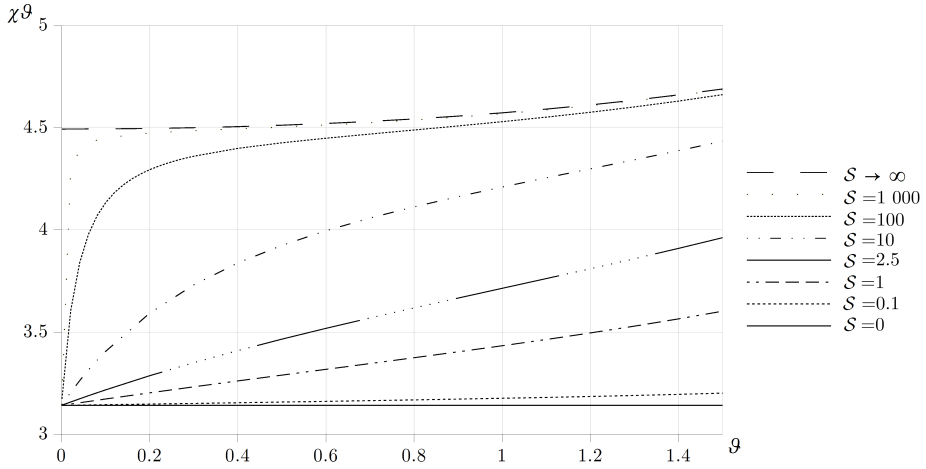


Figure 3. Some solutions to $\mathfrak{F}(\vartheta, \mathcal{S})$.

Vanishing of the second factor in (45) yields

$$(\chi^2 - 1) + \mathcal{S}(\chi \tan \chi\vartheta - \tan \vartheta) = 0. \tag{49}$$

After solving the above equation for $\mathfrak{G} = \chi\vartheta$, we find that a symmetric buckling shape is the solution for the radial displacement with $C_2 = C_3 = 0$ and $C_1 = C_4 \cos \chi\vartheta / \cos \vartheta$:

$$W_{ob}(\varphi) = C_4 \left(\cos \chi\varphi - \frac{\cos \chi\vartheta}{\cos \vartheta} \cos \varphi \right) = C_4 \left(\cos \frac{\mathfrak{G}}{\vartheta} \varphi - \frac{\cos \mathfrak{G}}{\cos \vartheta} \cos \varphi \right). \tag{50}$$

5.3. Symmetric snap-through buckling. The general solution to the inhomogeneous equation (41) is

$$W_{ob}(\varphi) = D_1 \cos \varphi + D_2 \sin \varphi + D_3 \sin \chi\varphi + D_4 \cos \chi\varphi - \frac{m\varepsilon_m b}{2\chi^3} \left(\frac{2}{\chi} + A_3 \varphi \sin \chi\varphi - A_4 \varphi \cos \chi\varphi \right). \tag{51}$$

Since now the buckled shape is symmetric, the BCs collected in Table 3 are valid for the right half-arch.

Table 3. Boundary conditions for symmetric buckling.

Boundary conditions	
Crown point	Right end
$W_{ob}^{(1)} \Big _{\varphi=0} = 0$	$W_{ob} \Big _{\varphi=\vartheta} = 0$
$W_{ob}^{(3)} \Big _{\varphi=0} = 0$	$W_{ob}^{(2)} + \mathcal{S}W_{ob}^{(1)} \Big _{\varphi=\vartheta} = 0$

Upon substitution of solution (51) into the boundary conditions, we get a system of linear equations from which

$$\begin{aligned}
 D_1 &= \varepsilon_{mb} \left(\hat{D}_{11} + \hat{D}_{12} \frac{\mathcal{P}}{\vartheta} \right) = \\
 &= \varepsilon_{mb} \frac{m}{\chi^3 a} \left\{ A_{31} [\chi \cos^2 \chi\vartheta + 0.5\mathcal{S}(\vartheta\chi + \cos \chi\vartheta \sin \chi\vartheta)] + (\chi \cos \chi\vartheta + \mathcal{S} \sin \chi\vartheta) \right\} + \\
 &\quad + \varepsilon_{mb} \frac{m}{2\chi^3 (1 - \chi^2) a} \left\{ A_{32} (1 - \chi^2) [2\chi \cos^2 \chi\vartheta + \mathcal{S}(\vartheta\chi + \cos \chi\vartheta \sin \chi\vartheta)] + \right. \\
 &\quad \quad \quad \left. + A_{42} [2\chi (1 - \chi^2) (\sin \chi\vartheta - \chi \sin \vartheta) \cos \chi\vartheta + \right. \\
 &\quad \quad \quad \left. + \mathcal{S} (2\chi^2 \cos \vartheta \cos \chi\vartheta + 2\chi^3 \sin \vartheta \sin \chi\vartheta - 3\chi^2 + 1 + (\chi^2 - 1) \cos^2 \chi\vartheta)] \right\} \frac{\mathcal{P}}{\vartheta}, \quad (52a)
 \end{aligned}$$

$$D_2 = \varepsilon_{mb} \hat{D}_{22} \frac{\mathcal{P}}{\vartheta} = \varepsilon_{mb} \frac{mA_{42}}{(\chi^2 - 1)\chi} \frac{\mathcal{P}}{\vartheta}, \quad D_3 = \varepsilon_{mb} \hat{D}_{32} \frac{\mathcal{P}}{\vartheta} = \varepsilon_{mb} \frac{A_{42}m(3\chi^2 - 1)}{2\chi^4(1 - \chi^2)} \frac{\mathcal{P}}{\vartheta}, \quad (52b)$$

$$\begin{aligned}
 D_4 &= \varepsilon_{mb} \left(\hat{D}_{41} + \hat{D}_{42} \frac{\mathcal{P}}{\vartheta} \right) = \\
 &= \varepsilon_{mb} \frac{m \cos \vartheta}{-2\chi^4 a} \left\{ 2(1 + \mathcal{S} \tan \vartheta) + A_{31}\chi [2\chi - \vartheta(\chi^2 - 1) \tan \chi\vartheta + \right. \\
 &\quad \quad \quad \left. + \mathcal{S}(\vartheta \tan \vartheta \tan \chi\vartheta + \tan \chi\vartheta + \chi\vartheta)] \cos \chi\vartheta \right\} + \\
 &\quad + \varepsilon_{mb} \frac{m}{2\chi^4 (\chi^2 - 1) a} \left\{ A_{32}\chi (1 - \chi^2) [(2\chi - \vartheta(\chi^2 - 1) \tan \chi\vartheta) + \right. \\
 &\quad \quad \quad \left. + \mathcal{S}(\vartheta \tan \vartheta \tan \chi\vartheta + \tan \chi\vartheta + \chi\vartheta)] \cos \vartheta \cos \chi\vartheta + \right. \\
 &\quad + A_{42} \left[(1 - \chi^2)^2 (\tan \chi\vartheta - \chi\vartheta) \cos \vartheta \cos \chi\vartheta + \mathcal{S} [2\chi^3 (1 - \cos \vartheta \cos \chi\vartheta) + \right. \\
 &\quad \quad \left. + (1 - \chi^2) \vartheta\chi (\chi \tan \chi\vartheta - \tan \vartheta) \cos \vartheta \cos \chi\vartheta + (1 - 3\chi^2) \sin \vartheta \sin \chi\vartheta] \right] \left. \right\} \frac{\mathcal{P}}{\vartheta} \quad (52c)
 \end{aligned}$$

are the integration constants D_i ($i = 1, \dots, 4$). We remark that the constants \hat{D}_{11} , \hat{D}_{12} , \hat{D}_{22} , \hat{D}_{32} , \hat{D}_{41} and \hat{D}_{42} can be read off equations (52).

For the sake of brevity, we manipulate the particular solution to (51) into the following form:

$$\begin{aligned}
 W_{ob \text{ part}} &= -\varepsilon_{mb} \frac{m}{2\chi^3} \left[\frac{2}{\chi} + \left(A_{31} + A_{32} \frac{\mathcal{P}}{\vartheta} \right) \varphi \sin \chi\varphi - A_{42} \varphi \cos \chi\varphi \frac{\mathcal{P}}{\vartheta} \right] = \\
 &= \varepsilon_{mb} \left[-\frac{m}{\chi^4} - \frac{A_{31}m}{2\chi^3} \varphi \sin \chi\varphi + \left(-\frac{A_{32}m}{2\chi^3} \varphi \sin \chi\varphi + \frac{A_{42}m}{2\chi^3} \varphi \cos \chi\varphi \right) \frac{\mathcal{P}}{\vartheta} \right] = \\
 &= \varepsilon_{mb} \left[\hat{D}_{01} + \hat{D}_{51} \varphi \sin \chi\varphi + \left(\hat{D}_{52} \varphi \sin \chi\varphi + \hat{D}_{62} \varphi \cos \chi\varphi \right) \frac{\mathcal{P}}{\vartheta} \right], \quad (53a)
 \end{aligned}$$

where

$$\hat{D}_{01} = -\frac{m}{\chi^4}, \quad \hat{D}_{51} = -\frac{A_{31}m}{2\chi^3}, \quad \hat{D}_{52} = -\frac{A_{32}m}{2\chi^3}, \quad \hat{D}_{62} = \frac{A_{42}m}{2\chi^3}. \quad (53b)$$

With the knowledge of the integration constants

$$\begin{aligned} W_{ob}(\varphi) = \varepsilon_{mb} \left[\hat{D}_{01} + \hat{D}_{11} \cos \varphi + \hat{D}_{41} \cos \chi\varphi + \hat{D}_{51} \varphi \sin \chi\varphi + \right. \\ \left. + \left(\hat{D}_{12} \cos \varphi + \hat{D}_{22} H \sin \varphi + \hat{D}_{32} H \sin \chi\varphi + \hat{D}_{42} \cos \chi\varphi + \right. \right. \\ \left. \left. + \hat{D}_{52} \varphi \sin \chi\varphi + \hat{D}_{62} H \varphi \cos \chi\varphi \right) \frac{\mathcal{P}}{\vartheta} \right] \quad (54) \end{aligned}$$

is the solution for the complete arch. The increment in the rotation field for shallow arches is given by

$$\begin{aligned} -\psi_{o\eta b} \simeq W_{ob}^{(1)} = \varepsilon_{mb} \left[E_{11} \sin \varphi + E_{41} \sin \chi\varphi + E_{51} \varphi \cos \chi\varphi + \right. \\ \left. + (E_{12} \sin \varphi + E_{22} \cos \varphi + E_{32} \cos \chi\varphi + E_{42} \sin \chi\varphi + \right. \\ \left. E_{52} \varphi \cos \chi\varphi + E_{62} \varphi \sin \chi\varphi) \frac{\mathcal{P}}{\vartheta} \right], \quad (55) \end{aligned}$$

where

$$\begin{aligned} E_{11} = -\hat{D}_{11}, \quad E_{41} = \hat{D}_{51} - \hat{D}_{41}\chi, \quad E_{51} = \hat{D}_{51}\chi, \quad E_{12} = -\hat{D}_{12}, \quad E_{22} = \hat{D}_{22}H, \\ E_{32} = \hat{D}_{32}H\chi + \hat{D}_{62}H, \quad E_{42} = \hat{D}_{52} - \hat{D}_{42}\chi, \quad E_{52} = \hat{D}_{52}, \quad E_{62} = -\hat{D}_{62}H. \end{aligned} \quad (56)$$

We can now calculate the mathematical average of the strain increment for the right half arch on the basis of (43). We get

$$1 = \frac{1}{\vartheta \varepsilon_{mb}} \int_0^{\vartheta} \left(U_{ob}^{(1)} + W_{ob} + W_o^{(1)} W_{ob}^{(1)} \right) d\varphi = J_2 \mathcal{P}^2 + J_1 \mathcal{P} + J_0, \quad (57)$$

where the right side is also independent of ε_{mb} . Formulae for the coefficients (integrals) J_0 , J_1 and J_2 are presented in Appendix A.1. Though the corresponding integrals can be given in a closed form, these are very long and are therefore omitted.

6. COMPUTATIONAL RESULTS

6.1. What to compute? In this section results are presented for four different magnitudes of the parameter m . At first, we investigate how the spring stiffness affects the endpoints of the typical buckling intervals. Then the critical loads are calculated. The results are comparable with those obtained by Bradford et al. in [15] and [17] using more neglects but, due to this fact, arriving at analytical solutions. When $\mathcal{S} = 0$ and $\mathcal{S} \rightarrow \infty$ our results – since they are based on a similar mechanical model – coincide with those valid both for pinned-pinned [20] and for fixed-fixed [21] arches.

6.2. Limits for the characteristic buckling intervals. There are four intervals of interest regarding the buckling behavior of symmetrically supported shallow arches. For a given ϑ , the endpoints of these intervals are functions of m , $\chi(\varepsilon_m)$ and \mathcal{S} . The lower limit of antisymmetric buckling can be obtained from the condition that the discriminant of (40) should be real when the antisymmetric critical strain (46) is substituted, consequently inequality

$$[I_1^2 - 4I_2(I_0 - \varepsilon_{m\ cr\ anti})] \Big|_{\chi^\vartheta = \mathfrak{F}} \geq 0 \tag{58}$$

should be fulfilled. We remark that when the spring stiffness is zero – i.e. the arch is pinned-pinned – instead of using the exact solution we assumed that $\mathfrak{F} = \pi - 10^{-4}$. It is also possible in certain cases that a real antisymmetric solution vanishes, so there is an upper limit also in the investigated $\vartheta = 0 \dots 1.5$ range. The upper limit is obtained by using an algorithm which monitors at what value of \mathcal{S} there exists no real solution any longer if $\chi^\vartheta = \mathfrak{F}$.

When evaluating the critical antisymmetric and symmetric buckling loads against the geometry of the arch, we find that these two curves sometimes intersect each other. This intersection point varies with \mathcal{S} . There is a switch between the symmetric and antisymmetric buckling modes at the intersection point as it is shown in Section 6.4. Prior to the intersection, the symmetric buckling shape governs. However, after this intersection, the bifurcation point is located before the limit point of the corresponding primary equilibrium path, which means that antisymmetric buckling occurs first. (To better understand the meaning of limit point see Figure 12). This switch can be found when (40) and (57) are equal at $\chi^\vartheta = \mathfrak{F}$ with all the other parameters being the same:

$$[I_2\mathcal{P}^2 + I_1\mathcal{P} + I_0 - \varepsilon_m] \Big|_{\mathfrak{F}, m, \mathcal{S}, \mathcal{P}} = [J_2\mathcal{P}^2 + J_1\mathcal{P} + J_0] \Big|_{\mathfrak{F}, m, \mathcal{S}, \mathcal{P}} \tag{59}$$

Finally, the lower endpoint for symmetric buckling, below which there is no buckling at all, is obtained by substituting the lowest symmetric solution (49) into the pre-buckling averaged strain (40) when the discriminant is set to zero:

$$[I_1^2 - 4I_2(I_0 - \varepsilon_{m\ cr\ sym})] \Big|_{\chi^\vartheta = \mathfrak{G}} = 0. \tag{60}$$

Now we turn the attention to the evaluation. Choosing $m = 1\,000$, Figure 4 shows the effects of the dimensionless spring stiffness in terms of the semi-vertex angle. When $\mathcal{S} = 0$, we get back the results valid for a pinned-pinned arch. Thus, when $\vartheta \leq 0.347$ there is no buckling – see the range denoted by (I). Then, up until $\vartheta = 0.5$, only symmetric limit point buckling can occur at the right loading level (II). Even though a bifurcation point (and therefore the possibility of antisymmetric buckling) appears when further increasing ϑ (III), still the symmetric shape is the dominant up until the intersection point of the symmetric and antisymmetric buckling curves at $\vartheta = 0.553$. At this point the buckling loads and strains are the same for symmetric and antisymmetric buckling and it holds a switch between the buckling types since above it (IV) the bifurcation point is located on the stable branch of the primary

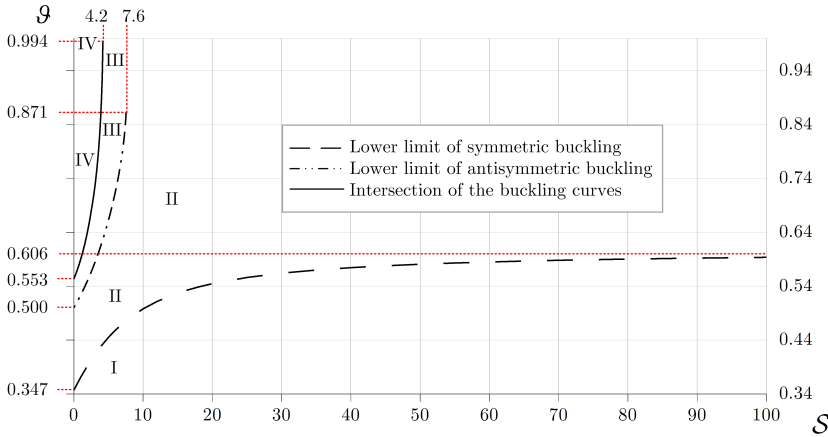


Figure 4. Typical buckling ranges when $m = 1000$.

equilibrium path as it will be shown later. Apart from the range limits, there are no any other differences as long as $S \leq 4.2$. Passing this value results in the disappearance of the intersection point of the buckling curves, therefore antisymmetric buckling is only possible after symmetric buckling. Another limit of importance is $S = 7.6$, since above that, the bifurcation point vanishes. It can also be seen that as S approaches to infinity from below – i.e. the arch becomes fixed – the switch between no buckling and symmetric buckling can be found at $\vartheta = 0.606$. The results when $[S = 0] (S \rightarrow \infty)$ are in a complete accord with what have been achieved in [20], [21]. This statement is valid for all the forthcoming results as well.

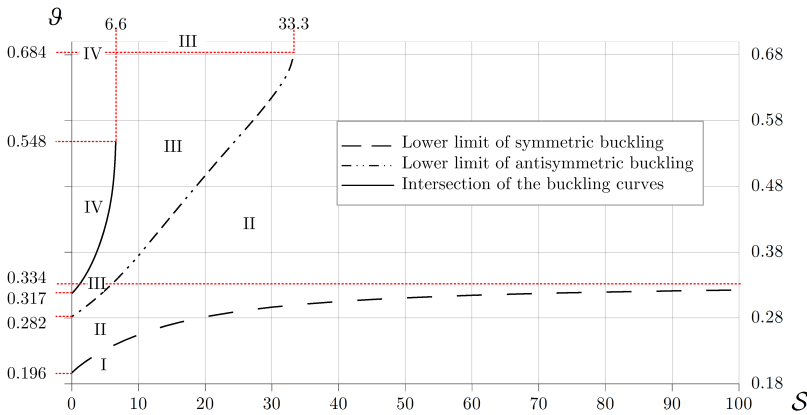


Figure 5. Typical buckling ranges when $m = 10000$.

The behavior of arches with $m = 10000$ is very similar to the former description – see Figure 5. This time an intersection point can be found up until $S = 6.6$ and an upper limit for antisymmetric buckling until $S \leq 33.3$. So these points show an

increase in \mathcal{S} as m is increased. It is also noticeable that increasing m yields a decrease in all the typical buckling endpoints in ϑ .

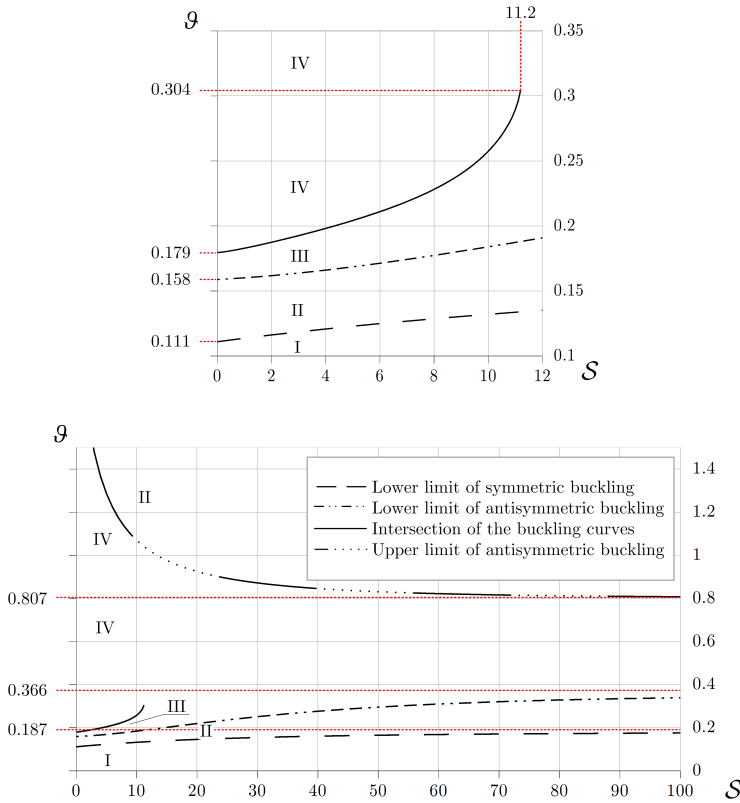


Figure 6. Typical buckling ranges when $m = 100\,000$.

More complex are the results in Figure 6 obtained for $m = 100\,000$, since the presence of an upper limit for antisymmetric buckling is experienced above $\mathcal{S}(\vartheta < 1.5) = 2.83$. Therefore, if $\mathcal{S} = 0 \dots 2.83$ there is a range in which there is no buckling (*I*). It is followed by the range of symmetric buckling only (*II*). Then antisymmetric buckling comes after symmetric buckling (*III*). After that, for all included angles, the antisymmetric shape governs. However, for $\mathcal{S} = 2.83 \dots 11.2$ after range (*IV*) the symmetric shape becomes again the dominant (*II*), since the possibility of antisymmetric buckling vanishes. A further increase in the spring stiffness yields the vanishing of the intersection point, so above range (*I*) the symmetric shape governs.

The characteristics of the curves valid for $m = 1\,000\,000$ in Figure 7 are very similar to that described in relation with $m = 100\,000$. So an increase in m results in a slight increase in the upper limit for antisymmetric buckling and a decrease in all other limits expressed in ϑ .

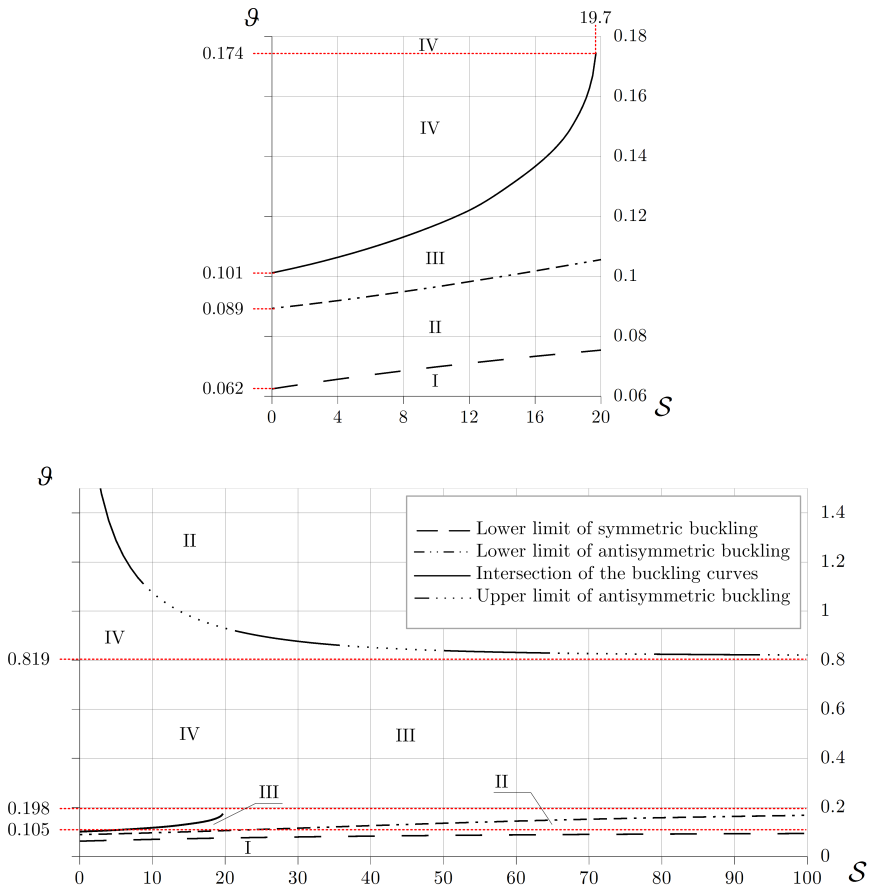


Figure 7. The typical buckling ranges when $m = 1\,000\,000$.

6.3. Buckling curves. In what follows, the governing buckling curves are drawn for four magnitudes of m . In each of these graphs, curves are presented for $\mathcal{S} = 0$ (pinned-pinned arch); $\mathcal{S} = 10^{20}$ (fixed-fixed arch with a very good accuracy) and $\mathcal{S} = 1$ (rotationally restrained arch) with the restriction that when both symmetric and antisymmetric shape is possible only the one, which comes prior in the load-deflection curve is plotted, since that is the dominant – see Section 6.4.

Antisymmetric buckling can be evaluated upon substitution of the critical strain for antisymmetric buckling from (47) into the averaged pre-buckling strain (40), therefore

$$\mathcal{P} = \frac{-I_1 \pm \sqrt{I_1^2 - 4(I_0 - \varepsilon_{m\ cr\ anti})I_2}}{2I_2} \Big|_{\chi^\theta = \mathfrak{F}} \quad (61)$$

Here we get two solutions for the load but only the one in relation with the first bifurcation point is presented.

As for symmetric buckling we have two unknowns – the force and the critical strain. We also have two equations – one obtained from the averaged pre- (40) and one from the averaged post-buckling strain (57). Solving these simultaneously

$$[I_2\mathcal{P}^2 + I_1\mathcal{P} + I_0 - \varepsilon_m] \Big|_{\chi, \vartheta, \mathcal{S}, m} = [J_2\mathcal{P}^2 + J_1\mathcal{P} + J_0] \Big|_{\chi, \vartheta, \mathcal{S}, m} \quad (62)$$

leads to the lowest buckling load. In Figure 8, $m = 1000$. The lower limits for symmetric buckling are $\vartheta(\mathcal{S} = 0) = 0.346$; $\vartheta(\mathcal{S} = 1) = 0.371$ and $\vartheta(\mathcal{S} = 10^{20}) = 0.606$. This buckling type is dominant for fixed-fixed arches throughout the whole interval while for the other two cases an intersection point was found with the corresponding antisymmetric curve at $\vartheta(\mathcal{S} = 0) = 0.553$ and $\vartheta(\mathcal{S} = 1) = 0.590$. Above these the antisymmetric buckling governs. It can therefore be seen that increasing the value of \mathcal{S} results that the lower limit of symmetric buckling and the intersection point moves to the right in the scale with increasing corresponding buckling loads. It is also clear that arches with rotationally restrained ends can bear such loading levels, which are between the critical loads for pinned-pinned and fixed-fixed arches. It is generally quite a notable range in \mathcal{P} so account for such restraints seems inevitable.

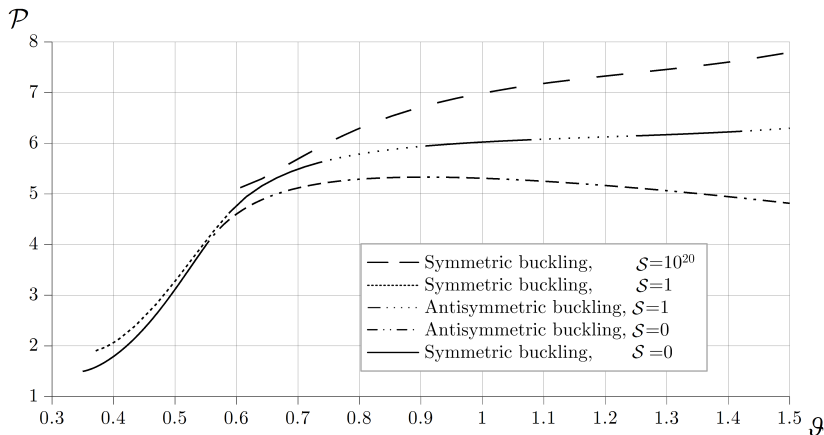


Figure 8. Buckling loads versus the semi-vertex angle when $m = 1000$.

Setting m to 10000 yields what is shown in Figure 9. Now the lower endpoints for symmetric buckling are $\vartheta(\mathcal{S} = 0) = 0.196$; $\vartheta(\mathcal{S} = 1) = 0.205$ and $\vartheta(\mathcal{S} = 10^{20}) = 0.334$ so the increase in m decreases this limit as it has already been pointed out in relation with Figure 5. It turns out that the intersection point in ϑ increases as the spring stiffness is increased: $\vartheta(\mathcal{S} = 0) = 0.317$; $\vartheta(\mathcal{S} = 1) = 0.328$. Above $\mathcal{S} = 6.6$, this point vanishes. It is also clear that the symmetric buckling curves of the two lowest stiffnesses run quite close compared to $m = 1000$. (This is the reason why this part is enlarged on the top part of the figure.) Above $\vartheta = 0.3$, they almost coincide. The critical load for any \mathcal{S} is generally greater this time compared to the results when $m = 1000$.

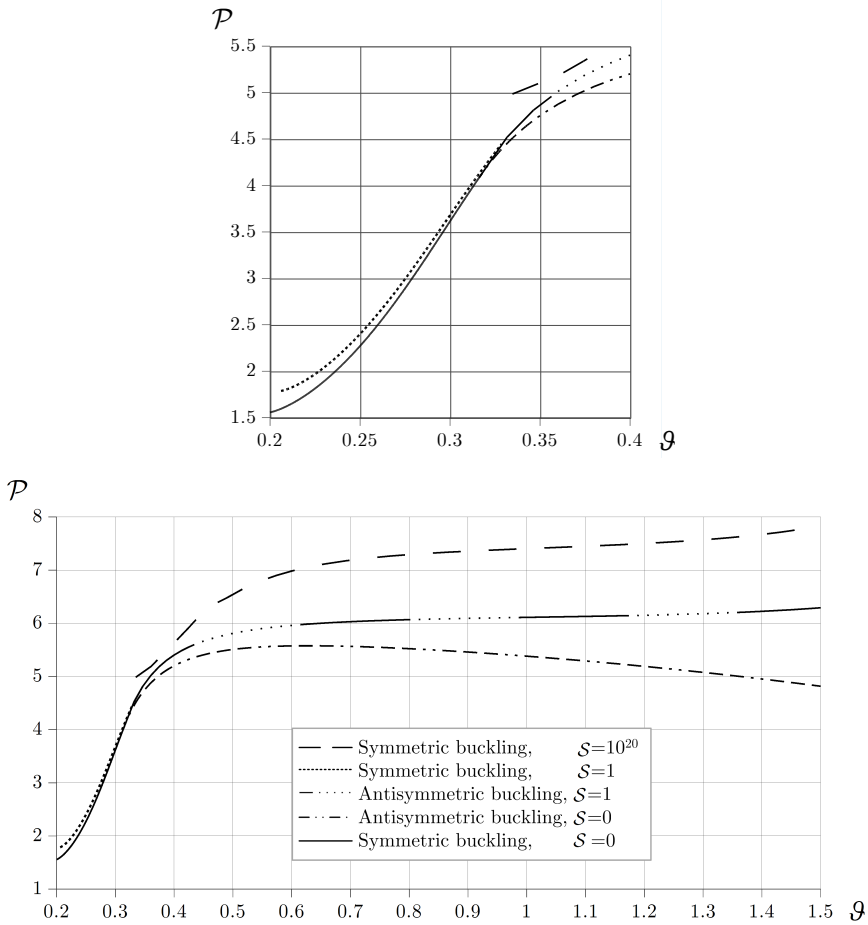


Figure 9. Buckling loads versus the semi-vertex angle when $m = 10\,000$.

In Figure 10, m is 100 000. The lower limit of symmetric buckling happens to decrease further but slowly: $\vartheta(\mathcal{S} = 0) = 0.111$; $\vartheta(\mathcal{S} = 1) = 0.113$ and $\vartheta(\mathcal{S} = 10^{20}) = 0.187$, while the intersection points occur at $\vartheta(\mathcal{S} = 0) = 0.179$; $\vartheta(\mathcal{S} = 1) = 0.182$. This time the symmetric curves are again closer to each other and the starting points of all the curves are closer to the origin.

With $m = 1\,000\,000$, we find that $\vartheta(\mathcal{S} = 0) = 0.062$; $\vartheta(\mathcal{S} = 1) = 0.063$ and $\vartheta(\mathcal{S} = 10^{20}) = 0.105$ are the lower limits for symmetric buckling and $\vartheta(\mathcal{S} = 0) = 0.101$; $\vartheta(\mathcal{S} = 1) = 0.102$ for the intersection point. This intersection point exists until $\mathcal{S} = 19.7$. The symmetric buckling curves for the two lowest stiffnesses coincide with a very good accuracy in their quite narrow interval in ϑ . Generally, the differences compared to $m = 100\,000$ are not that relevant when moving from $m = 1\,000$ to $m = 10\,000$.

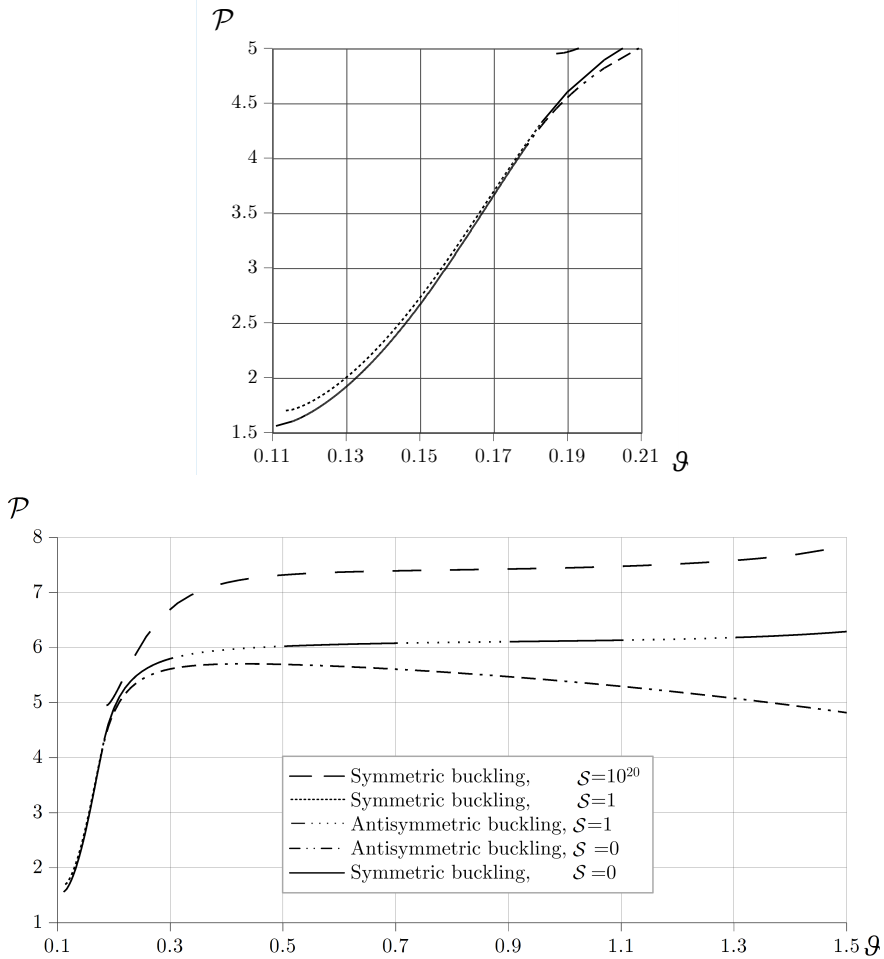


Figure 10. Buckling loads versus the semi-vertex angle when $m = 100\,000$.

It is clear from the corresponding figures that the presence of the springs have a huge effect on the buckling load. For instance, if $m = 1\,000\,000$ and $\vartheta = 1$ the critical dimensionless load varies between 5.4 and 7.5. This range becomes greater when the central angle is greater as it turns out.

The results of the new model for symmetric buckling are verified by finite element computations using Abaqus 6.7. The cross-section considered is rectangular with $0.01 [m]$ width and $0.005 [m]$ height and the Young's modulus is $2 \cdot 10^{11} [Pa]$. B22 (3-node quadratic Timoshenko) beam elements and the Static,Riks step have been used to draw the load-deflection diagrams. Results are gathered in Table 4. It can be seen that the greatest differences (4.4%) are experienced when $m = 10^6$ and $\vartheta = 1.366$, so predictions of the new model for not so shallow arches also seem to be quite good.

This new model, anyway, generally yields lower critical loads except when $m = 10^3$ and $\vartheta = 0.641$.

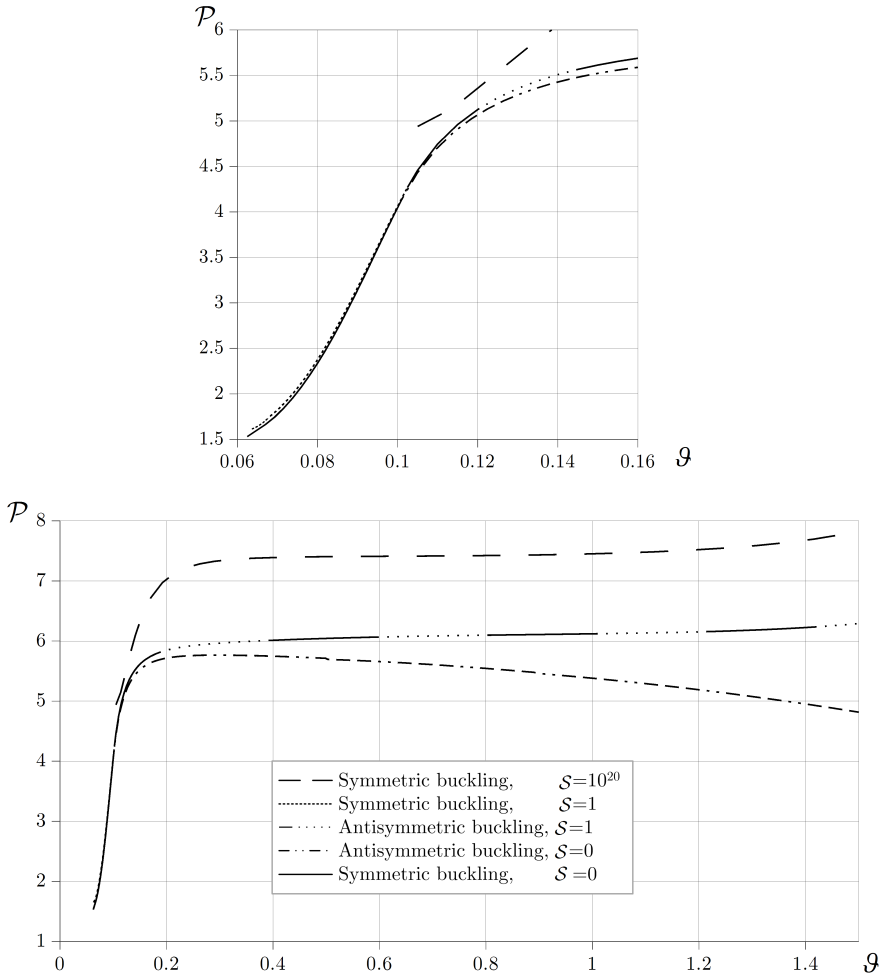


Figure 11. Buckling loads versus the semi-vertex angle when $m = 1\,000\,000$.

Table 4. Some control results regarding the symmetric buckling loads.

\mathcal{S}	m	ϑ	$\mathcal{P}_{\text{Abaqus}}$	$\mathcal{P}_{\text{New model}}$
0/10/10 ²⁰	10 ³	0.641	4.98 / 5.03 / 5.09	5.23 / 5.26 / 5.29
0/10/10 ²⁰	10 ³	1.052	6.78 / 6.83 / 6.99	6.70 / 6.86 / 7.09
0/10/10 ²⁰	10 ³	1.416	7.48 / 7.51 / 7.71	7.36 / 7.43 / 7.62
0/100/10 ²⁰	10 ⁶	0.289	6.75 / 7.20 / 7.38	6.69 / 7.14 / 7.32
0/10/10 ²⁰	10 ⁶	0.782	6.98 / 7.18 / 7.52	6.76 / 6.99 / 7.42
0/10/10 ²⁰	10 ⁶	1.366	7.58 / 7.70 / 7.98	7.26 / 7.39 / 7.64

6.4. **The primary equilibrium paths and the load-strain relationships.** In Figure 12 on the horizontal axis, the dimensionless displacement of the crown point W_{oC} is plotted against the dimensionless load \mathcal{P} for arches with $m = 100\,000$. The former quantity is obtained by dividing the displacement (36) at $\varphi = 0$ by the rise of the arch:

$$W_{oC} = \frac{-W_o|_{\varphi=0}}{1 - \cos \vartheta}. \tag{63}$$

There are four central angles picked to represent the different path types when $\mathcal{S} = 1$ (continuous lines in the forthcoming figures). Results for $\mathcal{S} = 0$ (fine dashed lines), $\mathcal{S} = 15$ (dotted lines) and $\mathcal{S} = 10^{20}$ (dashed lines) are also included. When $\vartheta = 0.113$, the slope is always positive and there is neither limit point nor bifurcation point for the spring supported arches. This is also true for the fixed-fixed arch with, of course,

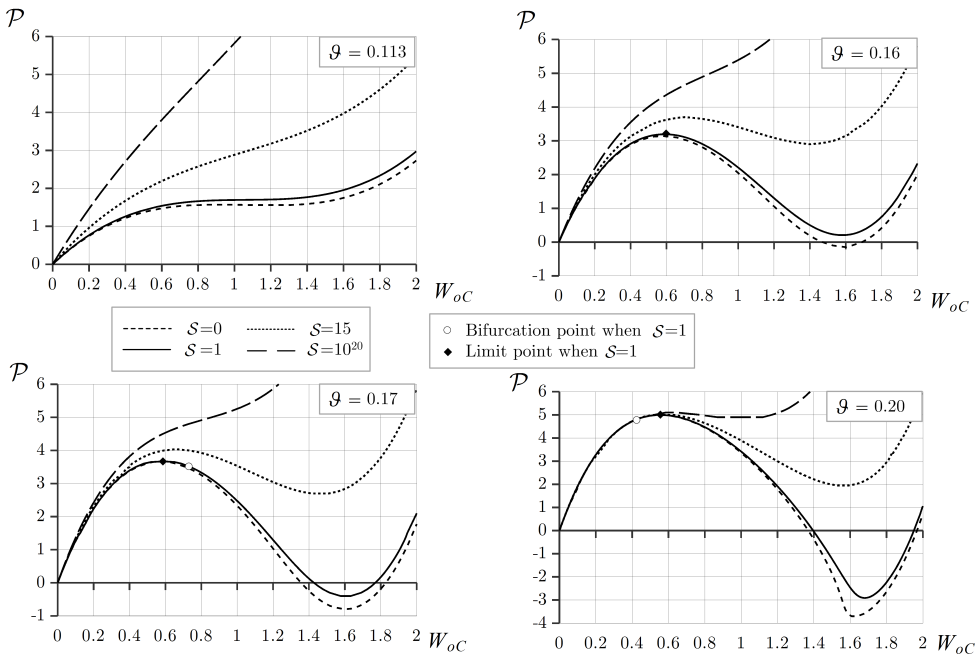


Figure 12. Dimensionless crown point displacement versus dimensionless load, $m = 100\,000$.

less displacement under the same load. However, for a stiff pin support, there appears a limit point. Increasing ϑ to 0.16 results in the appearance of a limit point for all but the fixed arch and the corresponding critical loads increase with \mathcal{S} . The fixed arch still has a positive tangent throughout but this curve generally runs closer to the others up until the first limit point on the curves for the restrained arches. At $\vartheta = 0.17$, there can be found a bifurcation point also but on the descending branch of the corresponding load-deflection curve for the pinned and restrained arches. Finally, for $\vartheta = 0.2$, there is a limit point in all four curves and these are quite close to each

other as well as all the first stable branches. This time, and above this central angle, the two picked rotationally restrained and the pinned arches buckle antisymmetrically first, as the bifurcation point is located on the stable branch, while fixed arches might still buckle symmetrically only.

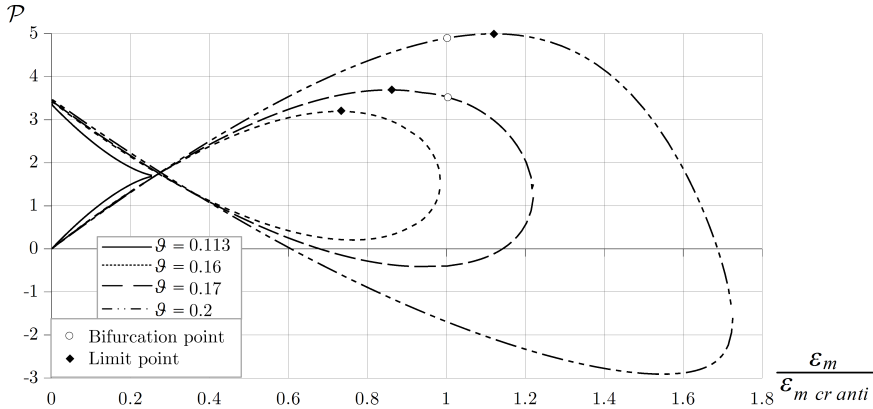


Figure 13. Typical load-strain relationships for $m = 100\,000$.

For $\mathcal{S} = 1$, the load-strain curves are drawn in Figure 13. On the horizontal axis the strain - critical strain ratio for antisymmetric buckling is measured. When $\vartheta = 0.113$, there are two different branches to which always a different \mathcal{P} belongs. If $\vartheta = 0.16$, the branches intersect each other and a limit point also appears at which symmetric snap-through buckling occurs. However, the $\varepsilon_m/\varepsilon_{m\,cr} = 1$ ratio is not reached, so there is no bifurcation. Increasing ϑ to 0.17, we experience that a bifurcation point appears after the limit point. Finally, if ϑ is greater or equal with 0.2, the bifurcation point comes prior to the limit point, so the antisymmetric buckling shape dominates for such shallow arches under a central load. It is also remarkable that every time there are two branches. The first one always starts at the origin, while the second one commences around 3.3 – 3.5 in \mathcal{P} , depending on the angle. There is an intersection point at $\varepsilon_m/\varepsilon_{m\,cr} \approx 0.27$ to which a loading level of $\mathcal{P} \approx 1.75$ belongs.

7. CONCLUSIONS

For rotationally restrained shallow arches with cross-sectional heterogeneity, a geometrically nonlinear model for the buckling analysis has been presented, partly on the basis of [17]. Nonlinearities were taken into account assuming the dominance of the rotation field. By using the principle of virtual work, we have derived the governing differential equations both for the pre-buckling and post-buckling state for arches under a central concentrated load and an arbitrary distributed load. Based on this achievement, the pre-buckling axial strain, as well as the post-buckling strain is constant on the centerline, when only a concentrated load is exerted at the crown

point. Heterogeneity appears in the formulation through the parameter $\chi(m)$. The equations of static equilibrium possess less neglects than the model derived and solved by Bradford et al. – see e.g., [15]; [17]. For this reason, the results computed by using the current model are more accurate even for greater central angles as well when they are compared to the previously cited articles. It should also be mentioned that for the rotation field the effect of the tangential displacement is neglected, which can cause erroneous predictions for deeper arches.

The evaluation process of the results are based on what Bradford et al. have used in their series of articles. We have presented how the different buckling limits and ranges are affected by the spring stiffness. It turns out that symmetrically supported shallow arches under a central load can buckle in an antisymmetric bifurcation mode with no strain increment at the moment of the stability loss, and in a symmetric snap-through mode, when there is a buckling strain. We have found, in an agreement with the earlier results, that an increase in \mathcal{S} results in an increase of the typical buckling limits for any fixed m . However, as m increases, those limits show a decrease. Evaluation of the critical loads for three different spring stiffness is carried out. If $\mathcal{S} = 0$ and $\mathcal{S} \rightarrow \infty$, we retrieved the results valid for pinned-pinned and fixed-fixed arches – see [20], [21]. The rotational restraints can have a considerable effect on the critical load a shallow arch can bear. For the same arches, but with different spring stiffnesses, the maximum difference between the critical loads can reach up to 25% when $\vartheta \leq 0.8$ and up to 57% for greater central angles. The load-deflection curves are also affected by the rotational restraints as it has been presented.

Acknowledgements. This research was supported by the **European Union** and the **State of Hungary, co-financed by the European Social Fund** in the framework of TÁMOP 4.2.4.A/2-11-1-2012-0001 'National Excellence Program'.

The author would also like to express his gratitude to the unknown reviewers for their valuable and constructive comments.

APPENDIX A.1. DETAILED MANIPULATIONS

Calculation of the pre-buckling averaged strain. Integral (38) is divided into two parts. The first part is

$$\frac{1}{\vartheta} \int_0^\vartheta W_o \, d\varphi = I_a + I_b \mathcal{P},$$

where

$$I_a = \frac{1}{\vartheta} \int_0^\vartheta \left(\frac{\chi^2 - 1}{\chi^2} + A_{11} \cos \varphi - \frac{A_{31}}{\chi^2} \cos \chi \varphi \right) \, d\varphi = \frac{\chi^2 - 1}{\chi^2} + A_{11} \frac{\sin \vartheta}{\vartheta} - \frac{A_{31}}{\chi^3} \frac{\sin \chi \vartheta}{\vartheta}, \tag{A.1}$$

$$I_b = \frac{1}{\vartheta^2} \int_0^\vartheta \left(A_{12} \cos \varphi + A_{22} \sin \varphi - \frac{A_{32}}{\chi^2} \cos \chi \varphi - \frac{A_{42}}{\chi^2} \sin \chi \varphi \right) \, d\varphi =$$

$$= \frac{1}{\vartheta^2} \left(A_{12} \sin \vartheta - A_{22} \cos \vartheta - A_{32} \frac{\sin \chi \vartheta}{\chi^3} + A_{42} \frac{\cos \chi \vartheta}{\chi^3} + A_{22} - \frac{A_{42}}{\chi^3} \right). \quad (\text{A.2})$$

The other part is of the form

$$\frac{1}{\vartheta} \int_0^\vartheta \frac{1}{2} \psi_{\sigma\eta}^2 d\varphi = I_c + I_d \mathcal{P} + I_e \mathcal{P}^2. \quad (\text{A.3})$$

Here

$$I_c = \frac{1}{2\vartheta} \int_0^\vartheta (B_{11} \sin \varphi + B_{31} \sin \chi \varphi)^2 d\varphi = \frac{-1}{8\vartheta \chi (1 - \chi^2)} \times \\ \times \left[B_{11}^2 \chi (\sin 2\vartheta - 2\vartheta) + \frac{8B_{11} B_{31} \chi (\sin \chi \vartheta \cos \vartheta - \chi \sin \vartheta \cos \chi \vartheta)}{(1 - \chi^2)} + B_{31}^2 (\sin 2\chi \vartheta - 2\vartheta \chi) \right]. \quad (\text{A.4})$$

To simplify the calculation it is advisable to decompose I_d :

$$I_d = \frac{1}{\vartheta^2} \int_0^\vartheta B_{11} \sin \varphi (B_{12} \sin \varphi + B_{22} \cos \varphi + B_{32} \sin \chi \varphi + B_{42} \cos \chi \varphi) d\varphi + \\ + \frac{1}{\vartheta^2} \int_0^\vartheta B_{31} \sin \chi \varphi (B_{12} \sin \varphi + B_{22} \cos \varphi + B_{32} \sin \chi \varphi + B_{42} \cos \chi \varphi) d\varphi = I_{d1} + I_{d2}, \quad (\text{A.5})$$

where

$$I_{d1} = \frac{-B_{11}}{4\vartheta^2 (1 - \chi^2)} \{ B_{12} (1 - \chi^2) (\sin 2\vartheta - 2\vartheta) + B_{22} (1 - \chi^2) (\cos 2\vartheta - 1) + \\ + 4B_{32} [\sin \chi \vartheta \cos \vartheta - \chi \cos \chi \vartheta \sin \vartheta] + 4B_{42} [\cos \vartheta \cos \chi \vartheta + \chi \sin \vartheta \sin \chi \vartheta - 1] \} \quad (\text{A.6a})$$

and

$$I_{d2} = \frac{B_{31}}{4\chi \vartheta^2 (1 - \chi^2)} \{ 4\chi B_{12} [\chi \sin \vartheta \cos \chi \vartheta - \sin \chi \vartheta \cos \vartheta] + \\ + 4\chi B_{22} [\sin \vartheta \sin \chi \vartheta + \chi \cos \vartheta \cos \chi \vartheta - \chi] + B_{32} (1 - \chi^2) [2\vartheta \chi - \sin 2\chi \vartheta] + \\ + B_{42} (1 - \chi^2) [1 - \cos 2\chi \vartheta] \}. \quad (\text{A.6b})$$

Moving on now to the calculation of I_e in (A.3), it is again worth decomposing the factor in question as

$$I_e = \frac{1}{\vartheta^3} \int_0^\vartheta (B_{12} \sin \varphi + B_{22} \cos \varphi + B_{32} \sin \chi \varphi + B_{42} \cos \chi \varphi) B_{12} \sin \varphi d\varphi + \\ + \frac{1}{2\vartheta^3} \int_0^\vartheta (B_{12} \sin \varphi + B_{22} \cos \varphi + B_{32} \sin \chi \varphi + B_{42} \cos \chi \varphi) B_{22} (\cos \varphi) d\varphi + \\ + \frac{1}{2\vartheta^3} \int_0^\vartheta (B_{12} \sin \varphi + B_{22} \cos \varphi + B_{32} \sin \chi \varphi + B_{42} \cos \chi \varphi) B_{32} (\sin \chi \varphi) d\varphi + \\ + \frac{1}{2\vartheta^3} \int_0^\vartheta (B_{12} \sin \varphi + B_{22} \cos \varphi + B_{32} \sin \chi \varphi + B_{42} \cos \chi \varphi) B_{42} (\cos \chi \varphi) d\varphi = \\ = I_{e1} + I_{e2} + I_{e3} + I_{e4}. \quad (\text{A.7})$$

The four terms in this sum are

$$I_{e1} = \frac{B_{12}}{8\vartheta^3 (1 - \chi^2)} \{ B_{12} (1 - \chi^2) [2\vartheta - \sin 2\vartheta] + B_{22} (1 - \chi^2) [1 - \cos 2\vartheta] + \\ + 4B_{32} (\chi \sin \vartheta \cos \chi \vartheta - \cos \vartheta \sin \chi \vartheta) + 4B_{42} [1 - \cos \vartheta \cos \chi \vartheta - \chi \sin \vartheta \sin \chi \vartheta] \}, \quad (\text{A.8a})$$

$$I_{e2} = \frac{-B_{22}}{8\vartheta^3(\chi^2-1)} \{B_{12}(\chi^2-1)(\cos 2\vartheta-1) - B_{22}(\chi^2-1)(\sin 2\vartheta+2\vartheta) + 4B_{32}[\chi \cos \vartheta \cos \chi\vartheta + \sin \vartheta \sin \chi\vartheta - \chi] + 4B_{42}[\sin \vartheta \cos \chi\vartheta - \chi \cos \vartheta \sin \chi\vartheta]\} , \quad (\text{A.8b})$$

$$I_{e3} = \frac{B_{32}}{8\chi\vartheta^3(1-\chi^2)} \{4B_{12}\chi[\chi \sin \vartheta \cos \chi\vartheta - \cos \vartheta \sin \chi\vartheta] + 4B_{22}\chi[\sin \vartheta \sin \chi\vartheta + \chi \cos \vartheta \cos \chi\vartheta - \chi] + B_{32}(1-\chi^2)[2\vartheta\chi - \sin 2\chi\vartheta] + B_{42}(1-\chi^2)[1 - \cos 2\chi\vartheta]\} \quad (\text{A.8c})$$

and

$$I_{e4} = \frac{B_{42}}{8\vartheta^3\chi(\chi^2-1)} \{4B_{12}\chi[\cos \vartheta \cos \chi\vartheta + \chi \sin \vartheta \sin \chi\vartheta - 1] + 4B_{22}\chi[\chi \cos \vartheta \sin \chi\vartheta - \sin \vartheta \cos \chi\vartheta] + 2B_{32}(\chi^2-1)\sin^2 \chi\vartheta + 2B_{42}(\chi^2-1)[\chi\vartheta + \sin \chi\vartheta \cos \chi\vartheta]\} . \quad (\text{A.8d})$$

With the knowledge of the previous integrals

$$I_0 = I_a + I_c, \quad I_1 = I_b + I_d \quad \text{and} \quad I_2 = I_e \quad (\text{A.9})$$

are the coefficients in (40).

Calculation of the averaged strain increment. Integrals J_a and J_b in

$$\frac{1}{\varepsilon_{mb}\vartheta} \int_0^\vartheta W_{ob} d\varphi = J_a + J_b \mathcal{P} \quad (\text{A.10})$$

are given below in closed forms:

$$J_a = \frac{1}{\vartheta} \int_0^\vartheta \left(\hat{D}_{01} + \hat{D}_{11} \cos \varphi + \hat{D}_{41} \cos \chi\varphi + \hat{D}_{51} \varphi \sin \chi\varphi \right) d\varphi = \frac{1}{\chi^2\vartheta} \left[\chi^2 \left(\hat{D}_{01}\vartheta + \hat{D}_{11} \sin \vartheta \right) + \hat{D}_{41}\chi \sin \chi\vartheta + \hat{D}_{51} (\sin \chi\vartheta - \chi\vartheta \cos \chi\vartheta) \right] , \quad (\text{A.11a})$$

$$J_b = \frac{1}{\vartheta^2} \int_0^\vartheta \left(\hat{D}_{12} \cos \varphi + \hat{D}_{22} \sin \varphi + \hat{D}_{32} \sin \chi\varphi + \hat{D}_{42} \cos \chi\varphi + \hat{D}_{52} \varphi \sin \chi\varphi + \hat{D}_{62} \varphi \cos \chi\varphi \right) d\varphi = \frac{1}{\chi^2\vartheta^2} \left[\chi^2 \left(\hat{D}_{12} \sin \vartheta + (1 - \cos \vartheta) \hat{D}_{22} \right) + \hat{D}_{52} \sin \chi\vartheta + (\cos \chi\vartheta - 1) \hat{D}_{62} + \chi \left((1 - \cos \chi\vartheta) \hat{D}_{32} + \hat{D}_{42} \sin \chi\vartheta - \hat{D}_{52}\vartheta \cos \chi\vartheta + \hat{D}_{62}\vartheta \sin \chi\vartheta \right) \right] . \quad (\text{A.11b})$$

As for the third integral in (57), let us recall formulae (37) and (55). Consequently, we get

$$\frac{1}{\vartheta\varepsilon_{mb}} \int_0^\vartheta W_o^{(1)} W_{ob}^{(1)} d\varphi = J_2 \mathcal{P}^2 + J_d \mathcal{P} + J_c, \quad (\text{A.12})$$

in which

$$J_c = -\frac{1}{\vartheta} \int_0^\vartheta (E_{11} \sin \varphi + E_{41} \sin \chi\varphi + E_{51} \varphi \cos \chi\varphi) (B_{11} \sin \varphi + B_{31} \sin \chi\varphi) d\varphi , \quad (\text{A.13a})$$

$$J_d = -\frac{1}{\vartheta^2} \int_0^\vartheta (B_{11} \sin \varphi + B_{31} \sin \chi\varphi) \times (E_{12} \sin \varphi + E_{22} \cos \varphi + E_{32} \cos \chi\varphi + E_{42} \sin \chi\varphi + E_{52} \varphi \cos \chi\varphi + E_{62} \varphi \sin \chi\varphi) d\varphi -$$

$$-\frac{1}{\vartheta^2} \int_0^\vartheta (E_{11} \sin \varphi + E_{41} \sin \chi\varphi + E_{51} \varphi \cos \chi\varphi) (B_{12} \sin \varphi + B_{22} \cos \varphi + B_{32} \sin \chi\varphi + B_{42} \cos \chi\varphi) d\varphi, \quad (\text{A.13b})$$

$$J_2 = -\frac{1}{\vartheta^3} \int_0^\vartheta (B_{12} \sin \varphi + B_{22} \cos \varphi + B_{32} \sin \chi\varphi + B_{42} \cos \chi\varphi) \times \\ \times (E_{12} \sin \varphi + E_{22} \cos \varphi + E_{32} \cos \chi\varphi + E_{42} \sin \chi\varphi + E_{52} \varphi \cos \chi\varphi + E_{62} \varphi \sin \chi\varphi) d\varphi. \quad (\text{A.13c})$$

Observe that

$$J_0 = J_a + J_c; \quad J_1 = J_b + J_d.$$

We would like to emphasize that the above integrals can all be given in closed forms. We omit them from being presented here as these are very complex. Any mathematical software, like Maple 16 or Scientific Work Place 5.5 can calculate these constants.

REFERENCES

1. BRESSE, J. A. C.: *Recherches analytiques sur la flexion et la résistance des pièces courbes*. MALLEY-BACHELIER AND CARILIAN-GOEURY AT V^r DALMONT, Paris, 1854.
2. HURLBRINK, E.: Festigkeitsberechnung von röhrenartigen Körpern, die unter äusserem Druck stehen. *Schiffbau*, **9**(14), (1907-1908), 517–523.
3. CHWALLA, E. and KOLLBRUNNER, C. F.: Beiträge zum Knickproblem des Bogenträgers und des Rahmens. *Stahlbau*, **11**(10), (1938), 73–78.
4. TIMOSHENKO, S. P. and GERE, J. M.: *Theory of Elastic Stability*. Engineering Societies Monographs, McGraw-Hill, 2nd edn., 1961.
5. SCHREYER, H. L. and MASUR, E. F.: Buckling of shallow arches. *Journal of Engineering Mechanics Division, ASCE*, **92**(EM4), (1965), 1–19.
6. DADDEPO, D. A. and SCHMIDT, R.: Sidesway buckling of deep circular arches under a concentrated load. *Journal of Applied Mechanics, ASME*, **36**(6), (1969), 325–327.
7. DYM, C. L.: Bifurcation analyses for shallow arches. *Journal of the Engineering Mechanics Division, ASCE*, **99**(EM2), (1973), 287.
8. DYM, C. L.: Buckling and postbuckling behaviour of steep compressible arches. *International Journal of Solids and Structures*, **9**(1), (1973), 129.
9. SZEIDL, G.: *Effect of Change in Length on the Natural Frequencies and Stability of Circular Beams*. Ph.D Thesis, Department of Mechanics, University of Miskolc, Hungary, 1975. (in Hungarian).
10. NOOR, A. K. and PETERS, J. M.: Mixed model and reduced/selective integration displacement models for nonlinear analysis of curved beams. *International Journal of Numerical Methods in Engineering*, **17**(4), (1981), 615–631.
11. CALBOUN, P. R. and DADDEPO, D. A.: Nonlinear finite element analysis of clamped arches. *Journal of Structural Engineering, ASCE*, **109**(3), (1983), 599–612.
12. ELIAS, Z. M. and CHEN, K. L.: Nonlinear shallow curved beam finite element. *Journal of Engineering Mechanics, ASCE*, **114**(6), (1988), 1076–1087.
13. WEN, R. K. and SUHENDRO, B.: Nonlinear curved beam element for arch structures. *Journal of Structural Engineering, ASCE*, **117**(11), (1991), 3496–3515.

14. PI, Y. L. and TRAHAIR, N. S.: Non-linear buckling and postbuckling of elastic arches. *Engineering Structures*, **20**(7), (1998), 571–579.
15. BRADFORD, M. A., UY, B., and PI, Y. L.: In-plane elastic stability of arches under a central concentrated load. *Journal of Engineering Mechanics*, **128**(7), (2002), 710–719.
16. PI, Y. L. and BRADFORD, M. A.: Dynamic buckling of shallow pin-ended arches under a sudden central concentrated load. *Journal of Sound and Vibration*, **317**, (2008), 898–917.
17. PI, Y. L., BRADFORD, M. A., and TIN-LOI, F.: Non-linear in-plane buckling of rotationally restrained shallow arches under a central concentrated load. *International Journal of Non-Linear Mechanics*, **43**, (2008), 1–17.
18. PI, Y. L. and BRADFORD, M. A.: Nonlinear analysis and buckling of shallow arches with unequal rotational end restraints. *Engineering Structures*, **46**, (2013), 615–630.
19. PLAUT, R.: Buckling of shallow arches with supports that stiffen when compressed. *ASCE Journal of Engineering Mechanics*, **116**, (1990), 973–976.
20. KISS, L. and SZEIDL, G.: In-plane stability of pinned-pinned heterogeneous curved beams under a concentrated radial load at the crown point. *Technische Mechanik*, *Accepted for publication*.
21. KISS, L. and SZEIDL, G.: In-plane stability of fixed-fixed heterogeneous curved beams under a concentrated radial load at the crown point. *Technische Mechanik*, *under review*.

NUMERICAL SOLUTIONS FOR STEADY VISCOUS FLOW PAST A CIRCULAR CYLINDER IN AN ALIGNED MAGNETIC FIELD

SEKHAR, T.V.S.

School of Basic Sciences, IIT Bhubaneswar,
Bhubaneswar - 751013, INDIA
sekhartvs@iitbbs.ac.in

SIVAKUMAR, R.

Department of Physics, Pondicherry University,
Pondicherry-605 014, INDIA
rs4670@gmail.com

HARISH KUMAR

Department of Physics, Pondicherry Engineering College,
Pondicherry-605 014, INDIA
harishkumarholla@rediffmail.com

[Received: March 26, 2004, Accepted: July 16, 2004.]

Abstract. The steady incompressible magneto-hydrodynamic (MHD) flow past a circular cylinder with an aligned magnetic field is studied for the Reynolds number (Re) up to 40, using the Hartmann number, M as the perturbation parameter. The multigrid method with defect correction technique is used to achieve the second order accurate solution of complete nonlinear Navier-Stokes equations. The magnetic Reynolds number is assumed to be small. It is observed that as M is increased the volume of the separation bubble decreases and drag coefficient increases. The graphs of streamlines, vorticity lines, surface pressure, surface vorticity and drag coefficient are presented and the effect of the magnetic field is discussed.

Mathematical Subject Classification: 76DXX, 76005, 76W05

Keywords: Navier-Stokes equations, MHD, Hartmann number, Multigrid method, Defect correction.

1. INTRODUCTION

In the plane flow of an incompressible, viscous, electrically conducting fluid over a solid body, the presence of a normal magnetic field at the surface has the effect of alleviating an adverse pressure gradient. One might expect that separation of the boundary layer would be delayed as a result. Indeed, since the degree to which the unfavorable pressure gradient is alleviated depends on the strength of the magnetic field, it is conceivable that separation could be completely suppressed. In a two dimensional flow of a liquid with small magnetic Reynolds number under the influence of an applied magnetic field, it has been proved that if the field is strong enough and

has the appropriate orientation, then separation of a viscous boundary layer can be prevented even up to rear stagnation point.

The problem of steady two-dimensional incompressible MHD flow past a circular cylinder with an applied magnetic field parallel to the main flow was investigated by Bramely [5] using the Oseen approximation. He later extended the problem to full Navier-Stokes equations for low Reynolds numbers using the method of series truncation [6]. Shanti Swarup and Sinha [22] investigated the steady flow of an incompressible, viscous, electrically conducting fluid past a non-magnetic and non-conducting circular cylinder for low Reynolds numbers [$Re = O(R_m)$ and $R_m \ll M \ll 1$], using the method of matched asymptotic expansions. Very recently, Sekhar *et al.* [21] studied the MHD flow past a sphere in an aligned magnetic field using the multigrid method.

In the absence of a magnetic field the present problem corresponds to the steady, viscous flow past a circular cylinder which has been studied by several researchers, including Dennis and Chang [8], Fornberg [9, 10], Kawamura and Kuwahara [15], Braza *et al.* [7], Karniadakis and Triantafyllou [14], Ingham and Tang [11] and Baranyi and Shirakashi [2]. Roshko [20], Bearman [4] and Norberg [16, 17] have studied the flow past a cylinder experimentally and have provided invaluable data. It is well known that the flow around a cylinder becomes unstable at $Re \sim 49$ due to periodic vortex shedding [25]. Bae *et al.* [1] investigated the conditions needed to facilitate the suppression of Kármán vortex excitation of a circular cylinder by a second cylinder set downstream in a cruciform arrangement. Baranyi [3] studied the unsteady momentum and heat transfer from a fixed cylinder using the finite difference method. In this paper, we discuss the flow of a conducting fluid past a circular cylinder for a range of Reynolds numbers from 10 to 40 and for the intermediate values of Hartmann number M using the finite difference method. The multigrid method with defect correction technique is applied to obtain the second order accurate solution.

2. MATHEMATICAL MODELLING

The equations governing the steady MHD flow of an incompressible fluid (with finite electrical conductivity σ) past a circular cylinder (of radius a) with uniform free-stream velocity \mathbf{U}_∞ and an uniformly applied magnetic field \mathbf{H}_∞ at large distances are, in non-dimensional form:

Momentum equation

$$\frac{Re}{2}(\mathbf{q} \cdot \nabla)\mathbf{q} = -\nabla p + \nabla^2 \mathbf{q} + \frac{M^2}{2R_m}[(\nabla \times \mathbf{H}) \times \mathbf{H}] \quad (1)$$

Ohm's law

$$\mathbf{j} = (\nabla \times \mathbf{H}) = \frac{R_m}{2}[\mathbf{E} + \mathbf{q} \times \mathbf{H}] \quad (2)$$

Equation of continuity

$$\nabla \cdot \mathbf{q} = 0 \quad (3)$$

where p is the pressure, \mathbf{q} the fluid velocity, \mathbf{H} the magnetic field, \mathbf{E} the electric field, \mathbf{j} the current density. The Reynolds number is $Re = 2\rho U_\infty a/\eta$ and $M = \mu H_\infty a(\sigma/\eta)^{1/2}$ is the Hartmann number. The magnetic Reynolds number is given by $R_m = U_\infty a\mu\sigma$. The viscosity, density and magnetic permeability of the fluid are η , ρ and μ respectively. The following non-dimensional terms were substituted to obtain the dimensionless differential equations:

$$\mathbf{q} = \frac{\mathbf{q}'}{U_\infty}, \quad p = \frac{a}{\rho\nu U_\infty} p', \quad r = \frac{r'}{a}, \quad \mathbf{H} = \frac{\mathbf{H}'}{H_\infty}$$

$$\mathbf{E} = \frac{\mathbf{E}'}{E_\infty}, \quad \mathbf{j} = \frac{\mathbf{j}'}{j_\infty}$$

where primed variables are dimensional quantities and ν is the kinematic viscosity, E_∞ and j_∞ are the magnitudes of electric field intensity and current density at infinity, respectively. In order to satisfy equation (2.3), the dimensionless stream function $\psi(r, \theta)$ is introduced such that

$$u = \frac{1}{r} \frac{\partial \psi}{\partial \theta}, \quad v = -\frac{\partial \psi}{\partial r} \quad (4)$$

where u and v are the dimensionless radial and transverse components of fluid velocity. Cylindrical polar coordinates (r, θ, z) are used in such a way that the flow is symmetric about $\theta = 0^\circ$ and $\theta = 180^\circ$. As the magnetic field and fluid flow are aligned at infinity, the electric field can be assumed to be zero. The problem can be simplified by assuming the magnetic Reynolds number to be small. The magnetic field must not be so large that the flow develops into a slug flow. It should be large enough to see the effect on separation but small enough for the flow to be a perturbation of the potential flow with zero magnetic field. We use the low- R_m approximation and ignore equation (2.2) as well as replace the magnetic field in all MHD equations by

$$\mathbf{H} = (-\cos \theta, \sin \theta, 0), \quad (5)$$

which will eliminate several nonlinear terms of unknown quantities in the governing equations. After eliminating pressure from equation (2.1), we get

$$\frac{Re}{2} [\nabla \times (\boldsymbol{\omega} \times \mathbf{q})] = \nabla^2 \boldsymbol{\omega} + \frac{M^2}{2R_m} [\nabla \times \{(\nabla \times \mathbf{H}) \times \mathbf{H}\}] \quad (6)$$

where

$$\boldsymbol{\omega} = \nabla \times \mathbf{q} \quad (7)$$

is the vorticity. Substitution of equation (2.2) in equation (2.6) gives

$$\nabla^2 \boldsymbol{\omega} = \frac{Re}{2} [\nabla \times (\boldsymbol{\omega} \times \mathbf{q})] - \frac{M^2}{4} [\nabla \times \{(\mathbf{q} \times \mathbf{H}) \times \mathbf{H}\}] \quad (8)$$

Expanding equations (2.7) and (2.8) we get

$$\frac{\partial^2 \psi}{\partial r^2} + \frac{1}{r} \frac{\partial \psi}{\partial r} + \frac{1}{r^2} \frac{\partial^2 \psi}{\partial \theta^2} = -\omega \quad (9)$$

and

$$\frac{\partial^2 \omega}{\partial r^2} + \frac{1}{r} \frac{\partial \omega}{\partial r} + \frac{1}{r^2} \frac{\partial^2 \omega}{\partial \theta^2} - \frac{Re}{2r} \left[\frac{\partial \psi}{\partial \theta} \frac{\partial \omega}{\partial r} - \frac{\partial \psi}{\partial r} \frac{\partial \omega}{\partial \theta} \right] = \frac{M^2}{4} \left[\omega \sin^2 \theta + \frac{\sin 2\theta}{r} \frac{\partial^2 \psi}{\partial r \partial \theta} - \frac{\sin 2\theta}{r^2} \frac{\partial \psi}{\partial \theta} - \cos 2\theta \frac{\partial^2 \psi}{\partial r^2} \right] \quad (10)$$

Since major velocity gradients occur near the body, we used the transformations $r = e^{\pi\xi}$ and $\theta = \pi\eta$ to concentrate the mesh spacing near the body. Then equations (2.9) and (2.10) can be written as

$$\frac{\partial^2 \psi}{\partial \xi^2} + \frac{\partial^2 \psi}{\partial \eta^2} + \pi^2 e^{2\pi\xi} \omega = 0 \quad (11)$$

and

$$\frac{\partial^2 \omega}{\partial \xi^2} + \frac{\partial^2 \omega}{\partial \eta^2} - \frac{Re}{2} \left[\frac{\partial \psi}{\partial \eta} \frac{\partial \omega}{\partial \xi} - \frac{\partial \psi}{\partial \xi} \frac{\partial \omega}{\partial \eta} \right] = \frac{M^2}{4} \left[\pi^2 e^{2\pi\xi} \omega \sin^2(\pi\eta) + \sin 2(\pi\eta) \frac{\partial^2 \psi}{\partial \xi \partial \eta} - \pi \sin 2(\pi\eta) \frac{\partial \psi}{\partial \eta} - \cos 2(\pi\eta) \frac{\partial^2 \psi}{\partial \xi^2} + \pi \cos 2(\pi\eta) \frac{\partial \psi}{\partial \xi} \right] \quad (12)$$

in the vorticity-stream function form. Equations (2.11) and (2.12) must now be solved subject to the following boundary conditions:

(1) On the surface of the cylinder; ($r = 1$), $\xi = 0$,

$$\psi = \frac{\partial \psi}{\partial \xi} = 0$$

$$\omega = -\frac{1}{\pi^2} \frac{\partial^2 \psi}{\partial \xi^2}$$

(2) At large distances from the cylinder; ($r \rightarrow \infty$), $\xi \rightarrow \infty$,

$$\psi \sim e^{\pi\xi} \sin(\pi\eta)$$

$$\omega \rightarrow 0$$

(3) Along the axis of symmetry ($\eta = 0, \eta = 1$), $\psi = 0$ and $\omega = 0$.

3. NUMERICAL METHOD

The coupled nonlinear Navier-Stokes equations are solved by first applying finite difference method and the resulting algebraic equations are solved by using the multigrid method. Here, a recursive multigrid procedure is employed in which the smoother is a point Gauss Seidel iteration and the usual coarse grid correction is applied as follows [23]. Let there be a sequence of computational grids G^1, G^2, \dots, G^l with G^k finer than G^{k-1} . Let $U^k \rightarrow \mathbf{R}$ be the space of grid functions on G^k , let $P^k : U^{k-1} \rightarrow U^k$ be a prolongation operator and let $R^k : U^{k+1} \rightarrow U^k$ be a restriction operator. Suppose

we have a nonlinear (system of) partial differential equation(s), discretized on G^1, G^2, \dots, G^l . On G^k , the algebraic problem to be solved is given by

$$A^k(u^k) = f^k$$

where, A^k is the matrix obtained by suitable discretization. If \hat{u} is the approximation to exact solution u , then, $(\hat{u} - u)$ represents the error e . Then, we have

$$Ae = -r = A\hat{u} - f \quad (13)$$

where, r is called the residue. The coarse grid approximation \bar{u} of $-e$ satisfies

$$\bar{A}\bar{u} = Rr$$

where, \bar{A} is the operator obtained by discretizing the original problem on a coarser grid and R is the restriction operator. If the grid under consideration is coarsest, then the above equation should be solved exactly. The coarse grid correction to be added to \hat{u} is $P\bar{u}$ (where P is the prolongation operator) given by

$$\hat{u} = \hat{u} + P\bar{u}$$

This represents one multigrid cycle. Solving on G^{l-1} by γ multigrid iterations results in the following recursive algorithm:

procedure MG(k, u, f)

begin if $k = 1$ **then** solve $A^1(u^1) = f^1$ **else**

begin $S_1(k, u, f)$

Choose $\tilde{u}^{k-1} \in U^{k-1}$

$$\tilde{f}^{k-1} = A^{k-1}(\tilde{u}^{k-1})$$

$$f^{k-1} = \tilde{f}^{k-1} + R^{k-1}(f^k - A^k(u^k))$$

for $i := 1$ **step** 1 **until** γ **do** MG($k - 1, u, f$)

$$u^k = u^k + P^k(u^{k-1} - \tilde{u}^{k-1})$$

$S_2(k, u, f)$

end

end MG

where, S denotes a smoother involving a small number of point Gauss Seidel iterations.

The initial solution is taken as $\psi = 0$ and $\omega = 0$ at all inner grid points except for ψ at $\xi = \infty$ where the boundary condition holds. In finding the solution for higher values of Re and M , the solution obtained for lower values of Re and M are used as starting solution. Among the two variables, ω and ψ , we first solved for ω and then for ψ . Convergence is said to have been achieved when the difference between two successive iterations m and $m + 1$, at all interior grid points, is less than 10^{-5} , i.e.,

$$|\psi^{m+1} - \psi^m| < 10^{-5}$$

and

$$|\omega^{m+1} - \omega^m| < 10^{-5}.$$

The restriction operator R_k^{k-1} transfers a fine grid function U^k to a coarse grid function U^{k-1} . On the other hand the prolongation operator, denoted as P_{k-1}^k , transfers a coarse grid function U^{k-1} to a fine grid function U^k . For the restriction operator, the simplest form is ‘injection’ where by the values of a function in the coarse grid are taken to be exactly the values at the corresponding points of the next fine grid *i.e.*,

$$(R_k^{k-1}u^k)_{i+1,j+1} = u_{2i+1,2j+1}^k.$$

We used the above injection operator throughout this study. For the prolongation operator the simplest form is derived using linear interpolation. Prolongation by linear interpolation introduces no ambiguity when the interpolated value is desired at the mid points of the boundaries of a mesh cell. The following 9-point prolongation operator defined by Wesseling [24] is used for the present study

$$\begin{aligned} (P_{k-1}^k u^{k-1})_{2i+1,2j+1} &= u_{i+1,j+1}^{k-1} \\ (P_{k-1}^k u^{k-1})_{2i+2,2j+1} &= \frac{1}{2} (u_{i+1,j+1}^{k-1} + u_{i+2,j+1}^{k-1}) \\ (P_{k-1}^k u^{k-1})_{2i+1,2j+2} &= \frac{1}{2} (u_{i+1,j+1}^{k-1} + u_{i+1,j+2}^{k-1}) \\ (P_{k-1}^k u^{k-1})_{2i+2,2j+2} &= \frac{1}{4} (u_{i+1,j+1}^{k-1} + u_{i+2,j+1}^{k-1} + u_{i+1,j+2}^{k-1} + u_{i+2,j+2}^{k-1}). \end{aligned}$$

The solution obtained by the above method is not second order accurate as we have approximated all terms by second order central difference method except convective terms which are approximated by first order upwind difference scheme to ensure diagonal dominance. In order to achieve second order accurate solution, the defect correction method is employed as follows. If \mathbf{B} is the operator obtained, for example, by first order upwind discretization and \mathbf{A} is that obtained by second order accurate discretization, then defect correction algorithm [12, 13] works as given below. At the start of defect correction, \bar{y} is a solution that is not second order accurate, and at the end of defect correction, \bar{y} is second order accurate.

```

begin Solve  $\mathbf{B}\bar{y} = b$ 
  for  $i := 1$  step 1 until  $n$  do
    solve  $By = b - A\bar{y} + B\bar{y}$ 
     $\bar{y} := y$ 
  od
end

```

Usually, in practice, it is sufficient to take $n = 1$ or 2.

4. RESULTS AND DISCUSSIONS

Full, nonlinear Navier-Stokes equations for the MHD flow past a circular cylinder are solved using the multigrid method with defect correction technique for the range of Reynolds numbers from 10 to 40 and for different values of Hartmann number M , using 512×512 as the finest grid with 256×256 , 128×128 and 64×64 as coarser

grids. The finite difference method is applied to the grid shown in Figure 1. We observed the separation at rear stagnation point for all Reynolds numbers considered in the present study, in $M = 0$ case (Figures 2–7). The length of the wake (l/a) and angle of the separation (θ_s) are found to increase with Re as observed by some researchers [8, 9]. With no magnetic field ($M = 0$), both length of the wake and angle of the separation values (Tables 1–3) are in good agreement with Dennis and Chang [8]. We observed that as the magnetic field is increased, the Lorentz forces dominate and produce a convective rate in a direction opposite to the flow resulting in the decrease of wake length and separation angle, for all Re values ($10 \leq Re \leq 40$). A similar phenomenon can be seen in the case of the translation of a sphere in a rotating viscous fluid [18, 19] and MHD flow past a sphere [21]. For $Re = 10$ the separation bubble disappeared completely at $M = 3$ (Figure 3). As the magnetic forces are proportional to and resist the flow of fluid in any other direction than that of the unperturbed magnetic field, near the cylinder, they produce changes in the pattern of the vorticity lines. The length of standing vortex is reduced slightly and the strength of the disturbance in front of the cylinder is increased with increasing magnetic field (Figures 8–13). It can also be seen that the radial component (u) of fluid velocity near the cylinder at $\theta = 90^\circ$ is suppressed more compared to the transverse component (v) as it (u) is not parallel to the magnetic field (Figures 16, 17). As the Hartmann number increases, the thickness of the boundary layer adjoining the cylinder surface decreases, indicating that it tends to zero for sufficiently large values of M ($M \gg 1$) (Figure 16). This may be attributed to the enhanced velocity gradients required by the viscous stresses to compete with the large magnetic forces.

The drag coefficients and surface pressure are calculated using the following relations:

Viscous drag coefficient

$$C_v = -\frac{4\pi}{Re} \int_0^1 \omega_{\xi=0} \sin(\pi\eta) d\eta \quad (14)$$

Pressure drag coefficient

$$C_p = \frac{4}{Re} \int_0^1 \left(\frac{\partial\omega}{\partial\xi} \right)_{\xi=0} \sin(\pi\eta) d\eta \quad (15)$$

Total drag coefficient

$$C_D = C_v + C_p \quad (16)$$

and surface pressure

$$P(0, \eta) = 1 - \frac{4}{\pi Re} \int_0^\infty \left(\frac{\partial\omega}{\partial\eta} \right)_{\eta=1} d\xi - \frac{4}{Re} \int_\eta^1 \left(\frac{\partial\omega}{\partial\xi} \right)_{\xi=0} d\eta \quad (17)$$

We found that as the thickness of the boundary layer decreases, the increased velocity gradients at the surface will increase the pressure drop (Figure 14) necessary to maintain the given flow rate. It can be seen from Figure 15 that the magnetic field tends to suppress the surface vorticity behind the cylinder thereby competing with the viscous diffusion of vorticity out from the surface. The observed flow field

is in accordance with the assumption that the effect of magnetic field is the small perturbation of zero field potential flow.

Table 1. Drag coefficient values for $Re = 10$

M	256×256			512×512			θ_s	$P(0,0)$	$P(0,1)$	(l/a)
	C_v	C_p	C_D	C_v	C_p	C_D				
0.00	1.23	1.57	2.80	1.24	1.58	2.82	29.40	-0.70	1.48	1.55
1.00	1.23	1.61	2.84	1.23	1.59	2.83	25.40	-0.73	1.48	1.34
2.00	1.23	1.70	2.93	1.23	1.70	2.93	14.06	-0.83	1.50	1.05
3.00	1.30	1.93	3.23	1.31	1.93	3.24	0	-1.06	1.53	0

Table 2. Drag coefficient values for $Re = 20$

M	256×256			512×512			θ_s	$P(0,0)$	$P(0,1)$	(l/a)
	C_v	C_p	C_D	C_v	C_p	C_D				
0.00	0.79	1.20	1.99	0.80	1.22	2.02	43.80	-0.53	1.26	2.81
3.00	0.79	1.26	2.05	0.79	1.26	2.05	34.71	-0.60	1.27	1.80
5.00	0.82	1.54	2.36	0.82	1.54	2.36	26.36	-0.87	1.30	1.40
7.00	0.89	1.90	2.79	0.89	1.90	2.79	21.72	-1.50	1.35	1.25

Table 3. Drag coefficient values for $Re = 40$

M	256×256			512×512			θ_s	$P(0,0)$	$P(0,1)$	(l/a)
	C_v	C_p	C_D	C_v	C_p	C_D				
0.00	0.51	0.97	1.48	0.51	0.97	1.48	53.59	-0.46	1.14	5.74
3.00	0.51	1.00	1.51	0.51	1.01	1.52	44.45	-0.47	1.14	3.81
5.00	0.53	1.15	1.68	0.53	1.15	1.68	36.01	-0.54	1.15	2.80
7.00	0.57	1.43	2.00	0.57	1.44	2.01	31.09	-0.68	1.15	2.30

Table 4. Drag coefficient values before and after defect correction for $M = 0$

Re	128×128		256×256		512×512	
	before DC	after DC	before DC	after DC	before DC	after DC
10	2.7186	2.7280	2.7561	2.7683	2.8133	2.8221
20	1.8826	1.8901	1.9905	1.9941	1.9954	2.0180
40	1.3851	1.3928	1.4644	1.4723	1.4742	1.4805

Table 5. Comparison of Drag coefficient values for $M = 0$

Re	Present results	Dennis and Chang [8]	Fornberg [9]	Ingham and Tang [11]
10	2.82	2.846	—	—
20	2.02	2.045	2.000	1.995
40	1.48	1.522	1.498	—

In the case of $M = 0$, the drag coefficient values are in good agreement with the earlier work [8, 9, 11]. The drag coefficient values before and after applying defect correction (DC) in three different grids 128×128 , 256×256 and 512×512 are given

in Table 4. The comparison of the drag coefficient values for $M = 0$ is given in Table 5 and the graph of drag coefficient versus Reynolds number is presented in Figure 18. It is observed that the effect of magnetic field decreases as Re increases up to the range considered in this study.

APPENDIX A. FIGURES

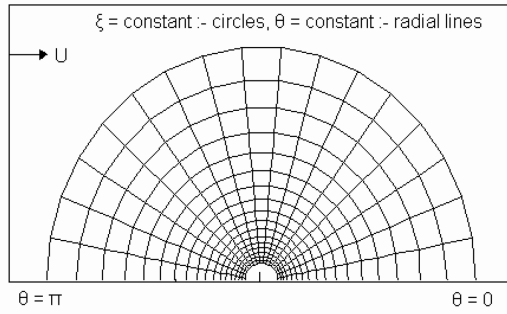


Figure 1. Finite difference grid

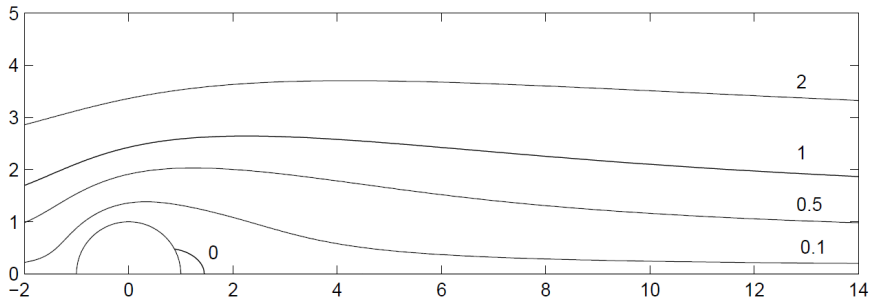


Figure 2. Streamlines for $Re = 10$, $M = 0$

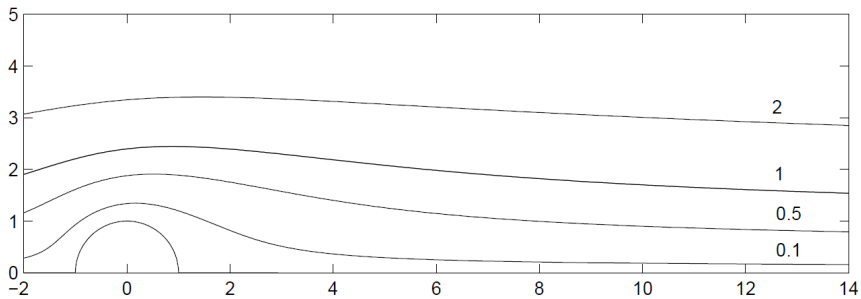
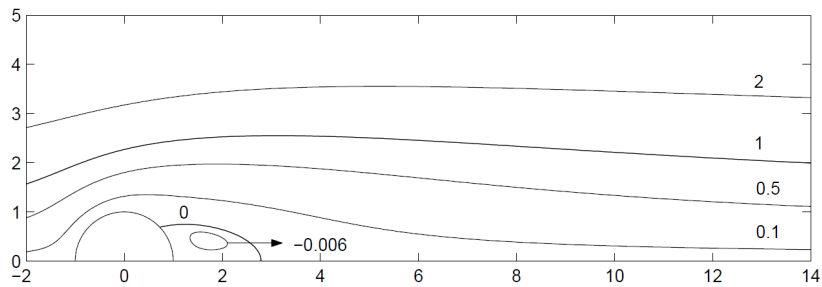
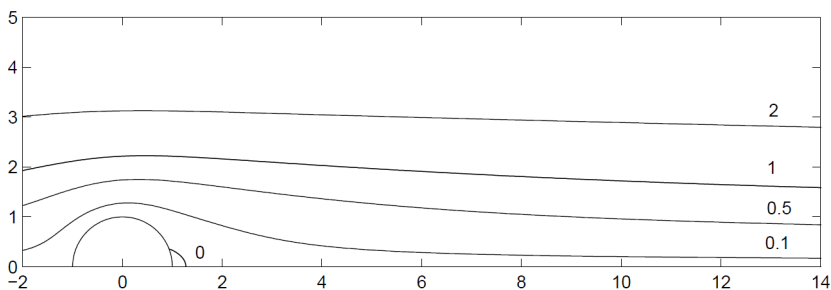
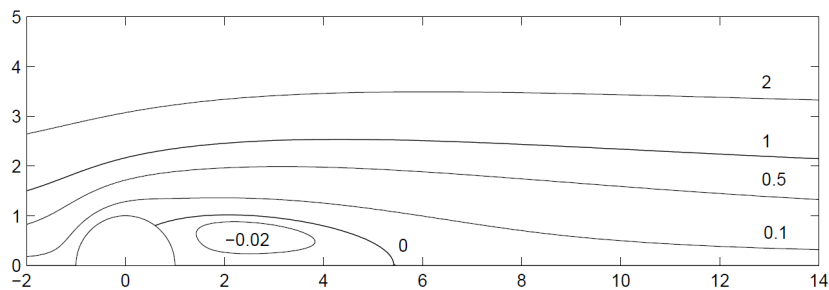
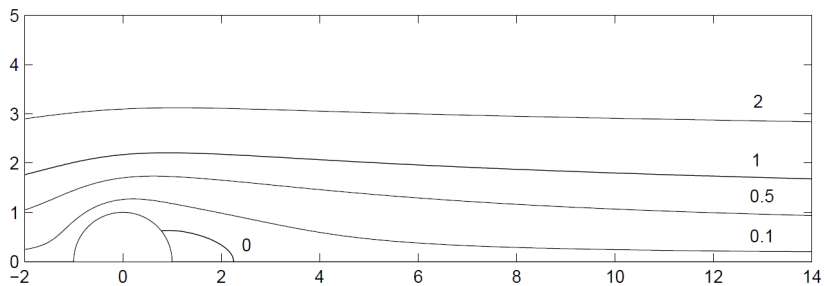


Figure 3. Streamlines for $Re = 10$, $M = 3$

Figure 4. Streamlines for $Re = 20$, $M = 0$ Figure 5. Streamlines for $Re = 20$, $M = 7$ Figure 6. Streamlines for $Re = 40$, $M = 0$ Figure 7. Streamlines for $Re = 40$, $M = 7$

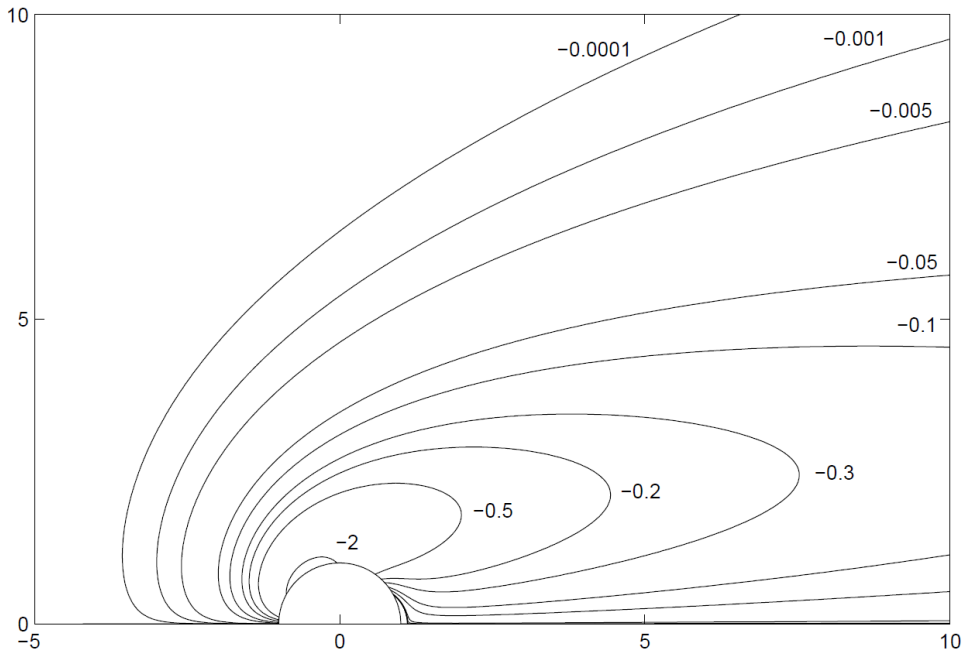


Figure 8. Vorticity lines for $Re = 10$, $M = 0$

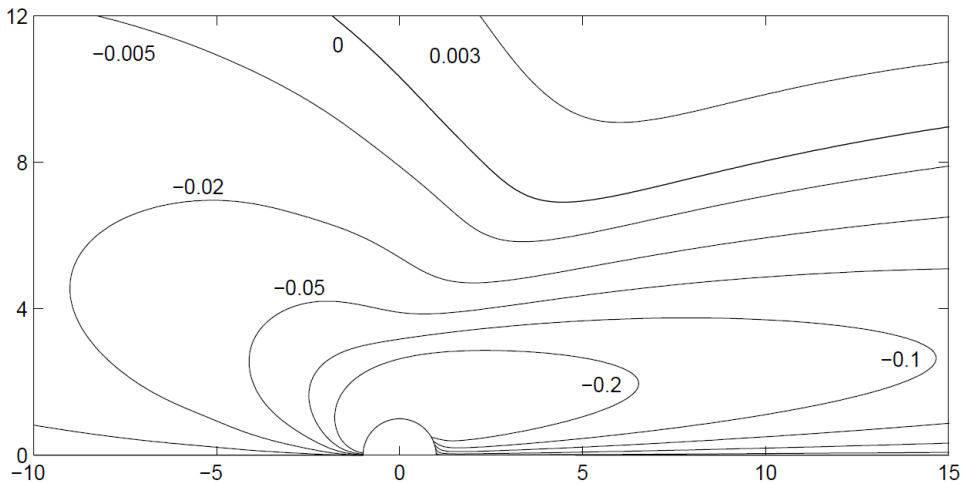


Figure 9. Vorticity lines for $Re = 10$, $M = 3$

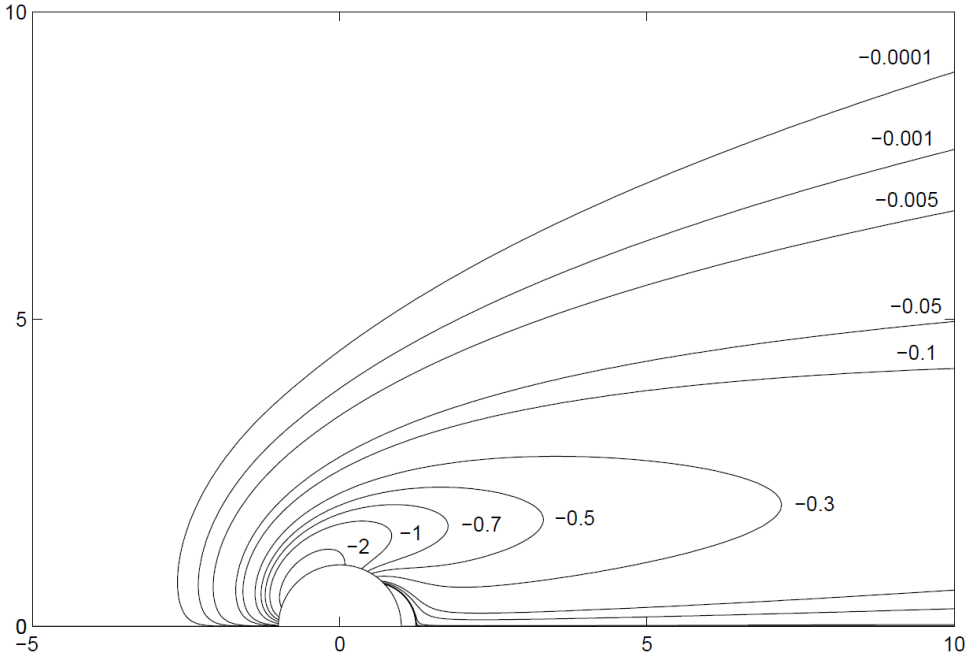


Figure 10. Vorticity lines for $Re = 20$, $M = 0$

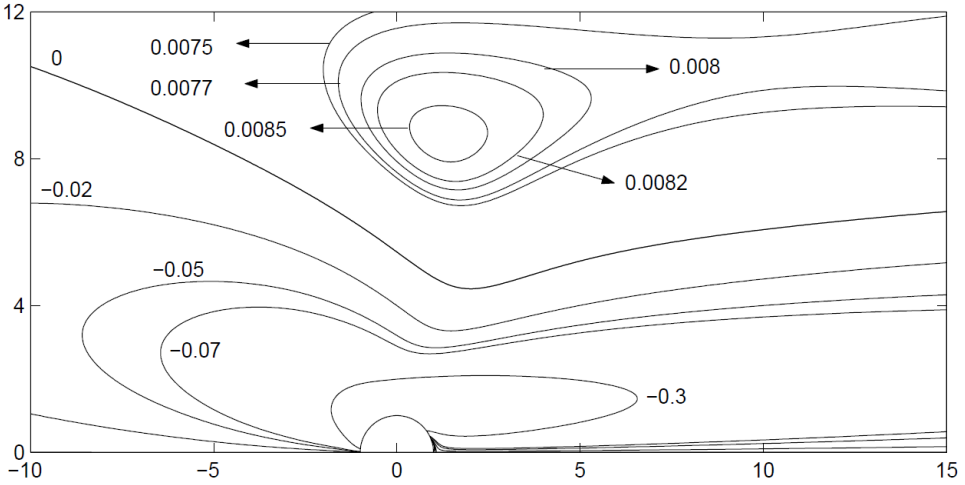


Figure 11. Vorticity lines for $Re = 20$, $M = 7$

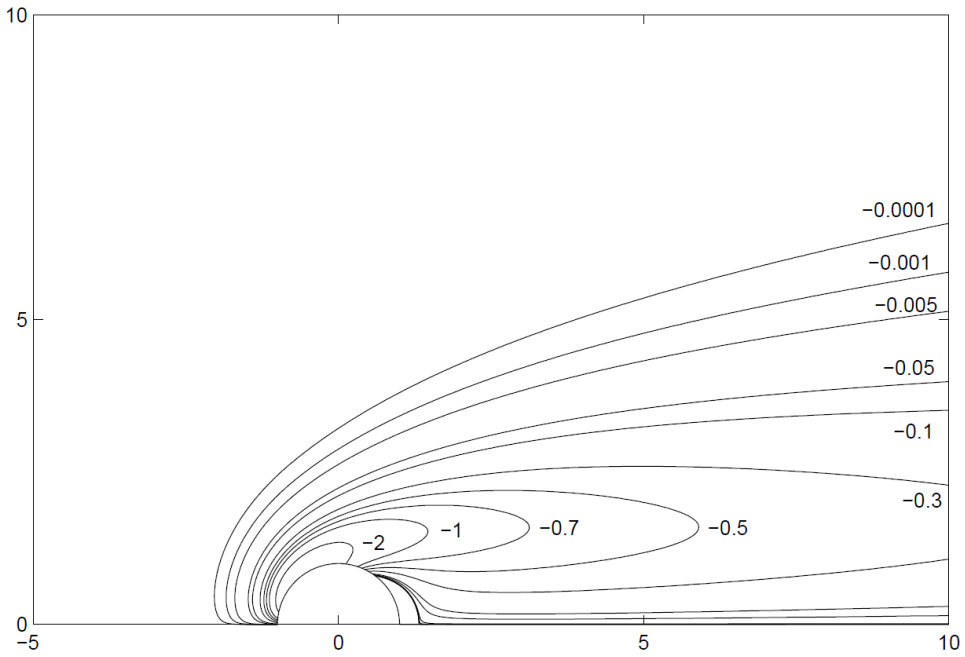


Figure 12. Vorticity lines for $Re = 40$, $M = 0$

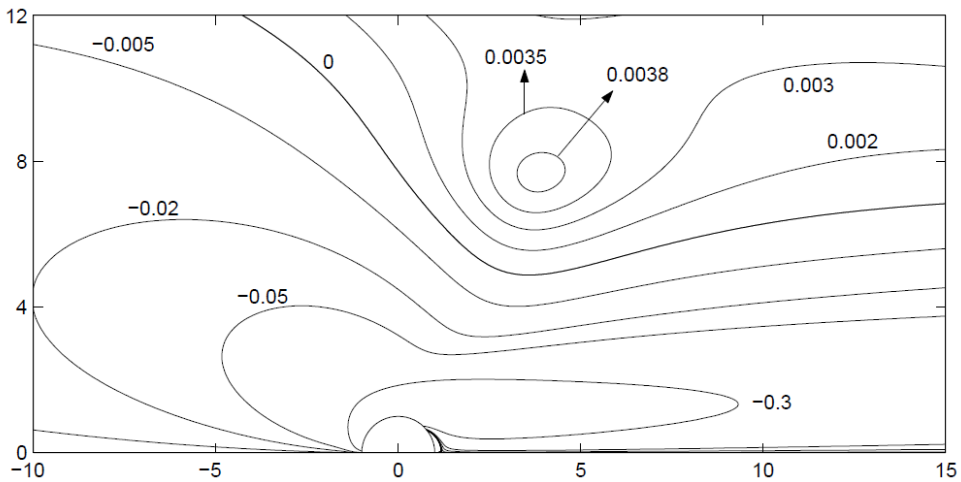


Figure 13. Vorticity lines for $Re = 40$, $M = 7$

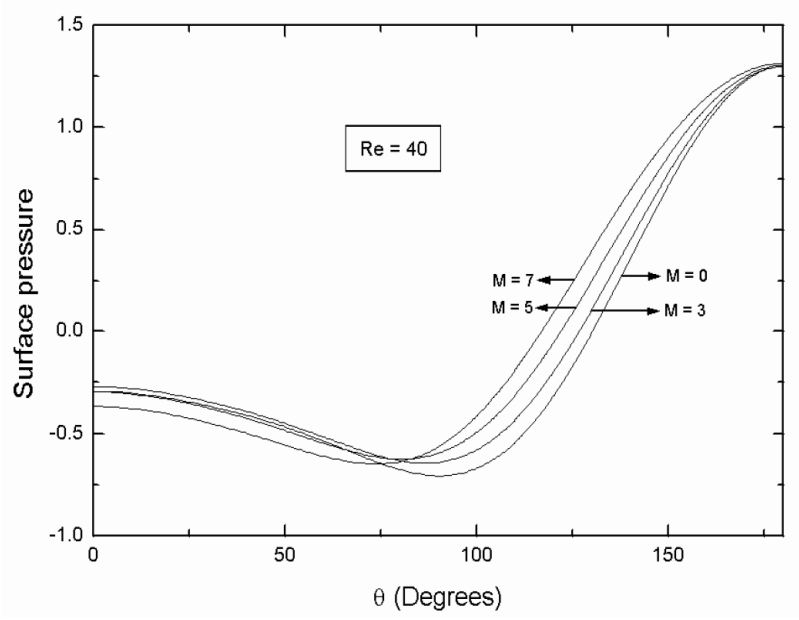


Figure 14. Surface pressure for $Re = 40$ at different M values

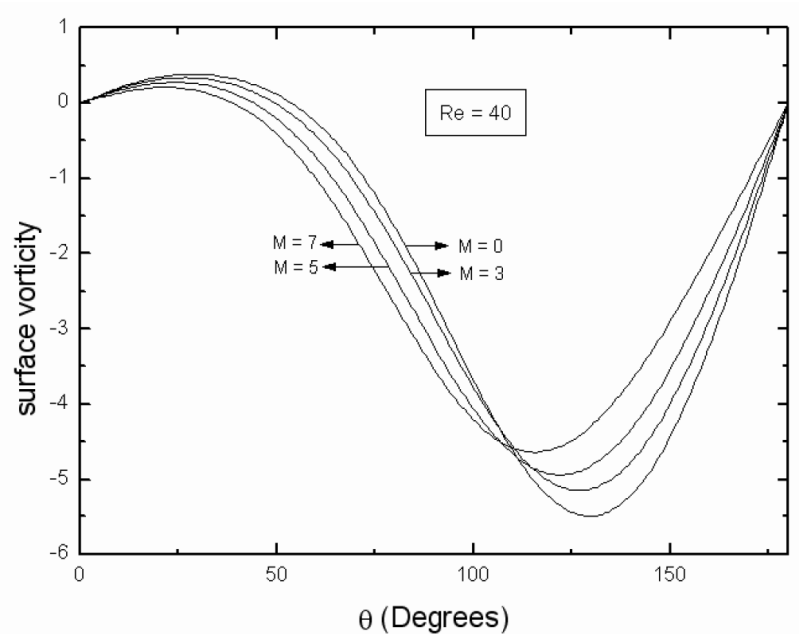


Figure 15. Surface vorticity for $Re = 40$ at different M values

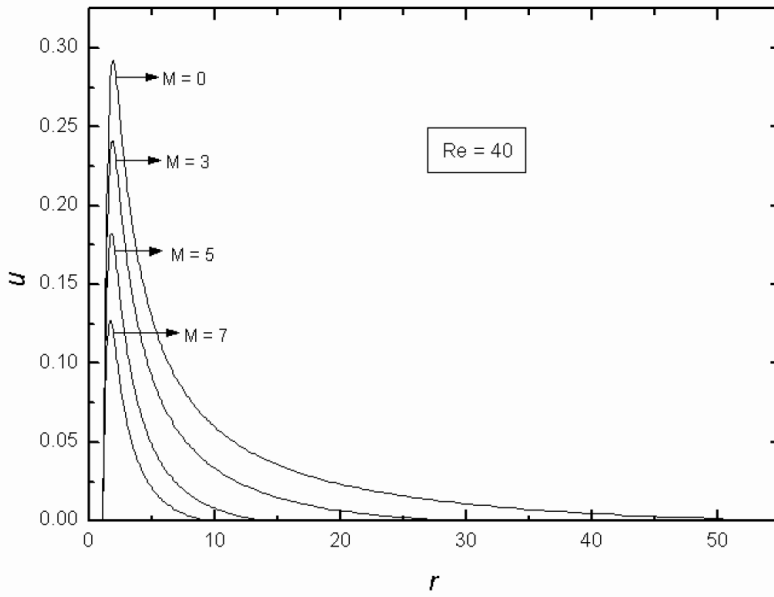


Figure 16. Radial component of velocity within boundary layer at $\theta = 90^\circ$

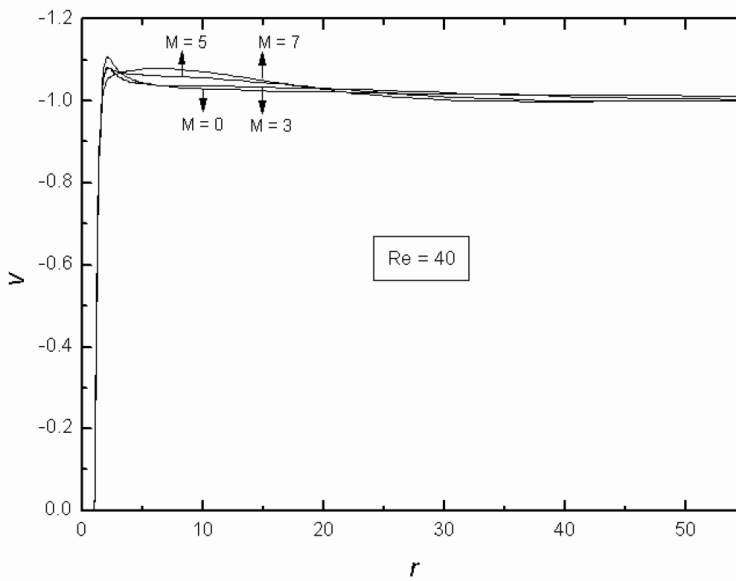


Figure 17. Transverse component of velocity within boundary layer at $\theta = 90^\circ$

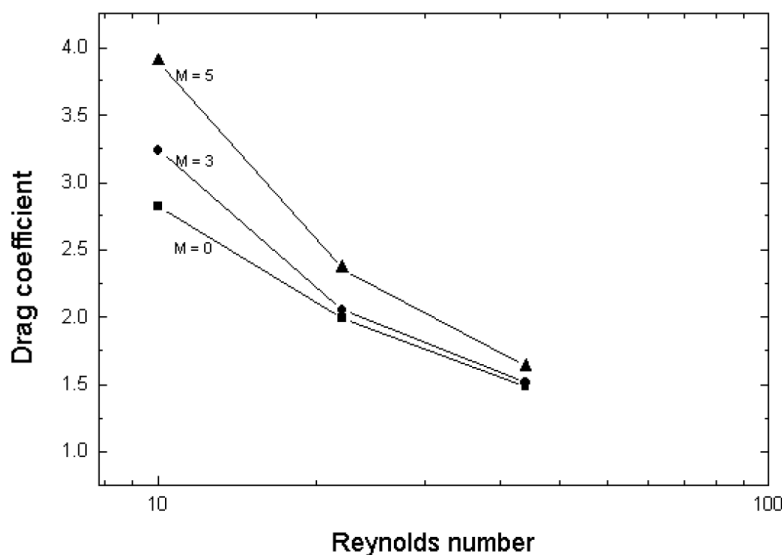


Figure 18. Drag coefficient versus Reynolds number at different M values

REFERENCES

1. BAE, H. M., BARANYI, L., KOIDE, M., TAKAHASHI, T. and SHIRAKASHI, M.: *Suppression of Kármán vortex excitation of a circular cylinder by a second cylinder set downstream in cruciform arrangement*, Journal of Computational and Applied Mechanics, **2**, (2001), 175-188.
2. BARANYI, L. and SHIRAKASHI, M.: *Numerical solution for laminar unsteady flow about fixed and oscillating cylinders*, Computer Assisted Mechanics and Engineering Sciences, **6**, (1999), 263-277.
3. BARANYI, L.: *Computation of unsteady momentum and heat transfer from a fixed cylinder in laminar flow*, Journal of Computational and Applied Mechanics, **4**, (2003), 13-25.
4. BEARMAN, P. W.: *Developments in the understanding of blunt body flows*, JSME Centennial Grand Congress, International Conference on Fluid Engineering, **1**, Tokyo, (1997), 53-61.
5. BRAMELY, J. S.: *Magnetohydrodynamic flow past a circular cylinder*, Journal of Applied Mathematics and Physics, **25**, (1974), 409-416.
6. BRAMELY, J. S.: *Magnetohydrodynamic flow past a circular cylinder-II*, Journal of Applied Mathematics and Physics, **26**, (1975), 203-209.
7. BRAZA, M., CHASSAING, P. and MINH, H. H. : *Numerical study and physical analysis of the pressure and velocity fields in the near wake of a circular cylinder*, Journal of Fluid Mechanics, **165**, (1986), 79-130.
8. DENNIS, S. C. R. and CHANG, G. Z.: *Numerical solutions for steady flow past a circular cylinder at Reynolds numbers up to 100*, Journal of Fluid Mechanics, **42**, (1970), 471-489.
9. FORNBERG, B.: *A numerical study of steady viscous flow past a circular cylinder*, Journal of Fluid Mechanics, **98**, (1980), 819-855.

10. FORNBERG, B.: *Steady viscous flow past a circular cylinder upto Reynolds numbers 600*, Journal of Computational Physics, **61**, (1985), 297-320.
11. INGHAM, D. B. and TANG, T.: *A numerical investigation into the steady flow past a rotating circular cylinder at low and moderate Reynolds numbers*, Journal of Computational Physics, **87**, (1990), 107-124.
12. JUNCU, G. H. and MIHAIL, R.: *Numerical solution of the steady incompressible Navier-Stokes equations for the flow past a sphere by a multigrid defect correction technique*, International Journal of Numerical Methods in Fluids, **11**, (1990), 379-395.
13. JUNCU, G. H.: *A numerical study of steady viscous flow past a fluid sphere*, International Journal of Heat and Fluid Flow, **20**, (1999), 414-421.
14. KARNIADAKIS, G. E. and TRIANTAFYLLOU, D. S.: *Frequency selection and asymptotic states in laminar wakes*, Journal of Fluid Mechanics, **199**, (1989), 441-469.
15. KAWAMURA, T. and KUWAHARA, K. : *Computation of high Reynolds number flow around a circular cylinder with surface roughness*, Proceedings of the 22nd Aerospace Sciences Meeting, Reno, Nevada, AIAA-84-0340, (1984), 1-11.
16. NORBERG, C.: *Flow around a circular cylinder: aspects of fluctuating lift*, Journal of Fluids and Structures, **15**, (2001), 459-469.
17. NORBERG, C.: *Fluctuating lift on a circular cylinder: review and new measurements*, Journal of Fluids and Structures, **17**, (2003), 57-96.
18. RAGHAVA RAO, C. V. and SEKHAR, T. V. S.: *Numerical solution of the slow translation of a sphere moving along the axis of a rotating viscous fluid*, Computational Fluid Dynamics **1**, (1993), 351.
19. RAGHAVA RAO, C. V. and SEKHAR, T. V. S.: *Translation of a sphere in a rotating viscous fluid - A numerical study*, International Journal of Numerical Methods in Fluids, **20**, (1995), 1253.
20. ROSHKO, A.: *On the development of turbulent wakes from vortex sheets*, NACA Rep., 1191, 1954.
21. SEKHAR, T. V. S., RAVIKUMAR, T. V. R. and HARISH KUMAR: *MHD flow past a sphere at low and moderate Reynolds numbers*, Computational Mechanics **31**, (2003) 437-444.
22. SHANTI SWARUP and SINHA, P. C.: *Magnetohydrodynamic flow past a circular cylinder*, Journal of Applied Mathematics and Physics, **28**, (1977), 73-83.
23. WESSELING, P.: *Multigrid Methods in Fluid Dynamics*, In Eds. W Hackbusch and U Trottenberg. Multigrid Methods-III, T337, (1991).
24. WESSELING, P.: *Report NA-37*, Delft University of Technology, The Netherlands (1980).
25. WILLIAMSON, C. H. K.: *Vortex dynamics in the cylinder wake*, Annual Review of Fluid Mechanics, **28**, (1996), 477-539.

ON COUPLED VIBRATIONS OF BEAMS WITH LATERAL LOADS

GÁBOR VÖRÖS

Department of Applied Mechanics, Budapest University of Technology and Economics
H-1512 Budapest, Hungary
voros@mm.bme.hu

[Received: June 19, 2008]

Abstract. The objective of this paper is to analyze the free vibration and mode shapes of straight beams where the coupling between the bending and torsion is induced by steady state lateral loads. The governing differential equations and boundary conditions for the coupled vibrations of Euler-Bernoulli-Vlasov beams are derived by using the virtual work principle which includes the second order terms of finite beam rotations. Closed form solution is found for the coupled frequencies and mode shapes of a symmetric beam with simply supported ends under uniform bending. A finite element model with seven degrees of freedoms per node is also presented. To illustrate the accuracy of this formulation, numerical solutions are presented and compared with available solutions.

Mathematical Subject Classification: 74K10, 70J25, 74S05

Keywords: coupled free vibrations, buckling, torsional warping

1. INTRODUCTION

The determination of natural frequencies and modes is a significant problem in the dynamic analysis of thin-walled beams and it is of great importance in designing of beam structures subject to dynamic loadings. For a beam having cross sectional symmetry in two perpendicular directions the solution of independent bending and torsional free vibration frequencies and mode shapes is well known (Bishop and Johnson, [1]). If the shear center \mathbf{S} and the centroid \mathbf{C} are not coincident, coupling between bending and torsion should be considered during free vibration.

A number of studies dealing with coupled vibrations of thin-walled beams were developed and only a few is mentioned here. Dokumaci [2] derived the exact analytical expression for the solution of the bending-torsion equations and his results were later extended by Bishop et. al. [3] to include torsional warping which is important for thin-walled section beams. Afterwards, Tanaka and Bercin [4] and then Arpacı and Bozdağ [5] extended the approach to triply coupled vibrations of thin-walled beams and Prokić [6] analysed the fivefold coupled vibrations of Timoshenko beams. Banerjee and Williams took into account the effect of axial load [7]. In Ref. [8] Kollár presented the analysis of the natural frequency of composite beams. A dynamic transfer matrix method has been presented by Li et al. [9]. Recently Chen and Hsiao [10] investigated the coupled vibration induced by the boundary conditions.

In the most general case the coupling between different vibration modes is induced not only by the eccentricity of geometry but by the steady state lateral loads and internal stress resultants. The investigation presented in this paper is motivated by the fact that for dynamic structural analyses that are sensitive to the modal vibration properties small errors in the natural frequencies and mode shapes may produce sizable errors in the modal time history and associated structural response (e.g., earthquake response). A literature survey on the subject has revealed that studies of this kind of couplings are limited.

The important points presented in this study are summarized as follows:

The potential energy of nonsymmetric beams subjected to initial loads and stress resultants based on semitangential rotations and moments is firstly derived.

Next, the finite element model is defined by introducing seven nodal parameters.

Equations of motion and the closed form solution are derived from the potential energy principle for simply supported beam under uniform bending load.

Finally, numerical solution is presented for a cantilever under eccentric steady state tip load.

Accordingly the main objective of the present paper is to develop an accurate numerical procedure to account for static loads in linear dynamic analysis of spatial beam structures with arbitrary cross-sections.

2. FORMULATION

2.1. Equations of the problem. In this work, the basic assumptions are as follows: the beam member is straight and prismatic, the cross-section is rigid in its plane but is subjected to torsional warping, rotations are large but strains are small, the material is homogeneous, isotropic and linearly elastic. Figure 1 shows a straight, prismatic beam member with an arbitrary cross-section.

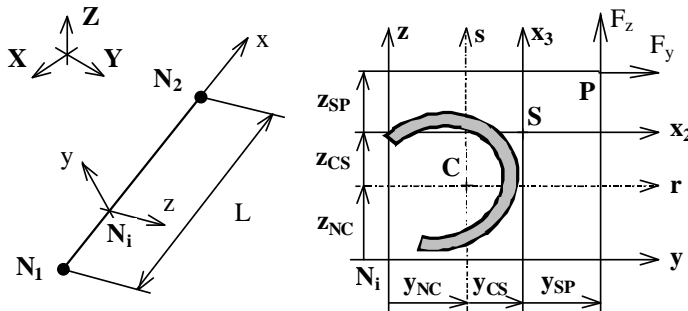


Figure 1. A beam element with local coordinate systems and eccentricities

The local axis x of the right-handed orthogonal system is parallel to the axis of the beam and passes through the end nodes N_1 and N_2 . The co-ordinate axes y and

z are parallel to the principal axes, marked as r and s , respectively. The positions of the centroid \mathbf{C} and shear center \mathbf{S} in the plane of the cross section are given by the co-ordinates y_{NC} , z_{NC} and y_{CS} , z_{CS} . The external loads are applied along points \mathbf{P} located y_{SP} and z_{SP} from the shear center \mathbf{S} .

Based on large rotation theory, the displacement vector consisting of two parts due to the translational and rotational deformations is obtained as (Kim et al. [11], [12]):

$$\mathbf{u} = \mathbf{U} + \mathbf{U}^* \tag{1}$$

where \mathbf{U} and \mathbf{U}^* are the displacements corresponding to the linear and second order terms of displacement parameters due to large rotation effects. In the explicit form these components can be written as:

$$\mathbf{U} = \begin{bmatrix} U_x \\ U_y \\ U_z \end{bmatrix} = \begin{bmatrix} u + \vartheta\varphi \\ v \\ w \end{bmatrix} + \begin{bmatrix} \beta(s - z_{CS}) - \gamma(r - y_{CS}) \\ -\alpha(s - z_{CS}) \\ \alpha(r - y_{CS}) \end{bmatrix}, \tag{2}$$

$$\mathbf{U}^* = \begin{bmatrix} U_x^* \\ U_y^* \\ U_z^* \end{bmatrix} = \frac{1}{2} \begin{bmatrix} \alpha\beta(r - y_{CS}) + \alpha\gamma(s - z_{CS}) \\ -(\alpha^2 + \gamma^2)(r - y_{CS}) + \beta\gamma(s - z_{CS}) \\ \beta\gamma(r - y_{CS}) - (\alpha^2 + \beta^2)(s - z_{CS}) \end{bmatrix}. \tag{3}$$

Displacement parameters are defined at the shear center \mathbf{S} as shown in Figure 2. Accordingly, u , v , and w are the rigid body translations in the directions x , y , and z and α , β and γ denote rigid body rotations about the shear center axes parallel to x , y and z , respectively. The small out-of-plane torsional warping displacement is defined by the $\vartheta(x)$ warping parameter and the warping function $\varphi(r, s)$ is normalized with respect to the shear center. In the following the warping function φ and the shear center location are the same as in the case of free torsion. For thin-walled sections $\varphi = -\omega$, the sector area coordinate introduced in Vlasov’s model. When the shear deformation effects are not considered, the Euler-Bernoulli and the Vlasov internal kinematical constraints are adopted as:

$$\beta = -w', \quad \gamma = v', \quad \vartheta = \alpha' \tag{4}$$

in which the prime denotes differentiation with respect to variable x .

The stress resultants shown in Figure 2 are defined as follows:

$$\begin{aligned} N &= \int_A \sigma_x dA, \quad V_r = \int_A \tau_{xr} dA, \quad V_s = \int_A \tau_{xs} dA, \\ M_t &= \int_A (r\tau_{xs} - s\tau_{xr}) dA, \quad M_r = \int_A s\sigma_x dA, \quad M_s = - \int_A r\sigma_x dA, \quad B = \int_A \varphi\sigma_x dA, \\ M_1 &= M_t - V_s y_{CS} + V_r z_{CS}, \quad M_2 = M_r - z_{CS} N, \quad M_3 = M_s + y_{CS} N, \\ M_W &= \int_A ((r - y_{CS})^2 + (s - z_{CS})^2) \sigma_x dA = N i_p^2 + M_r \beta_r - M_s \beta_s + B \beta_\omega \end{aligned} \tag{5}$$

where N is the axial force, V_r and V_s are the shear forces acting at the shear center, M_1 , M_2 and M_3 are the total twisting and bending moments with respect to shear

center, respectively, and B is the bimoment. The stress resultant M_W is known as the Wagner effect. Also, the sectional properties are defined as

$$\begin{aligned}
 I_r &= \int_A s^2 dA, \quad I_s = \int_A r^2 dA, \quad I_\omega = \int_A \varphi^2 dA, \\
 I_p &= I_s + I_r + A (y_{CS}^2 + z_{CS}^2), \quad i_p^2 = \frac{I_p s}{A}, \quad J = I_r + I_s - \int_A \left(s \frac{\partial \phi}{\partial r} - r \frac{\partial \phi}{\partial s} \right) dA, \\
 \beta_r &= \frac{1}{I_r} \int_A s(r^2 + s^2) dA - 2z_{CS}, \quad \beta_s = \frac{1}{I_s} \int_A r(r^2 + s^2) dA - 2y_{CS}, \\
 \beta_\omega &= \frac{1}{I_\omega} \int_A \varphi(r^2 + s^2) dA,
 \end{aligned} \tag{6}$$

where A denotes the cross sectional area.

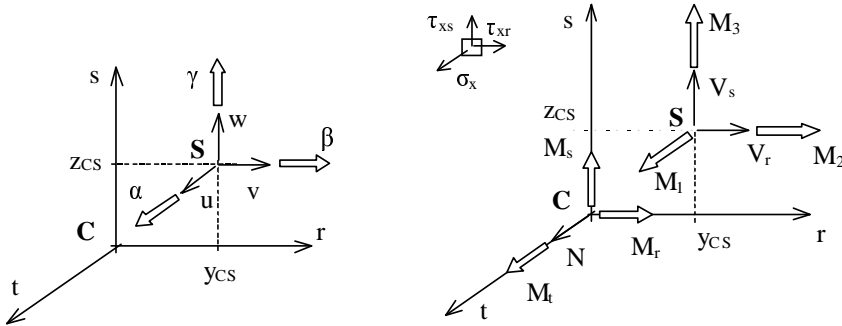


Figure 2. Definition of displacement parameters and stress resultants

The final form of the virtual work principle for the beam structure subjected to initial stresses may be expressed as

$$\delta \Pi = \delta (\Pi_L + \Pi_{Gi} - \Pi_{Ge}) - \delta W = 0 \tag{7}$$

where Π_L , Π_{Gi} , Π_{Ge} are the linear elastic strain energy, the energy change due to initial stress resultants and the potential energy due to eccentric initial external loads, respectively, and W is the work of external load increments on incremental displacements.

The first two terms of total potential (6) can be written as:

$$\Pi_L = \frac{1}{2} \int_0^L [EA(\bar{u}')^2 + EI_r(w'')^2 + EI_s(v'')^2 + EI_\omega(\alpha'')^2 + GJ(\alpha')^2] dx, \tag{8}$$

where E and G are the Young's and shear moduli, respectively, and

$$\begin{aligned}
 \Pi_{Gi} &= \frac{1}{2} \int_0^L [N((v')^2 + (w')^2) + M_W(\alpha')^2 + \\
 &\quad + M_1(v''w' - v'w'') + M_2(v''\alpha - v'\alpha') + M_3(w''\alpha - w'\alpha') + \\
 &\quad + (V_r w' - V_s v')\alpha - 2(V_r v' + V_s w')(w' - v''y_{CS} - w''z_{CS})] dx. \tag{9}
 \end{aligned}$$

The new displacement parameter, i.e. the overall average \bar{u} of the axial displacement U_x is defined as

$$\bar{u} = \frac{1}{A} \int_A U_x dA = u + y_{CS}v' + z_{CS}w'. \tag{10}$$

It should be mentioned that energy functional (7) was consistently obtained corresponding to semitangential internal moments because equation (9) due to initial bending and torsion moments was derived on the basis of including the second order terms of semitangential rotations in equation (3). For a detailed derivation of Π_L and Π_{G_i} the reader is referred to - among others - Kim et al. [12], [13] and Vörös [14].

The third term of equation (7) is the incremental work of initial loads. Considering conservative initial external forces F_x , F_y and F_z each acting at the material point $\mathbf{P}(y_{SP}, z_{SP})$ of the i -th nodal section - see Figure 1 for the details - the incremental work of these forces is

$$\begin{aligned} \Pi_{Ge} &= [F_x U_x^* + F_y U_y^* + F_z U_z^*]_{P_i} = \\ &= \frac{1}{2} [F_x (y_{SP}\beta + z_{SP}\gamma)\alpha + F_y (z_{SP}\beta\gamma - y_{SP}(\gamma^2 + \alpha^2)) + \\ &\quad + F_z (y_{SP}\beta\gamma - z_{SP}(\beta^2 + \alpha^2))]_i \end{aligned} \tag{11}$$

For time dependent dynamic problems, according to the d'Alembert's principle the volume load increment \mathbf{q} is the inertia force and the appropriate virtual work, neglecting the second order terms, can be written in the following form

$$\delta W = \int_V \mathbf{q} \delta \mathbf{u} dV = - \int_V \rho (\ddot{\mathbf{U}} + \ddot{\mathbf{U}}^*) \delta (\mathbf{U} + \mathbf{U}^*) dV \approx - \int_V \rho \ddot{\mathbf{U}} \delta \mathbf{U} dV = \delta \Pi_M$$

where ρ is the mass density per unit volume and dot denotes differentiation with respect to time variable t . Substituting the linear displacements from equation (2) and taking the definitions for the section properties from equation (6) into account the following expression is obtained:

$$\begin{aligned} \delta \Pi_M &= - \int_0^L \rho [A \ddot{u} \delta \bar{u} + A (\ddot{v} + \ddot{\alpha} z_{CS}) \delta v + A (\ddot{w} - \ddot{\alpha} y_{CS}) \delta w + \\ &\quad + A (\ddot{v} z_{CS} - \ddot{w} y_{CS} + \ddot{\alpha} i_p^2) \delta \alpha + I_s \ddot{v}' \delta v' + I_r \ddot{w}' \delta w' + I_\omega \ddot{\alpha}' \delta \alpha'] dx. \end{aligned} \tag{12}$$

2.2. Finite element discretisation. The derivation of finite element matrices is based on the assumed displacement field. The nodal vector of seven local displacement parameters is defined as

$$\Delta_i = [\bar{u} \quad v \quad w \quad \alpha \quad \beta \quad \gamma \quad \vartheta]_i^T, \quad \mathbf{U}_E = \begin{bmatrix} \Delta_1 \\ \Delta_2 \end{bmatrix}. \tag{13}$$

A linear interpolation is adopted for the axial displacement and a cubic Hermitian function for the lateral deflections and twist:

$$\begin{aligned}
 \bar{u}(\xi) &= \bar{u}_1(1 - \xi) + \bar{u}_2\xi, \\
 v(\xi) &= v_1F_1 + \gamma_1LF_2 + v_2F_3 + \gamma_2LF_4, \\
 w(\xi) &= w_1F_1 - \beta_1LF_2 + w_2F_3 - \beta_2LF_4, \\
 \alpha(\xi) &= \alpha_1F_1 + \vartheta_1F_2 + \alpha_2N_3 + \vartheta_2LN_4
 \end{aligned} \tag{14}$$

where

$$F_1 = 1 - 3\xi^2 + 2\xi^3, \quad F_2 = \xi - 2\xi^2 + \xi^3, \quad F_3 = 3\xi^2 - 2\xi^3, \quad F_4 = \xi^3 - \xi^2, \quad \xi = \frac{x}{L}.$$

Substituting the shape functions into equations (8), (9), (11) and (12) and integrating along the element length L , the elementary matrices obtained can be defined as:

$$\begin{aligned}
 \delta\mathbf{\Pi}_L &= \delta\mathbf{U}_E^T \mathbf{k}_L \mathbf{U}_E, & \delta\mathbf{\Pi}_{G_i} &= \delta\mathbf{U}_E^T \mathbf{k}_{G_i} \mathbf{U}_E, \\
 \delta\mathbf{\Pi}_{G_e} &= \delta\mathbf{U}_E^T \mathbf{k}_{G_e} \mathbf{U}_E, & \delta\mathbf{\Pi}_M &= \delta\mathbf{U}_E^T \mathbf{m} \mathbf{U}_E.
 \end{aligned} \tag{15}$$

The \mathbf{k}_L linear stiffness is the same as that published by Attard [15] and the exactly integrated 14x14 element geometric stiffness and consistent mass matrices \mathbf{k}_{G_i} , \mathbf{k}_{G_e} and \mathbf{m} were presented by Vörös [14], [16]. In this study it is assumed that the M_r and M_s initial bending moments are linearly varying along a beam element length, while the other internal force components are uniform. In this case the uniform shear forces can be approximated as $V_s = (M_{r2} - M_{r1})/L$ and $V_r = -(M_{s2} - M_{s1})/L$, where 1 and 2 in the indices refer to the \mathbf{M}_1 and \mathbf{M}_2 nodal moments.

This procedure was implemented in a conventional finite element program called VEM7 to obtain numerical results given in the following sections.

3. FREE VIBRATION OF A SIMPLY SUPPORTED BEAM

To study the effect of the initial bending on dynamic behaviour, consider a straight beam under a uniform bending moment. Both end loads are quasitangential moments and each moment is equivalent to a couple with a small rigid lever as shown in Figure 3. A quasitangential bending moment can be regarded as the simultaneous action of two eccentric axial forces. Therefore, making use of equation (11) at first with $F_x = F$, $z_{SP} = a/2$ than $F_x = -F$, $z_{SP} = -a/2$ at the $x = L$ end and the same but with opposite forces at the $x = 0$ end of the beam, the virtual work of quasitangential moment under small spatial rotations can be evaluated as follows:

$$\Pi_{G_e} = -\frac{1}{2} [F a \gamma \alpha]_{x=L} - \frac{1}{2} [-F a \gamma \alpha]_{x=0} = -\frac{1}{2} M [\gamma \alpha]_0^L, \tag{16}$$

where $M = Fa$.

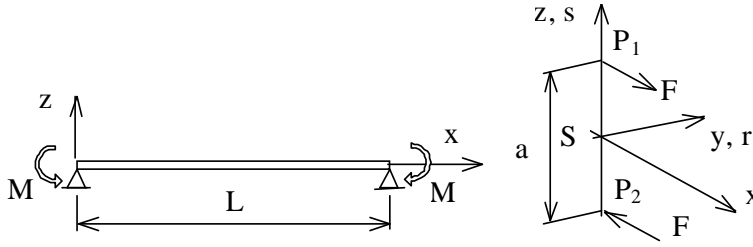


Figure 3. Simply supported beam with quasitangential end moments

To derive a closed form solution for the simplest case, a doubly symmetric section is taken and the only non zero initial stress resultant is the uniform bending moment. Now applying the $\beta_r = 0$ and $M_2 = M_r = M$ conditions in equation (9) and adopting the internal constraints (5) in equation (16), the actual form of the virtual work principle (7) is obtained as:

$$\begin{aligned} \delta \Pi = & \delta \int_0^L \frac{1}{2} (EA(\bar{u}')^2 + EI_r w'' + EI_s (v'')^2 + EI_\omega (\alpha'')^2 + GJ(\alpha')^2) dx + \\ & + \int_0^L \rho [A(\ddot{u}\delta\bar{u} + \ddot{v}\delta v + \ddot{w}\delta w) + I_p \ddot{\alpha}\delta\alpha + I_s \ddot{v}'\delta v' + I_r \ddot{w}'\delta w' + I_\omega \ddot{\alpha}'\delta\alpha'] dx + \\ & + \delta \int_0^L \frac{1}{2} M (v''\alpha - v'\alpha') dx + -\frac{1}{2} M \delta [v'\alpha]_0^L = 0. \end{aligned} \quad (17)$$

It can be seen that due to the initial bending moment $M_r = M$ the lateral displacement $v(x, t)$ and the torsional rotation $\alpha(x, t)$ are coupled. Neglecting the third mixed derivative terms (effects of rotary and warping inertia) in the above principle and focusing on the coupled parameters only from the variation of equation (17) with respect to v and α the equations of motion and boundary conditions are derived as follows:

$$\begin{aligned} EI_s v'''' + M\alpha'' + \rho A \ddot{v} &= 0 \\ EI_\omega \alpha'''' - GJ\alpha'' + Mv'' + \rho I_p \ddot{\alpha} &= 0. \end{aligned} \quad (18a)$$

$$\begin{aligned} [(EI_s v'''' - M\alpha'') \delta v]_0^L = 0, \quad [(EI_s v'') \delta v']_0^L = 0, \\ [(-EI_\omega \alpha'''' + GJ\alpha' - Mv'') \delta \alpha]_0^L = 0, \quad [(EI_\omega \alpha'') \delta \alpha']_0^L = 0. \end{aligned} \quad (18b)$$

In the case of simply supports at each end (fork like supports which prevent torsional rotation and allow free warping) the boundary conditions are:

$$x = 0, \quad x = L : \quad v = 0, \quad \alpha = 0, \quad v'' = 0, \quad \alpha'' = 0. \quad (18c)$$

For free harmonic vibrations the boundary conditions are satisfied by taking the trial solutions as

$$v(x, t) = v_0 \sin\left(\frac{i\pi}{L}x\right) \sin \omega t, \quad \alpha(x, t) = \alpha_0 \sin\left(\frac{i\pi}{L}x\right) \sin \omega t, \quad (19)$$

where v_0, α_0 are the modal amplitudes and ω is the circular frequency. Substituting equation (19) into equation (18a) results in the following linear homogeneous equations:

$$\begin{bmatrix} \left(EI_s \left(i \frac{\pi}{L} \right)^4 - \rho A \omega^2 \right) & -M \left(i \frac{\pi}{L} \right)^2 \\ -M \left(i \frac{\pi}{L} \right)^2 & \left(EI_\omega \left(i \frac{\pi}{L} \right)^4 + GJ \left(i \frac{\pi}{L} \right)^2 - \rho I_p \omega^2 \right) \end{bmatrix} \begin{bmatrix} v_0 \\ \alpha_0 \end{bmatrix} = \begin{bmatrix} 0 \\ 0 \end{bmatrix}. \quad (20)$$

Obviously, if there is no moment load on the beam, that is $M = 0$, then the uncoupled lateral bending and torsional frequencies are

$$\omega_{bi}^2 = \left(i \frac{\pi}{L} \right)^4 \frac{EI_s}{\rho A}, \quad \omega_{ti}^2 = \left(i \frac{\pi}{L} \right)^2 \frac{GJ}{\rho I_p} \left[1 + \left(i \frac{\pi}{L} \right)^2 \frac{EI_\omega}{GJ} \right], \quad i = 1, 2, \dots \quad (21)$$

Taking the solution of equation (20) in the static case for which $\omega = 0$ the following moment eigenvalues are obtained

$$M_i^2 = \left(i \frac{\pi}{L} \right)^2 EG I_s J \left(1 + \left(i \frac{\pi}{L} \right)^2 \frac{EI_\omega}{GJ} \right), \quad i = 1, 2, \dots \quad (22)$$

and the smallest moment obtained for $i = 1$ is the critical bending load:

$$M_{cr} = M_1 = \pm \frac{\pi}{L} \sqrt{EG I_s J} \sqrt{1 + \frac{\pi^2 EI_\omega}{L^2 GJ}} = \pm \frac{L^2}{\pi^2} \rho \sqrt{AI_p} \omega_{b1} \omega_{t1}. \quad (23)$$

Introducing the steady state moment load factor as

$$\mu_i = M/M_i \quad (24)$$

and substituting equations (21) and (22) into equation (20) yields

$$\begin{bmatrix} A(\omega_{bi}^2 - \omega^2) & -\sqrt{AI_p} \mu_i \omega_{bi} \omega_{ti} \\ -\sqrt{AI_p} \mu_i \omega_{bi} \omega_{ti} & I_p (\omega_{ti}^2 - \omega^2) \end{bmatrix} \begin{bmatrix} v_0 \\ \alpha_0 \end{bmatrix} = \begin{bmatrix} 0 \\ 0 \end{bmatrix}. \quad (25)$$

The non-trivial solution is obtained by setting the determinant of the above system equal to zero. For every i two natural frequencies can be calculated:

$$\omega_{i,1,2}^2 = \frac{\omega_{ti}^2 + \omega_{bi}^2}{2} \pm \sqrt{\left(\frac{\omega_{ti}^2 - \omega_{bi}^2}{2} \right)^2 + \mu_i^2 \omega_{ti}^2 \omega_{bi}^2}. \quad (26)$$

It can be seen from this result, that only the bending and torsion modes with the same i index are coupled. Now if $i = 1$ and $\omega_{b1} < \omega_{t1}$ then the first two coupled frequencies are

$$\omega_{1,1}^2 = \frac{\omega_{t1}^2 + \omega_{b1}^2}{2} - \sqrt{\left(\frac{\omega_{t1}^2 - \omega_{b1}^2}{2} \right)^2 + \mu_1^2 \omega_{t1}^2 \omega_{b1}^2}, \quad (27)$$

$$\omega_{1,2}^2 = \frac{\omega_{t1}^2 + \omega_{b1}^2}{2} + \sqrt{\left(\frac{\omega_{t1}^2 - \omega_{b1}^2}{2} \right)^2 + \mu_1^2 \omega_{t1}^2 \omega_{b1}^2}. \quad (28)$$

The corresponding diagrams of the bending moment and frequencies are shown in Figure 4. From equations (27,b) the extreme values of the plots are:

$$\begin{aligned}
 M = 0, \quad \mu_1 = 0, \quad \omega_{1,1}^2 = \omega_{b1}^2, \quad \omega_{1,2}^2 = \omega_{t1}^2, \\
 M = \pm M_{cr}, \quad \mu_1 = \pm 1, \quad \omega_{1,1}^2 = 0, \quad \omega_{1,2}^2 = \omega_{t1}^2 + \omega_{b1}^2.
 \end{aligned}
 \tag{29}$$

Once the natural frequencies are found, the modal amplitudes can be calculated in the usual way. The ratio of first modal amplitudes, or the modal bending-torsion mixing factor, from the first row of equation (25) is:

$$\frac{\alpha_0 i_p}{v_0} = \frac{\omega_{b1}^2 - \omega_{1,1}^2}{\mu_1 \omega_{b1} \omega_{t1}}.
 \tag{30}$$

The mixing factor-moment plot can also be seen in Figure 4. In a limit case, when $M = M_{cr}$ and $\mu_1 = 1$, the value of mode mixing factor is

$$\frac{\alpha_0 i_p}{v_0} = \frac{\omega_{b1}}{\omega_{t1}}.
 \tag{31}$$

Briefly, the bending-torsion mixing factor of the lateral bending-torsion buckling mode shape is proportional to the ratio of uncoupled natural frequencies.

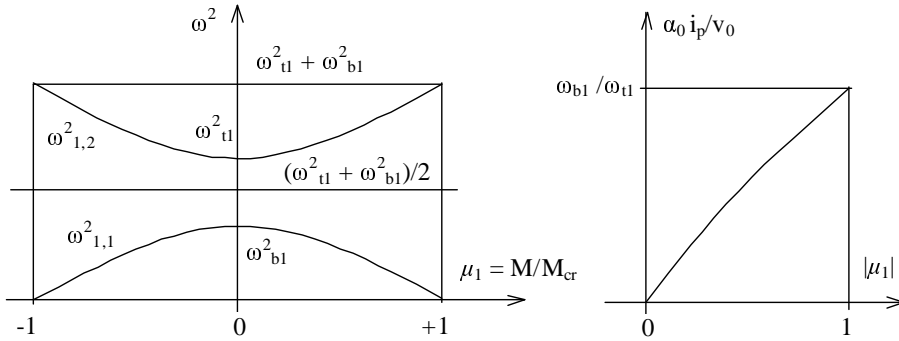


Figure 4. Change of first pair of coupled frequencies and mixing factor of the first mode

M (106 Nmm)	μ_1	FEM7			Eq.(27a)	Eq.(27b)	Eq.(29)
		$\omega_{1,1}$	$\omega_{1,2}$	$\alpha_0 i_p / v_0$	$\omega_{1,1}$	$\omega_{1,2}$	$\alpha_0 i_p / v_0$
0	0	68.93	161.4	0	69.00	161.4	0
10	0.284	65.51	162.8	0.145	65.58	162.8	0.146
20	0.569	54.91	166.7	0.274	54.93	166.7	0.275
35	0.995	6.39	175.4	0.425	6.34	175.4	0.426

Table 1. Comparison of coupled frequencies (1/sec) and mode mixing factors

To examine the validity and accuracy of the proposed VEM7 model, numerical and the closed form solutions are compared. Material and cross sectional properties used in this example are listed in Figure 5, and the length of the simply supported beam is $L = 4$ m. The first uncoupled lateral bending and torsional frequencies, using

equation (21) are $\omega_{b1} = 69.00 \text{ sec}^{-1}$, $\omega_{t1} = 161.4 \text{ sec}^{-1}$ and the buckling moment from equation (23) $M_1 = M_{cr} = \pm 35.18 \times 10^6 \text{ Nmm}$. Table 1 shows that the FEM7 solutions using 10 elements are practically identical with the closed form solutions.

4. CANTILEVER WITH LATERAL LOAD

In the following a straight cantilever beam of length L with a monosymmetric and uniform cross section is considered. The beam is shown in Figure 5. The distance between the centroid and shear center is denoted by z_{CS} and the initial lateral load F is applied at the cantilever right end with an eccentricity z_{SP} .

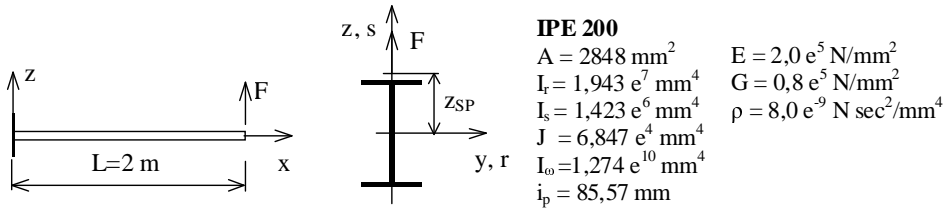


Figure 5. Cantilever beam with a tip load

Because the lateral bending in y direction and the torsional vibrations are coupled, only the $v(x, t)$ and $\alpha(x, t)$ increments are considered here. Applying the non zero initial stress resultants $M_2 = M_r$ and V_s in equation (9) the final form of the virtual work principle (7) is obtained as:

$$\begin{aligned} \delta \Pi = & \delta \int_0^L \frac{1}{2} (EI_s (v'')^2 + EI_\omega (\alpha'')^2 + GJ (\alpha')^2) dx + \\ & + \delta \int_0^L \frac{1}{2} [M_r (\beta_r \alpha^2 + v'' \alpha - v' \alpha') - V_s v' \alpha] dx + \\ & + \int_0^L \rho [A (\ddot{v} + z_{CS} \ddot{\alpha}) \delta v + (I_p \ddot{\alpha} + A z_{CS} \ddot{v}) \delta \alpha + I_s \dot{v}' \delta v' + I_\omega \dot{\alpha}' \delta \alpha'] dx + \\ & + \frac{1}{2} \delta [F z_{SP} \alpha^2]_{x=L} = 0. \quad (32) \end{aligned}$$

Now, in due course, at first integrating by part the variation of equation (32) then replacing the internal equilibrium equation $dM_r/dx = V_s$ the equations of motion can be derived in the following form:

$$\begin{aligned} EI_s v'''' + (M_r \alpha)'' + \rho A (\ddot{v} + z_{CS} \ddot{\alpha}) - \rho I_s \ddot{v}'' &= 0, \\ EI_\omega \alpha'''' - GJ \alpha'' - \beta_r (M_r \alpha')' + M_r v'' + \rho I_p \ddot{\alpha} + \rho A z_{CS} \ddot{v} - \rho I_\omega \ddot{\alpha}'' &= 0. \end{aligned} \quad (33a)$$

The corresponding boundary conditions with $M_r(L) = 0$ are

$$\begin{aligned} x = 0: v = 0, \quad \alpha = 0, \quad v' = 0, \quad \alpha' = 0, \\ x = L: v'' = 0, \quad -EI_s v'''' + \rho I_s \ddot{v}' = 0, \\ \alpha'' = 0, \quad -EI_\omega \alpha'''' + GJ \alpha' + \rho I_\omega \ddot{\alpha}' + F z_{SP} \alpha = 0. \end{aligned} \quad (33b)$$

It should be noted, that equation (33a) is coupled for the following two reasons: asymmetry of the section (z_{CS} , β_r) and the internal stress resultant (M_r).

F (10^3 kN)	$\omega_{1.1}$ (1/sec)	$\omega_{1.2}$ (1/sec)	$\alpha_0 i_p / v_0$
0	98.21	150.1	0
± 20	89.39	148.0	0.250
± 30	76.07	145.8	0.373
± 46	7.71	142.0	0.546

Table 2. Frequencies and mode mixing factor, $z_{SP} = 0$ mm, $F_{cr} = \pm 46.13$ kN

F (10^3 kN)	$\omega_{1.1}$ (1/sec)	$\omega_{1.2}$ (1/sec)	$\alpha_0 i_p / v_0$
-22	19.70	107.4	1.311
0	98.21	150.1	0
+30	87.33	197.7	0.141
+65	9.30	204.9	0.215

Table 3. Frequencies and mode mixing factor, $z_{SP} = 100$ mm, $F_{cr} = -22.38$ kN / + 65.26 kN

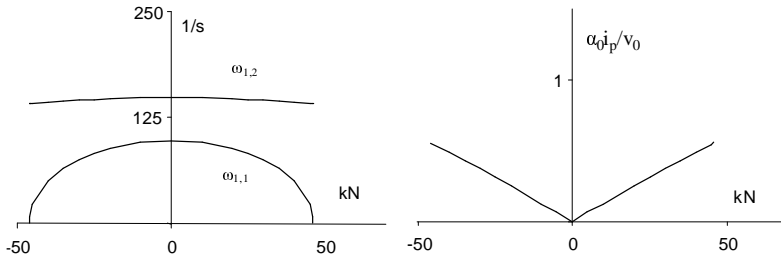


Figure 6. Change of coupled frequencies and mode mixing factor, $z_{SP} = 0$ mm

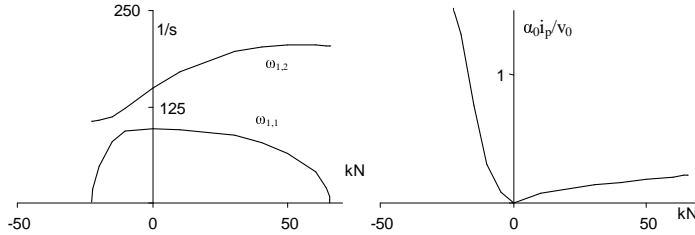


Figure 7. Change of coupled frequencies and mode mixing factor, $z_{SP} = 100$ mm

In general - even if the section is symmetric and the rotary and warping acceleration terms are neglected - it is not possible to derive a closed form solution for the coupled vibration of the cantilever, so numerical solutions by FEM7 model are presented here.

The first two coupled bending-torsion natural frequencies and the mode mixing factor - defined in equation (30) - of the first mode shape are given in Tables 2 and 3 for various eccentricities. As can be seen in Figures 6 and 7 the load eccentricity has a significant influence on the natural frequencies and particularly on the mode shapes even if the section is symmetric. For example, if a vertical tip load of magnitude $F = -10 \text{ kN} \approx F_{cr}/2$ pointing downwards acts on the top flange of IPE200 section ($z_{SP} = 100 \text{ mm}$) the decrease of the first two frequencies approximately are 4% and 20% respectively, and 30% of the lateral displacement of the load point of action comes from the torsional component of the first mode shape.

5. CONCLUSION

The paper presented a numerical method analysing the effect of steady state bending on the coupled bending torsional vibration and mode shapes of Bernoulli-Vlasov beams. It was found that the initial bending moment has a significant effect on the mode shapes. This prove the need of second order dynamics in structural analysis. The FEM7 finite element approach can be advantageously extended to more complex problems of spatial beam structures.

REFERENCES

1. BISHOP, R. E. D. and JOHNSON, D. C.: *The mechanics of vibration*. Cambridge University Press, Cambridge, 1979.
2. DOKUMACI, E.: An exact solution for coupled bending and torsion vibrations of uniform beams having single cross-sectional symmetry. *Journal of Sound and Vibration*, **119**, (1987), 443–449.
3. BISHOP, R. E. D., CANNON, S. M. ., and MIAO, S.: On coupled bending and torsional vibration of uniform beams. *Journal of Sound and Vibration*, **131**, (1989), 457–464.
4. TANAKA, M. and BERCIN, A. N.: Free vibration solution for uniform beams of non-symmetric cross section using mathematica. *Computers and Structures*, **71**(7-8), (1999), 1–8.
5. ARPACI, A. and BOZDAG, E.: On the free vibration analysis of thin-walled beams with nonsymmetric open cross sections. *Computers and Structures*, **80**, (2002), 691–695.
6. PROKIĆ, A.: On fivefold coupled vibrations of timoshenko thin-walled beams. *Engineering Structures*, **28**, (2006), 54–62.
7. BANERJEE, J. R. and W., W. F.: Coupled bending-torsional dynamic stiffness matrix of an axially loaded timoshenko beam element. *International Journal of Solids and Structures*, **31**, (1994), 749–762.
8. KOLLÁR, L.: Flexural-torsional vibration of open section composite beams with shear deformation. *International Journal of Solids and Structures*, **38**, (2001), 7543–7548.

9. LI, J., SHEN, R., HUA, H., and JIN, X.: Coupled bending and torsional vibration of axially loaded thin-walled timoshenko beams. *International Journal of Mechanical Sciences*, **46**, (2004), 299–320.
10. CHEN, H. H. and HSIAO, K. M.: Coupled axial-torsional vibration of thin walled z-section beam induced by boundary conditions. *Thin Walleed Structures*, **45**, (2007), 573–583.
11. KIM, M. Y., CHANG, S. P., and PARK, H. G.: Spatial postbuckling analysis of non-symmetric thin-walled frames. i: Theoretical considerations based on semitangential property. *Journal of Engineering Mechanics (ASCE)*, **127**(8), (2001), 769–778.
12. KIM, M. Y., CHANG, S. P., and KIM, S. B.: Spatial postbuckling analysis of nonsymmetric thin-walled frames. ii: Geometrically nonlinear fe procedures. *Journal of Engineering Mechanics (ASCE)*, **127**(8), (2001), 779–790.
13. KIM, M. Y., YUN, H. T., and KIM, N. I.: Exact dynamic and static element stiffness matrices of nonsymmetric thin-walled beam-columns. *Computers and Structures*, **81**(7-8), (2003), 1425–1448.
14. VÖRÖS, G.: An improved formulation of space stiffeners. *Computers and Structures*, **85**(7-8), (2007), 350–359.
15. ATTARD, M. M.: Lateral buckling analysis of beams by the fem. *Computers and Structures*, **23**(2), (1986), 217–231.
16. VÖRÖS, G.: Free vibration of thin walled beams. *Periodica Polytechnica, Series of Mechanical Engineering*, **48**, (2004), 99–110.

Notes for Contributors

to the Journal of Computational and Applied Mechanics

Aims and scope. The aim of the journal is to publish research papers on theoretical and applied mechanics. Special emphasis is given to articles on computational mechanics, continuum mechanics (mechanics of solid bodies, fluid mechanics, heat and mass transfer) and dynamics. Review papers on a research field and materials effective for teaching can also be accepted and are published as review papers or classroom notes. Papers devoted to mathematical problems relevant to mechanics will also be considered.

Frequency of the journal. Two issues a year (approximately 80 pages per issue).

Submission of Manuscripts. Submission of a manuscript implies that the paper has not been published, nor is being considered for publication elsewhere. Papers should be written in standard grammatical English. The manuscript is to be submitted in electronic, preferably in pdf, format. The text is to be 130 mm wide and 190 mm long and the main text should be typeset in 10pt CMR fonts. Though the length of a paper is not prescribed, authors are encouraged to write concisely. However, short communications or discussions on papers published in the journal must not be longer than 2 pages. Each manuscript should be provided with an English Abstract of about 50–70 words, reporting concisely on the objective and results of the paper. The Abstract is followed by the Mathematical Subject Classification – in case the author (or authors) give the classification codes – then the keywords (no more than five). References should be grouped at the end of the paper in numerical order of appearance. Author's name(s) and initials, paper titles, journal name, volume, issue, year and page numbers should be given for all journals referenced.

The journal prefers the submission of manuscripts in L^AT_EX. Authors should prefer the $\mathcal{A}\mathcal{M}\mathcal{S}$ -L^AT_EX article class and are not recommended to define their own L^AT_EX commands. Visit our home page for further details concerning the issue how to edit your paper.

For the purpose of refereeing the manuscripts should be sent either to Balázs Tóth (Balazs.TOTH@uni-miskolc.hu) or György SZEIDL (Gyorgy.SZEIDL@uni-miskolc.hu).

The eventual supply of an accepted for publication paper in its final camera-ready form will ensure more rapid publication. Format requirements are provided by the home page of the journal from which sample L^AT_EX files can be downloaded:

<http://www.mech.uni-miskolc.hu/jcam>

These sample files can also be obtained directly (via e-mail) from Balázs TÓTH (Balazs.TOTH@uni-miskolc.hu), upon request.

One issue of the journal and ten offprints will be provided free of charge and mailed to the correspondent author. Since JCAM is an open access journal each paper can be downloaded freely from the homepage of the journal.

The Journal of Computational and Applied Mechanics is abstracted in Zentralblatt für Mathematik and in the Russian Referativnij Zhurnal.

Secretariat of the Vice-Rector for Research and International Relations, University of Miskolc
Responsible for publication: Prof. Dr. Tamás Kékesi
Published by the Miskolc University Press under the leadership of Erzsébet Burmeister
Responsible for duplication: Works manager Erzsébet Pásztor
Number of copies printed: 75
Put to the Press on October 1, 2014
Number of permission: TNRT 2014-340-ME

HU ISSN 1586-2070

A Short History of the Publications of the University of Miskolc

The University of Miskolc (Hungary) is an important center of research in Central Europe. Its parent university was founded by the Empress Maria Teresia in Selmecebánya (today Banská Štiavnica, Slovakia) in 1735. After the first World War the legal predecessor of the University of Miskolc moved to Sopron (Hungary) where, in 1929, it started the series of university publications with the title *Publications of the Mining and Metallurgical Division of the Hungarian Academy of Mining and Forestry Engineering* (Volumes I.-VI.). From 1934 to 1947 the Institution had the name Faculty of Mining, Metallurgical and Forestry Engineering of the József Nádor University of Technology and Economic Sciences at Sopron. Accordingly, the publications were given the title *Publications of the Mining and Metallurgical Engineering Division* (Volumes VII.-XVI.). For the last volume before 1950 – due to a further change in the name of the Institution – *Technical University, Faculties of Mining, Metallurgical and Forestry Engineering, Publications of the Mining and Metallurgical Divisions* was the title.

For some years after 1950 the Publications were temporarily suspended.

After the foundation of the Mechanical Engineering Faculty in Miskolc in 1949 and the movement of the Sopron Mining and Metallurgical Faculties to Miskolc, the Publications restarted with the general title *Publications of the Technical University of Heavy Industry* in 1955. Four new series - Series A (Mining), Series B (Metallurgy), Series C (Machinery) and Series D (Natural Sciences) - were founded in 1976. These came out both in foreign languages (English, German and Russian) and in Hungarian.

In 1990, right after the foundation of some new faculties, the university was renamed to University of Miskolc. At the same time the structure of the Publications was reorganized so that it could follow the faculty structure. Accordingly three new series were established: Series E (Legal Sciences), Series F (Economic Sciences) and Series G (Humanities and Social Sciences). The latest series, i.e., the series H (European Integration Studies) was founded in 2001. The eight series are formed by some periodicals and such publications which come out with various frequencies.

Papers on computational and applied mechanics were published in the

Publications of the University of Miskolc, Series D, Natural Sciences.

This series was given the name Natural Sciences, Mathematics in 1995. The name change reflects the fact that most of the papers published in the journal are of mathematical nature though papers on mechanics also come out.

The series

Publications of the University of Miskolc, Series C, Fundamental Engineering Sciences

founded in 1995 also published papers on mechanical issues. The present journal, which is published with the support of the Faculty of Mechanical Engineering and Informatics as a member of the Series C (Machinery), is the legal successor of the above journal.



Contents

Contributed Papers

Atila BAKSA, István PÁCZELT and Tamás SZABÓ: Solution of 3D contact problems using spline interpolation	125–147
István ECSEDI and Kornél DLUHI: Vector formulae for non-homogeneous prismatic bars	149–169
László KISS: In-plane buckling of rotationally restrained heterogeneous shallow arches subjected to a concentrated force at the crown point	171–199
T. V. S. SEKHAR, R. SIVAKUMAR and H. KUMAR: Numerical solutions for steady viscous flow past a circular cylinder in an aligned magnetic field	201–217
Gábor VÖRÖS: On coupled vibrations of beams with lateral loads	219–231